Pilot Experiments with Relativistic Uranium Projectile and Fission Fragments Thermalized in a Cryogenic Gas-filled Stopping Cell

Inauguraldissertation zur Erlangung des Doktorgrades der Naturwissenschaftlichen Fakultät der Justus-Liebig-Universität Gießen

vorgelegt von

Moritz Pascal Reiter
geboren in Giessen

Fachbereich 07 - Mathematik und Informatik, Physik, Geographie

II. Physikalisches Institut Justus-Liebig-Universität Gießen

Gießen 2015

Selbstständigkeitserklärung

Ich erkläre: Ich habe die vorgelegte Dissertation selbständig und ohne unerlaubte fremde Hilfe und nur mit den Hilfen angefertigt, die ich in der Dissertation angegeben habe. Alle Textstellen, die wörtlich oder sinngemäß aus veröffentlichten Schriften entnommen sind, und alle Angaben, die auf mündlichen Auskünften beruhen, sind als solche kenntlich gemacht. Bei den von mir durchgeführten und in der Dissertation erwähnten Untersuchungen habe ich die Grundsätze guter wissenschaftlicher Praxis, wie sie in der „Satzung der Justus-Liebig-Universität Gießen zur Sicherung guter wissenschaftlicher Praxis“ niedergelegt sind, eingehalten.

Datum	Moritz Pascal Reiter

Erstgutachter: Prof. Dr. Christoph Scheidenberger
Zweitgutachter: Prof. Dr. Dr. h.c. Hans Geissel

Contents

1 Introduction

In nature about 300 stable nuclides exist. In addition, some 3000 unstable nuclides have been observed so far, and theoretical predictions expect in total approximately 6000 nuclides to exist. Thus, about 3000 nuclides are hitherto unobserved. While the stable nuclei have rather balanced numbers of protons and neutrons, the unstable nuclei, often called 'exotic nuclei', are characterized by significantly different neutron (N) to proton number (Z) ratios compared to those found in nature. They are created in stellar environments and prevail in stars or star explosions and often have 'exotic' properties. They are radioactive and often have short half-lives. This makes them difficult to study. Their existence is limited by the so-called proton and neutron drip-lines, where the nucleon separation energies become negative and additional nucleons are no longer bound to the nucleus.

Knowledge of the structure of the nucleus and its decay properties has been gained mainly from nuclei, which are stable or are found in the vicinity of the line of beta-stability (the so-called 'valley of stability'). At the moment the physical properties of exotic nuclides, such as masses, half-lives, decay modes etc., can in principle be predicted by theoretical models. However, even present theoretical models cannot reliably predict the properties of nuclides with exotic N/Z ratios. For instance, nuclear models can describe the binding energies (or masses) of nuclei within the valley of stability quite well. Nevertheless for exotic nuclei different models predict very different values. The situation is similar with decay properties, nuclear shapes, and other properties of exotic nuclei, which are essential for understanding the creation of nuclei in stellar sites.

It is a key quest of modern nuclear astrophysics to find out, where, when and how the chemical elements are created in the universe, and to explain quantitatively the observed solar abundances of the elements. For the major abundances of elements beyond iron, the so-called r-, rp-, s-, p-processes have been identified. Especially the r- and p-process nucleosynthesis pathways employ exotic nuclei far off stability. As their properties determine the location of the pathway itself and the resulting abundances, reliable knowledge of these properties is essential. In return, once reliable data is known, it allows to constrain the stellar parameters of nucleosynthesis (such as densities, temperatures, etc.) and often even the astrophysical site (e.g. neutron-star merger, supernova explosion, etc.). Therefore measurements of the binding energy and the decay properties of exotic nuclei have important applications in nuclear astrophysics.

Moreover, they help to understand the structure of the nuclei. For instance, they pro-

vide important input for nuclear structure theories and various mass models and they allow tests of the shell structure and the evolution of shell effects far from stability.

In addition to the short half-lives of exotic nuclei, which are challenging for experimental techniques, these nuclei need to be produced by nuclear reactions in the laboratory. This is only possible in ultra-small quantities, in extreme cases down to one single atom per day. For their production various accelerator laboratories around the world have developed complementary approaches.

The two main production and separation schemes are the in-flight method and the ISOL method. The ISOL method features high production yields even for very exotic nuclei far from stability, but the production is subject to restrictions by chemistry and therefore only isotopes of certain elements can be studied. With the in-flight method exotic nuclei are formed via nuclear reactions from a primary beam penetrating through a thin production target. The fragments are produced and separated in-flight, remaining at high kinetic energies. This technique allows the production of exotic nuclei of all elements.

In order to utilize known low-energy high-precision techniques for the investigation of the exotic nuclei, they need to be slowed down to kinetic energies of a few eV. This approach follows the developments of the IGISOL facility in Finland during the 1980s [Arj81]. The thermalization can be achieved with a gas-filled stopping cell. The exotic nuclei are produced at relativistic energies, separated in flight, energy-bunched, slowed-down and then thermalized in a gas filled stopping cell. After extraction from the stopping cell the ions can be delivered to high-precision low-energy experiments such as mass spectrometry, laser- or decay spectroscopy. A major challenge is to achieve ultra pure conditions in the stopping gas. Only under these conditions the ions can be extracted as singly or doubly charged ions. In addition stopping cells with high area densities are needed in order to stop a large fraction of the momentum distribution of the relativistic ion beam. The experience gained at the FRS at GSI [Pet08] lead to the development of a second generation, cryogenic, stopping cell (CSC) [Ran11].

The second generation stopping cell is at the focus of this thesis. In order to use the stopping cell technique at the low energy branch (LEB) of the new fragment separator (Super-FRS) of the future Facility for Antiproton and Ion Research (FAIR) efficiently for experiments, the performance of the prototype device has been investigated in detail. The performance of the stopping cell was improved by different changes. For the first time experiments with thermalized exotic nuclei produced at 1000 MeV/u energy by in-flight fragmentation and fission of ^{238}U primary beam, such as high-precision mass spectrometry and alpha decay spectroscopy, were possible at the FRS at GSI with the prototype cryogenic stopping cell. An area density almost three times higher compared to other systems using radio frequency structures for the extraction of ions from the stopping cell could be reached. In addition the prototype cryogenic stopping cell features excellent cleanliness, which allowed the extraction of the ions of interest as a bare ions and with very low background contaminations. With the knowledge gained during this work a final cryogenic stopping cell for the LEB will

be designed and allow various types of experiments with low energy beams of exotic nuclei produced by in-flight fragmentation and fission.

A brief discussion of the research with exotic nuclei will be given in chapter 2. The basic phenomena and effects relevant for the stopping cell technique as well as the production and separation in-flight are discussed in chapter 3. In chapter 4 the design and the new concepts of the second generation cryogenic stopping cell are summarized. In chapter 5 the implementation of the novel concepts is explained in detail and attention to the additional improvements and developments compared to the first version of the cryogenic stopping cell by [Ran11] is given. The performance characteristics of the CSC is discussed in chapter 6 for ions from an offline source and in chapter 7 for ions produced by fragmentation and fission of ^{238}U in flight at the FRS at GSI.

2 Research with exotic nuclei

2.1 The scientific quest

The nucleus forms the core of the atom. It consists of protons and neutrons, these so called nucleons interact by the strong force. The nucleus is a many body system dominated by the strong force. Its mean field and central potential arises from the interactions between all constituents. Its small size, the strong forces and the many particles involved in the nucleus make it a highly complex and also unique quantum system. For this system up to now no exact solution has been developed. Understanding the structure of the nuclei on the basis of the forces and interactions between its constituents and describing its behavior and properties in theoretical frameworks is challenging. Nuclear structure physics addresses this challenge.

The nucleus is surrounded by a spherically symmetric electric field, originating from the positive charged protons of the nucleus, in which the electrons of the atom orbit. In case of a charge-neutral atom the total nuclear charge, formed by the protons, is compensated by the electrons, defining the chemical element and its chemical properties. The number of protons in a nucleus is typically labeled as Z and the number of neutrons, being charge neutral, by N. The mass number of a nucleus is given by the sum of its nucleons $A = Z + N$. Isotopes of one chemical element have the same number of protons, but different amount of neutrons, whereas isobars have the same mass number.

The mass of a nucleus $m\left({}^{A}_{Z}X_{N}\right)$ is less than the mass of its constituents and the missing mass accounts for the binding energy B_{Nuc}, which holds the nucleus together. The difference

$$B_{Nuc} = Zm_P c^2 + Nm_N c^2 - m\left({}^{A}_{Z}X_{N}\right)c^2 \tag{2.1}$$

can be calculated, where m_P and m_N are the mass of the proton and neutron [Ast20] and is in the order of $\sim$ MeV, corresponding to $1.6 \cdot 10^{-13}$ Joule. Investigation of the structure of the nucleus started with the first mass measurements by Aston [Ast20] and first mass models by Gamow, Weizsäcker and Bethe [Gam30, Wei35, Bet36].

Stable nuclei exist only in a small region among all nuclides, as indicated by the solid symbols in the chart of nuclides in figure 2.1. The light stable nuclei, e.g. ^{4}He or ^{6}Li up to ^{40}Ca, have the same amount of protons to neutrons $Z = N$. This changes for heavier nuclei up to $N/Z \sim 1.6$ for the heaviest long-lived nuclei ^{238}U, because the Coulomb

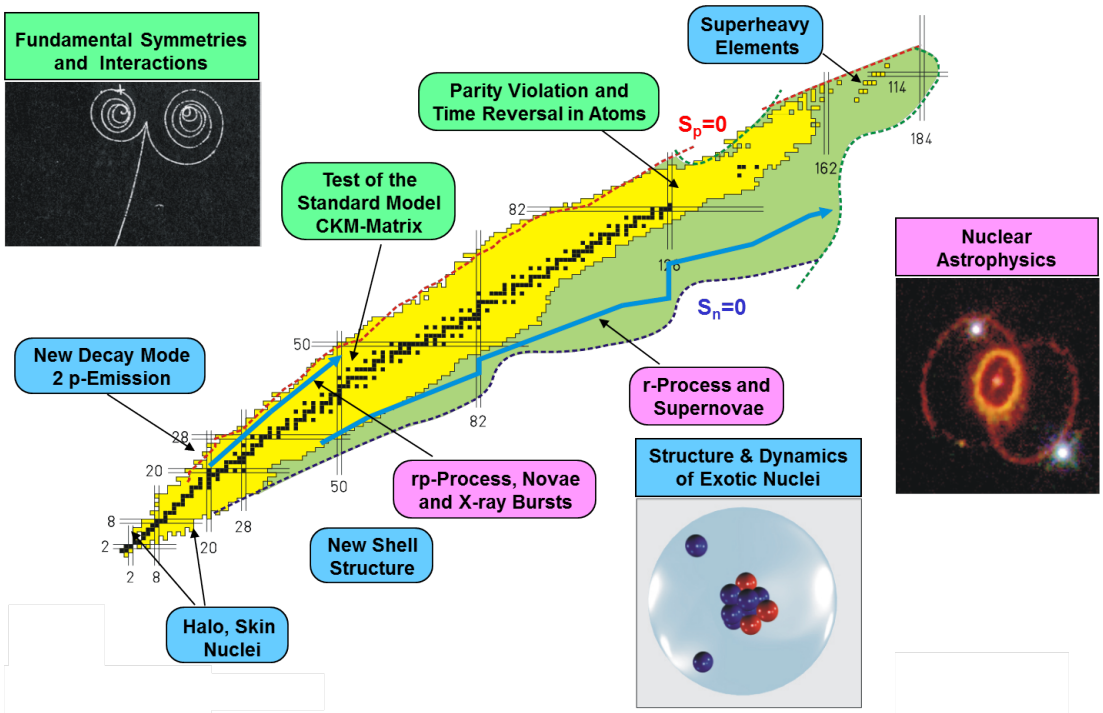

Figure 2.1: Chart of the nuclides highlighting the research possibilities with exotic nuclei for nuclear astrophysics, nuclear structure physics and fundamental symmetries and interactions [Hg].

repulsion between the protons requires more neutrons than protons in order to make the nucleus stable. In the past nuclear structure research was limited to nuclides of a small band around the stable nuclei, which have long half lifes. Nowadays radioactive beam facilities allow the production of exotic nuclei far from stability. These exotic nuclei have much larger or much smaller proton-to-neutron ratios than the stable nuclei. The study of those exotic nuclei opens new possibilities for research of nuclear structure and nuclear astrophysics, for studies of fundamental symmetries and test of the Standard Model. In figure 2.1 a chart of nuclides is shown highlighting the research possibilities concerning exotic nuclei for fundamental symmetries and interactions, for nuclear astrophysics and nuclear structure physics. These are discussed briefly in the following [CDR, Huy04].

- Nuclear structure far from stability
  A plot of the binding energy as a function of the proton and neutron numbers of the known nuclides forms the mass surface. In the mass surface structures can be seen, corresponding to the structure of the nucleus. Especially when plotting the one neutron (or two neutron) separation energy S_N (S_{2N}), the energy required to remove one (two) neutrons from a nucleus, nuclear structures effects e.g. pairing effect or shell closure, can be determined. With increasing resolving power and measurement accuracy access to additional physical effects and nuclear fine structure e.g. the deformation of the nucleus or neutron and proton halos is gained. Theoretical models can describe the properties of stable nuclei quiet well, but even today state of the art mass models fail to describe

experimental results of nuclides far from stability, as summarized e.g. in [Lun03], and more precise data is required. The study of exotic nuclei, including the production of super heavy elements, allows a test of our current understanding of the nucleus far from stability and it reveals new effects e.g. such as new decay modes, deformations modes of the nucleus or new nuclear shell structure.

- Fundamental interactions and symmetries
  Nuclear decay properties of exotic nuclei allow tests of certain aspects of the Standard Model of particle physics, as they are sensitive to the properties of the fundamental interactions. Violations of fundamental symmetries, such as parity or time-reversal can be studied with highest precision [Huy04].

- Nuclear Astrophysics
  The processes occurring in our cosmos are dominated by nuclear physics and gravity. The light elements up to iron are synthesized by nuclear reactions in stars, defining the different stellar burning stages. The nucleosynthesis of heavy elements happens in violent explosions e.g. novae, supernovae, neutron star mergers or x-ray bursts. The synthesis pathways mainly proceed within the region of unstable nuclei. In order to understand the nuclear synthesis the basic properties of the participating nuclei need to be known. For the majority of the nuclei on the r-process pathway, or close by, no experimental data is available and calculations of the r-process need to rely on the predictions of mass models. Especially around the neutron shell N=126, associated with the third r-process waiting point around A=195, little experimental information is known. These nuclides, on the pathway of the r-process before proceeding into the actinide region, are important for the normalization of the different r-process models in order to estimate the time scale, the end-point of the r-process and for estimates of the production of trans-bismuth elements.

The new Facility for Antiproton and Ion Research [**?**, FAIR] will provide new scientific opportunities for the research with exotic nuclei produced by in flight fragmentation and fission [Gei03]. High precision spectroscopy of stopped exotic nuclei will be addressed at the low energy branch (LEB). Thus well known low-energy physics techniques can be applied to nuclear physics, such as laser spectroscopy, high precision mass spectrometry and decay spectroscopy. The proposed MATS and LaSpec [Rod10] setups at the low-energy beam line as part of the NUSTAR collaboration at FAIR will allow to extend the knowledge of the properties of exotic nuclei further into the region far from stability, addressing nuclear structure and nuclear astrophysics as well as test of the standard model. The Super-FRS facility at FAIR will be one of few research facility worldwide that can produce exotic nuclei far from stability around the N=126 shell.

With its high-precision experiments MATS will give access to isomer resolution, test of the conserved vector current hypothesis and unitarity of the CKM matrix, nuclear structure and new masses, nuclear masses far from stability to test new mass models, nuclear astrophysics, spectroscopy of highly charged ions, in-trap conversion electron and alpha spectroscopy, trap-assisted and neutron spectroscopy.

The LaSpec set up will allow the determination of charge radii and nuclear moments from optical spectra, charge radii and isotope shifts and the hyperfine structure.

2.2 Production and separation of exotic nuclei

Exotic nuclei are produced by different nuclear reactions, depending on the primary beam energy and intensity, the target thickness, the production mechanism and cross section of the specific primary beam and target combination. The three main nuclear reactions are fusion, projectile fragmentation and fission.

Low energy central collisions near the Coulomb barrier lead to fusion or amalgamation of the projectile and the target nucleus. The fusion products of heavy ions are neutron deficient, because of the increased neutron excess of heavy nuclei. In addition fusion is the only reaction to create super heavy elements. The fusion reaction introduces high angular momenta and therefore high spin excited nuclear states are more likely to populate.

Compared to central collisions, peripheral collisions allow the production of target and projectile like isotopes by nucleon exchange. These collisions are well suited for production of neutron-rich isotopes of heavy elements. At the high energies only the overlapping region of the projectile and the target nucleus react by nuclear reactions with each other. The remaining heavy fragments, not part of the nuclear interaction, produce exotic nuclei of all elements. A similar process takes place by the proton-induced fragmentation, also called spallation, of a heavy target.

Nuclear fission describes the process of decay of a heavy nucleus into large fragments. The fission process can be induced by neutrons, high energy protons, heavy ions or photons. In contrast to fusion the fission process benefits from the increased neutron excess of the heavy ions and allows therefore the production of neutron-rich exotic nuclei. It can be seen as an inverse process to nuclear fusion.

For the production of exotic nuclei various accelerator laboratories around the world have developed complementary approaches. The two main production schemes are the in-flight method and the ISOL method. The principal production scheme is shown in figure 2.2. In the review articles by Blumenfeld [Blu13] and Geissel [Gei14] an overview of the current developments on production and separation techniques for exotic nuclei are given.

2.2.1 Isotope Separation On-Line – The ISOL method

In the Isotope Separation On-Line (ISOL) method, the exotic isotopes are produced by nuclear interactions of light particles impinging onto a high-Z target material.

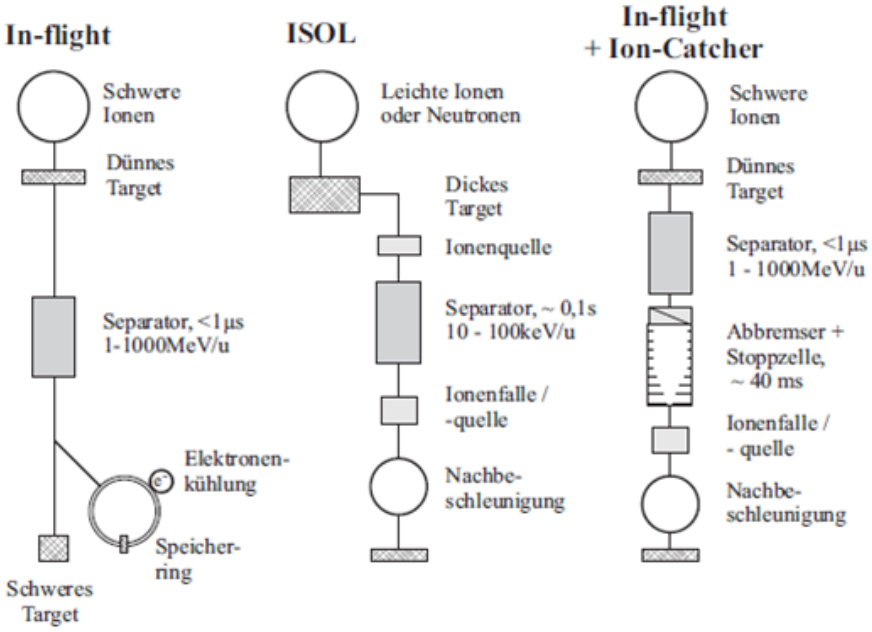

Figure 2.2: Comparison of the in flight and the ISOL technique, in addition the hybrid technique: in flight plus stopping cell is shown [Gei95].

The resulting reaction products are stopped in the bulk of the thick target (e.g. ~ 100 g/cm^2 at ISAC, TRIUMF). To be released, the atoms have to diffuse out off the inside of the target to the surface, then undergo a desorption process, until reaching the closely coupled ion source, where the neutral atoms are ionized and extracted in the form of an ion beam. The overall timescale is on the order of a few ms up to h depending on the element, thus limiting the ISOL method to exotic nuclei with half lives above several ms. To obtain the highest yields and best overall efficiency for the release out of the target to the ion source, the targets are usually operated at the highest acceptable beam power and temperature, e.g. up to 500 MeV 100 μA proton beam and 2000°C, respectively. The schematic of the production of exotic nuclei by the ISOL method is shown in figure 2.2(b).

The main challenges in the ISOL method come from the fact that the reaction products are stopped in the bulk of the target material and therefore the production is subject to restrictions by chemistry, e.g. refractory elements are hard to produce. This can be seen in the lower part of figure 2.3. Here, as an example, the ISOLDE yield data base is compared to current predictions for the production of exotic nuclei at the Super-FRS. The limitation of the ISOL method to certain elements can be seen.

The most direct method to increase the intensity of the secondary beam of exotic nuclei is to increase the driver beam intensity. Another method is the use of an indirect ISOL method, where a secondary particle beam (e.g. neutrons or γ's) interacts with a fissile target. This allows a decoupling of the power deposition in the system and the ISOL target. Therefore the ISOL-target can be operated at much lower power while the converter can be cooled without affecting the target temperature. Thus the efficiency

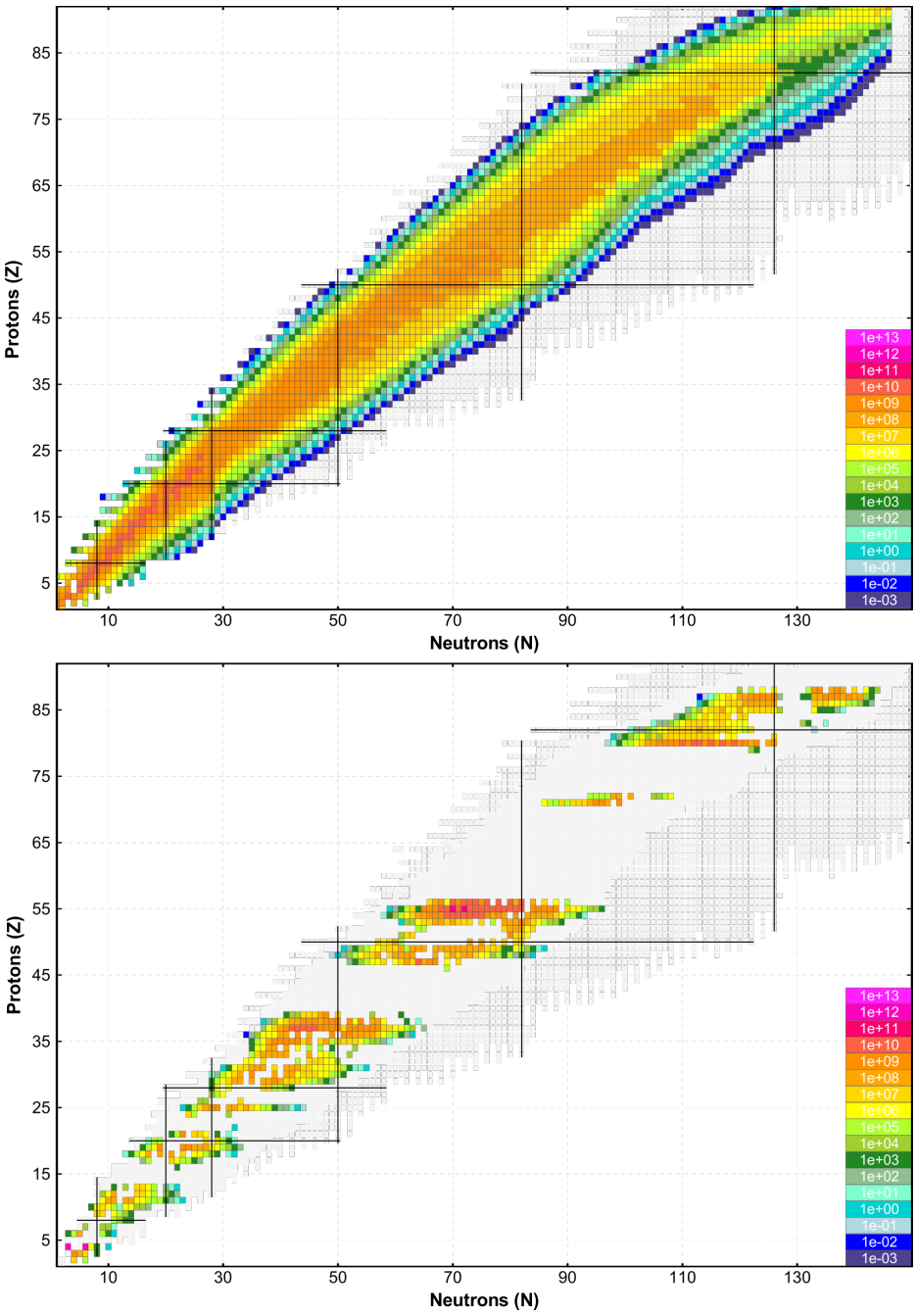

Figure 2.3: Chart of the nuclides showing the possible production of exotic nuclei at the Super-FRS [Pie15] as an example of an in-flight facility (top) and at ISOLDE [ISOLDE] as an example of an ISOL facility (bottom) down to productions yields of one exotic nuclei per minute.

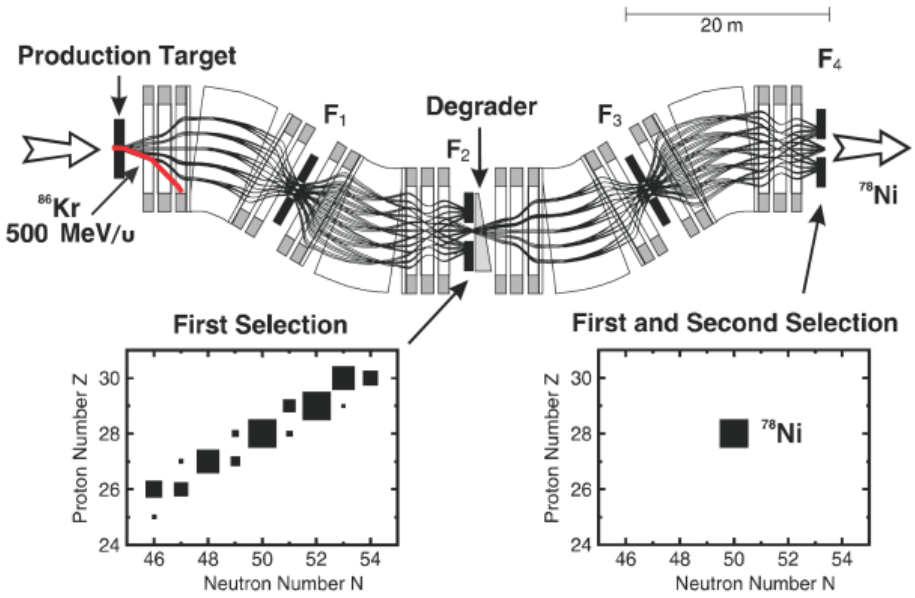

Figure 2.4: Separation method of the fragment separator (FRS) using the $B\rho - \Delta E - B\rho$ method with an intermediate degrader for the production of a ^{78}Ni secondary beam [Gei92, Pet08b].

of the release of the radioactive atoms from the target can be increased. The indirect ISOL method can reach the highest primary beam powers, but is mainly limited to fission products.

2.2.2 The In-flight method

In the in-flight method isotopes are produced by in-flight fusion, in-flight projectile fragmentation or in-flight fission of heavy ions, as indicated in figure 2.2(a). Fragmentation and fission can be achieved by steering a heavy, high energetic primary beam onto a target being thin compared to the range of the primary beam (e.g. $1-10$ g/cm^2 Be at 1000 Mev/u at FRS, GSI). Primary beams with energies near the Coulomb barrier can be used to produce exotic nuclei by fusion of the projectile and the target nucleus. The reaction products are able to penetrate through the target and can be transported through an ion optical system with high kinetic energies. The produced cocktail beam can then be separated using magnetic and electric fields e.g. velocity filters.

At relativistic energies the usage of electric fields is not possible and the separation needs to be performed based on magnetic fields and the element-specific energy-loss in matter. This approach makes use of the fact that the produced fragments are fully ionized at high energies and that the induced energy loss and angular straggling only result in a small phase-space enlargement. The separation is realized by placing a specially shaped energy degrader at the dispersive intermediate focal plane of an achromatic magnetic separator system. In this case the first stage of the separator

provides A/Z selection, because the momentum distribution of the projectile fragments is narrow, as the energy loss straggling in peripheral nuclear collisions is small. The second magnetic dipole stage separates the remaining cocktail beam to which an energy loss (ΔE) was introduced by the degrader. The energy loss depends on the nuclear charge and therefore allows a selection of a narrow range of fragments, thus producing clean secondary beams. In figure 2.4 the production and separation of a ^{78}Ni secondary beam at the FRS is illustrated. This separation scheme at relativistic energies is called $B\rho-\Delta E-B\rho$ method and can be used to produce exotic nuclei of all elements-independent of their chemical properties; same holds for in-flight separators using fusion reactions for the production of exotic nuclei. The in-flight method has been used successfully at the fragments separator (FRS) at GSI for experiments with exotic isotopes of all elements [Gei92]. In addition the in-flight production can provide exotic nuclei with half lives down to $\sim$ 100 ns, only being limited by the time-of-flight through the ion optical system.

In order to achieve higher yields for secondary beams, the primary beam intensity can be increased. In addition the transverse momentum acceptance of the magnetic separator can be enlarged. This will be used at the future Super-FRS at FAIR, increasing the momentum acceptance of the in-flight separator from 1% up to 2.5% resulting in a gain of about a factor of 30 for e.g. ^{78}Ni [Gei03].

In the upper part of figure 2.3 the current predictions for the production of exotic nuclei at the Super-FRS is compared to the ISOLDE yield data base. The figure points out that the in-flight method can produce exotic nuclei throughout the nuclear chart.

2.2.3 In-flight plus stopping cell – hybrid-systems

A possible disadvantage of the in-flight method is that the exotic nuclei have high kinetic energies and occupy a large phase volume. However, precision low-energy experiments of exotic nuclei as well as the re-acceleration of exotic nuclei require small emittance beams of low energy. In particular, studies with ion and atom traps need ion beams with kinetic energy of less than a few tens of keV with emittances down to a few π mm mrad and energy spreads smaller than 10 eV.

With the complete slowing-down of the in-flight reaction products in a gas-filled stopping cell [Schw03, Wad03, Sav03] the advantages of the ISOL and the in-flight techniques can be combined. This approach was pioneered in the early 1980s in the Ion Guide Isotope Separator On-Line (IGISOL) systems [Arj85]. For a recent historic overview of the development of stopping cells see [Wad13].

Stopping of nuclei produced at relativistic energies in a gas cell is particularly challenging because of the large phase space of the relativistic ion beams. In order to stop a reasonable fraction of the secondary beam a reduction of the energy spread in a dispersive magnetic stage a so called monoenergetic degrader system is required

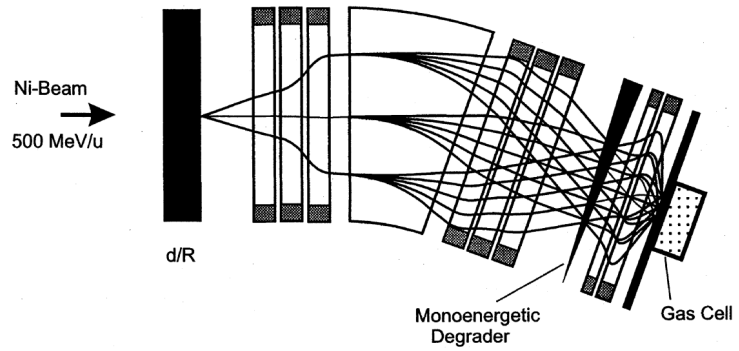

Figure 2.5: Range compression by a dispersive magnetic stage and a monoenergetic degrader of ^{78}Ni secondary beam in order to efficiently stop ions in a gas cell [Gei89, Wei00A].

[Gei89, Wei00A, Sche03].

This technique is called energy bunching. A high energetic secondary beam is passed through a dispersive magnetic stage, which allows a translation of the momentum spread into a spacial separation. Using a monoenergetic degrader it can be achieved, that ions, which are faster than the reference ion on the ion optical axis, need to travel through more material compared to slower ions. Choosing the correct shape for the monoenergetic degrader allows the production of an almost monoenergetic secondary beam. The concept is illustrated in figure 2.5. Combining the technique of energy bunching with a high-density stopping cell the conversion of high energy secondary beams in low-energy radioactive beams with total efficiencies of a few percent.

A schematic view of a possible realization of the stopping cell is shown in figure 6.1. A monoenergetic radioactive beam of high energy enters the volume of the stopping cell through several thin beam windows. The beam is separated beforehand and its momentum spread is reduced by range bunching [Gei89, Wei00A, Sche03]. The exotic nuclei loose energy and finally thermalize in the buffer gas volume of the stopping cell. Noble gases such as helium or argon are typically used as stopping gas. Stopping cells relying on the neutralization of the ion of interest typically use argon, where as stopping cells based on the extraction of charged ions use mainly helium. Once the ions of interest are stopped a homogenous longitudinal electric field pulls them to the extraction side of the stopping cell, on the right side of figure 6.1. In order to prevent the ions from hitting the chamber walls a radio frequency structures are positioned at the extraction side of the stopping cell and produce a pseudo potential wall. A superimposed radial DC field transports the ions towards an extraction nozzle. When reaching the vicinity of the nozzle, the gas flow dominates the ion transport and flushes the ions from the high pressure stopping region into a low pressure beam line. In order to reach a high pressure gradient between the stopping volume and the low pressure beam line extraction nozzles in the order of $\oslash \sim 1$ mm are used. For efficient ion confinement in the first differential pumping section typically RFQ's or higher order multipole ion guides, such as sextupole or octupole ion guides, are used.

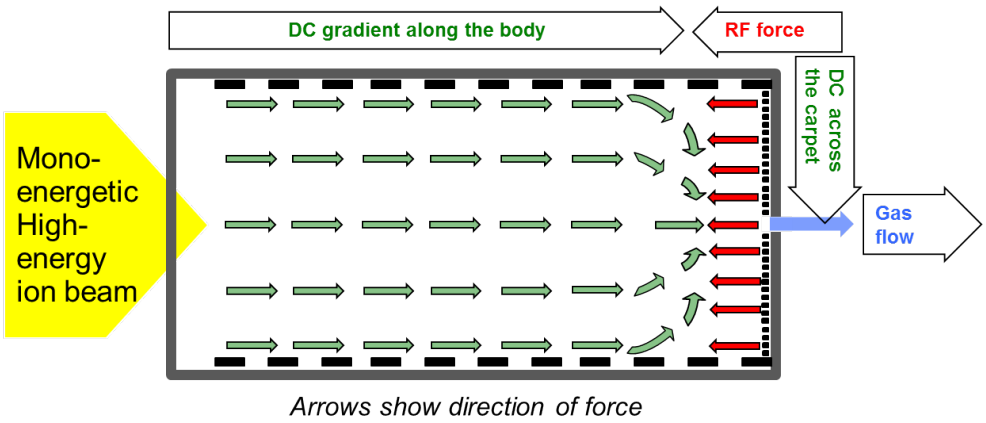

Figure 2.6: Schematic view of the forces acting on the ions inside a stopping cell. In green the homogenous longitudinal DC field along the body of the stopping cell and the radially focusing DC field are shown. In red the effective field of the RF structure, repelling the ions from hitting the surface of the electrodes, is shown. The gas flow is indicated in blue, flushing the ions from the extraction region into a low pressure beam line through an extraction nozzle.

The key performance parameters of stopping cells for exotic nuclei are their efficiency and extraction time. The total efficiency can be split up in the stopping efficiency and the extraction and survival efficiency. The stopping efficiency represents the fraction of the momentum distribution of the incoming high energy beam, that can be stopped inside the stopping cell. The survival and extraction efficiency describes the fraction of the stopped ions which get extracted from the stopping cells as bare ions. A challenge of the stopping cell technique is to achieve ultra pure conditions in the buffer gas of the stopping cell. Only under these conditions ions can be transported in the buffer gas as singly or doubly charged ions. In addition it becomes possible to extract the exotic nuclei without adducts. After extraction from the stopping cell the exotic nuclei can be formed into a low energy beam of high brilliance. A schematic view of the full in-flight plus stopping cell technique can be seen in figure 2.2(c).

3 Basics of hybrid-systems

In the following the basic ideas and concepts will be described relevant for the usage of the in-flight plus stopping cell technique for high precision experiments. The isomer production by relativistic in-flight fragmentation of ^{238}U is given special emphasis as fragmentation is the main production mechanism for the studied heavy nuclides in the region above lead. These nuclides were thermalized in a cryogenic stopping cell and extracted from the stopping volume. The physical processes involved in the slowing-down from relativistic to thermal energies and in addition the ion motion inside the stopping cell and in the low energy RFQ based beam line are discussed.

3.1 Population isomeric states by in-flight fragmentation

In 1917, Soddy predicted nuclei with same mass number and chemical properties but with different decay properties [Sod17]. These nuclei were described by Weizsäcker as long-lived excited nuclear states, with half-lives above $\sim$ 1 ns [Wei35]. They are referred to as isomers. Weizsäcker indicated that these excited states exist, if the difference in total angular momentum between the isomeric and the lower-lying ground state is large. In this case the gamma de-excitation would have a high multipolarity. These kinds of transitions have a low probability and therefore the excited nuclear states would becomes metastable.

The excitation energy of isomeric states varies between a few eV (in ^{229m}Th), up to several MeV (in ^{211m}Po) and they can have half lives ranging from only a few ns (in ^{212m}Po) to more than 10^{15} a (in ^{180m}Ta). Isomers are of great interest themselves as they give access to the shell structure of the nucleus and allow tests of nuclear structure models. In addition the production of isomeric states gives an insight into the processes occurring during their production in fragmentation, fission or fusion reactions. The measurement of isomeric ratios can be used to probe the understanding of the fragmentation process in peripheral heavy ion collisions at relativistic energies. In order to efficiently use in-flight fragmentation at future radioactive beam facilities its properties need to be studied and understood.

The fragmentation process can be described by a two-step abrasion-ablation model [Eis54, Bow73, Hue75]. In this description, during a first dynamic fast abrasion process nucleons are removed from the target and the projectile nucleus. By this a target-like

and a projectile-like prefragment are produced. In a second statistical slow ablation stage of the process the excited prefragment deexcites in an evaporation cascade. The energy and the linear momentum distribution in those fragmentation reactions have been investigated in detail e.g. by [Oli1979, Gol74, Web94]. The angular momentum distribution has been described in the abrasion-ablation model by Jong [Jon97].

Jong considers the angular momentum distribution in analogy to the linear momentum distribution of the fragmentation process by Goldhaber [Gol74]. A spin-cutoff parameter σ_f acts as a measure for the width of the distribution and can be written as

$$\sigma_f^2 = \left\langle j_z^2 \right\rangle \frac{A_{pf}(A_p - A_{pf})}{A_p - 1}, \tag{3.1}$$

with the mass number A_{pf} and A_p of the prefragment and the initial projectile, and with the average square value of the angular momentum projection $\langle j_z^2 \rangle$ of a nucleon in the nucleus [Gai91]. The value of $\langle j_z^2 \rangle$ can be calculated from the shell model by

$$\left\langle j_z^2 \right\rangle = k \cdot A_p^{2/3} \left(1 - \frac{2}{3}\beta\right), \tag{3.2}$$

with the quadrupole deformation parameter β of the projectile and a numerical constant k which is in the order of 0.16 [Jon97].
The distribution of the angular momentum P_I is described in the form

$$P_I = \frac{2I+1}{2\sigma_f^2} \exp\left[-\frac{I(I+1)}{2\sigma_f^2}\right], \tag{3.3}$$

as a function of the spin I.

After the abrasion stage the excited prefragment will deexcite. The angular momentum removed in the evaporation cascade may be neglected because of the low angular momentum values involved. Therefore the angular momentum distribution of the final fragment can be written as a superposition of the angular momentum distribution of the different prefragments, which contribute to the production of the final fragment in different evaporation chains.

The nuclear collision induces an average excitation energy of about 27 MeV per abraded nucleon [Schm93], which allows the assumption that the number of evaporated nucleons ν is proportional to the mass loss induced by the abrasion stage. In this context $\bar{\nu}$ is the average number of evaporated nucleons per abraded mass unit. The spin cutoff parameter σ_f can thus be written as

$$\sigma_f^2 = 0.16 \cdot A_p^{2/3} \left(1 - \frac{2}{3}\beta\right) \frac{(A_p - A_f)(\bar{\nu}A_p - A_f)}{(\bar{\nu}+1)^2(A_p - 1)}, \tag{3.4}$$

with the final fragment mass A_f and the projectile mass A_p. $\bar{\nu}$ can be assumed to be close to 2, because the excitation energy decreases by about 13 MeV per evaporation step. In this case typical angular momenta between $3\hbar$ and $10\hbar$ are reached

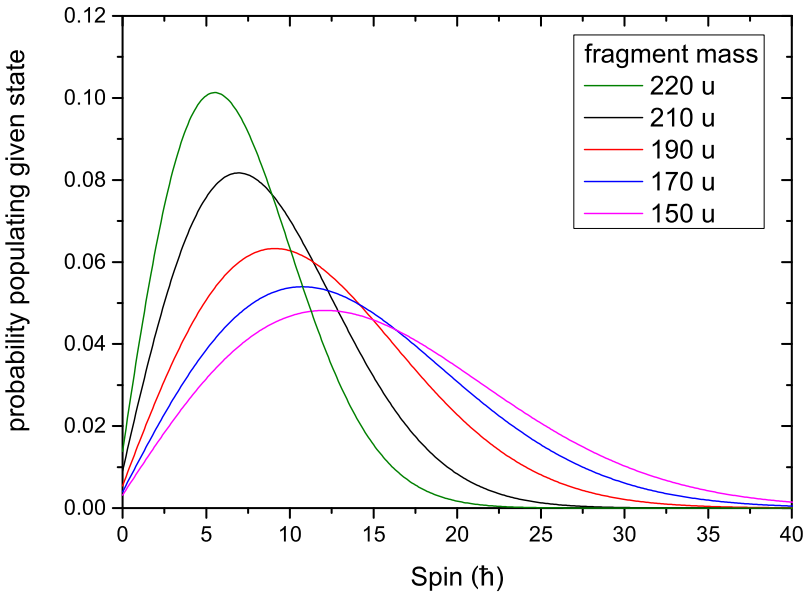

Figure 3.1: Calculated angular momentum distribution of the final fragment produced by ^{238}U fragmentation at relativistic energies in the two-step abrasion-ablation model [Jon97]. The distribution is calculated using eq. (3.3) and (3.4) for fragments with different mass number A_f. A average number of evaporated nucleons per abraded mass unit of $\bar{\nu} = 2$ was used for the calculation.

[Gai91]. A calculation for the angular momentum distribution of the final fragment is shown in figure 3.1 for fragments with different mass A_f produced by fragmentation of ^{238}U beam. The angular momentum distribution gets broader if the mass difference between the initial projectile and the fragment increases.

In order to give predictions for the production of the final fragment in its ground or isomeric state, the γ deexcitation has to be taken into account following the ablation. One can assume that the excited final fragment is produced covering a certain energy-spin region, as shown in figure 3.2. From this high excitation energy and high spin region the fragment deexcites by γ emission down to the Yrast line.

At the Yrast line all excitation energy is stored as rotational energy E_{rot}, following

$$E_{rot} = \frac{\hbar^2}{2\theta} I(I+1), \tag{3.5}$$

for a nucleus with moment of inertia θ and angular momentum I [May79]. Calculating the Yrast line requires knowledge of the shape of the nucleus in order to calculate the moment of inertia of the nucleus.

For a spherical nucleus of mass A_f the momentum of inertia can be calculated

$$\theta = \frac{2}{5} m_0 r_0 A_f^{5/3}, \tag{3.6}$$

with the mass of a nucleon m_0 and the nuclear radius r_0 [May79].

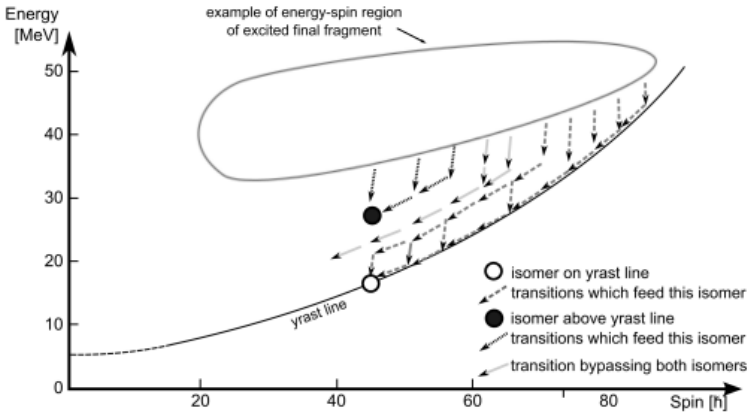

Figure 3.2: A schematic drawing showing the possible path of the γ de-excitation from the entry region of the fragment to the finally measured isomeric states and ground state. [Mya12]

If the level scheme is known it is possible to calculate the effective moment of inertia backwards from the energy difference ΔE between two levels

$$\theta = \frac{\hbar^2}{2}\frac{\Delta I(I+1)}{\Delta E} = \frac{\hbar^2}{2}\frac{I(I+1)-(I-2)(I-1)}{E_I - E_{I-1}} = \frac{\hbar^2}{2}\frac{4I-2}{E_I - E_{I-2}}, \tag{3.7}$$

for the above calculation an angular momentum difference of $\Delta I = 2$ was assumed [May79].

If the excited states are close to the Yrast line they are referred to Yrast states. These states tend to decay along the Yrast line, feeding the closest lower-lying isomeric state. Excited states above the Yrast line have the possibility to by-pass a certain isomeric state because of their higher excitation energy.

The current models only describe the energy-spin distribution in the entry channel, but not the deexcitation. Simple cut-off approaches can be used to describe the relative population of isomeric states compared to the ground state. In the sharp cut-off approach it is assumed that all states with higher spin compared to an isomeric state will deexcite into this state, while possible by-passing of the state is ignored. This assumption holds for Yrast-states, because the gamma deexcitation only removes small angular momentum from the excited nucleus, because of the low multipolarity. Integration over the momentum distribution P_I between the isomeric state and the maximum of the distribution provides an upper limit for the fraction R_{th} of production of a certain isomeric state with spin I_m

$$R_{th} = \int_{I_m}^{\infty} P_I \; dI = \exp\left[-\frac{I_m(I_m+1)}{2\sigma_f^2}\right]. \tag{3.8}$$

On the left hand side of figure 3.3 the sharp cut-off approach is illustrated for ^{211}Po and the population of its $(9/2^+)\hbar$ ground state, $(25/2^+)\hbar$ and $(43/2^+)\hbar$ excited states by in-flight fragmentation of a ^{238}U primary beam at 1000 MeV/u.

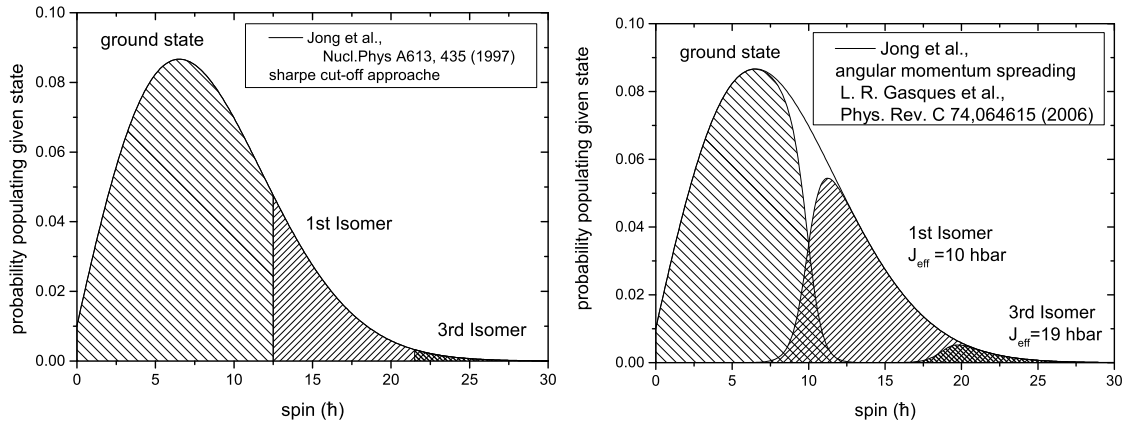

Figure 3.3: Illustration of the sharp-cut-off approach (left side) and an empirical state mixing approach (right side) for the calculation of the isomer ratio from the calculated angular momentum distribution for ^{211}Po produced by fragmentation of ^{238}U.

In the spin-mixing approach, following the assumption of Gasques, an empirical state mixing is introduced [Gas06]. The introduced effective angular momentum cut-off J_{eff} accounts for a spread in the angular momentum distribution, due to the neutron evaporation and the cascade of gamma rays from the initial compound nucleus to the final state [Gas06]. With the spreading parameter δ the angular momentum distribution associated with the ground sate $\sigma_I^{(0)}$ and an isomeric state $\sigma_I^{(1)}$ can be calculated:

$$\sigma_I^{(0)} = \frac{\sigma_I}{1 + \exp\left(\frac{J_{eff} - I}{\delta}\right)} \tag{3.9}$$

$$\sigma_I^{(1)} = \frac{\sigma_I}{1 + \exp\left(\frac{I - J_{eff}}{\delta}\right)}, \tag{3.10}$$

with σ_I as the total angular momentum distribution. The spreading parameter δ in the Fermi function describes the extend of the spreading of the angular momentum around the effective cut-off J_{eff}. In order to account for the angular momentum of the neutrons and gamma rays. Reasonable values for δ and J_{eff} can be choose as in [Gas06] to $\delta = 0.5$ and $J_{eff} = 10\hbar$. The empirical spin mixing following this approach is shown on the right hand side of figure 3.3. Integration over the individual angular momentum distributions of the ground sate $\sigma_I^{(0)}$ and an isomeric state $\sigma_I^{(1)}$ leads to the isomer ratio.

The mentioned approaches are only valid for Yrast-states, therefore knowledge of the level scheme of the fragment is important for the calculation of isomeric states and ratios [Mya12]. In addition knowledge about the structure of the nucleus and its properties is required.

3.2 Decay spectroscopy and Q-value measurements

Experimentally nuclear structure can be studied by measuring the properties of exotic nuclei by various experimental techniques. high-precision mass measurements allow a determination of the binding energy of exotic nuclei, gamma spectroscopy gives an insight into the level scheme of the exotic nucleus. Complementary methods to high precision mass measurements are decay studies and nuclear reaction studies of exotic nuclei. Measuring the amount of energy, the Q-value, released by a nuclear reaction or decay

$$a + A \rightarrow b + B \tag{3.11}$$

where a, A are the reactants, b, B are the products and m_a, m_A, m_b and m_B are their masses respectively, the Q-value is defined as

$$Q = [(m_a + m_A) - (m_b + m_B)]\, c_0^2. \tag{3.12}$$

Knowing the mass of three participants and the Q-value the mass of the remaining one can be calculated. The Q-value can also be measured if the kinetic energy of all participants is detected [Hof79].

The main nuclear decay types are α-decay, β^+ and β^--decays. In case of an α-decay from a parent nucleus to a daughter nucleus the Q-value results to

$$Q_\alpha = m_{Parent}c_0^2 - m_{Daughter}c_0^2 - m_\alpha c_0^2, \tag{3.13}$$

with the mass of the parent m_{Parent}, the daughter $m_{Daughter}$ and the α particle m_α. The α particles emerges from the decay with a kinetic energy $E_{kin,\alpha}$, which is below the value of Q_α, because of momentum conservation. The momentum of the α particle and the recoiling daughter nucleus are classically

$$\begin{aligned} p_\alpha &= \sqrt{2m_\alpha\, E_{kin,\alpha}} \\ p_{Daughter} &= \sqrt{2m_{Daughter}\, E_{kin,Daughter}}, \end{aligned} \tag{3.14}$$

respectively. The mother nucleus being at rest, implies momentum conservation and therefore $p_\alpha + p_{Daughter} = 0$. Substituting this with equation (3.13) leads to the kinetic energy of the α particle

$$E_{kin,\alpha} = \frac{m_{Daughter}}{m_{Parent}} Q_\alpha, \tag{3.15}$$

with the mass number of the daughter nucleus A. For the above calculation the electron binding energy was neglected. Sometimes α particles are measured with a somewhat lower energy. In this case the α decay results with a daughter nucleus in an excited state and is accompanied by emission of γ rays.

Conversely, the parent nucleus can α decay from an excited state. In this case an α energy higher than the Q_α value can be detected. The difference amounts to the excitation energy of the excited state. This shows already the disadvantage of measuring the Q-value compared to direct mass measurements, since all decay products and possible excited states have to be known in detail.

3.3 In-flight separation and kinematics

Magnetic fields are used in particle and accelerator physics for deflection, analysis and separation of ion beams. For energy momentum measurements or momentum selection dipole magnets are mainly used. Higher order magnetic fields, such as quadrupole, sextupole and octupole fields are used for focusing or correction of higher order aberrations.

The trajectories of a charged particle with charge q, mass m and velocity v in a homogenous magnetic dipole field of strength B can be calculated using the Lorentz- and centripetal force leading at non-relativistic energies to

$$\rho = \frac{mv}{qB}. \tag{3.16}$$

In this scenario the magnetic field is perpendicular to the direction of motion of the ion. The ion will be forced on a circular trajectory with radius ρ.

If a cocktail beam of different ion species is traversing through a dipole field it will split up according to the momentum-over-charge ratio of the particles. The magnetic rigidity χ can be used for the characterization of the particles at relativistic energies

$$\chi = B\rho = \frac{m}{q} c_0 \beta\gamma, \tag{3.17}$$

with the velocity of light c_0, $\beta = v/c_0$ and the Lorentz factor γ.

At non-relativistic energies electric fields can be used for the deflection of ions. Combining magnetic and electrostatic fields allows the construction of a double focusing sector field for mass separation with a mass resolving power R of up to several ten thousands.

However at relativistic energies electrostatic fields are no longer sufficient and the separation has to rely on magnetic fields only. The energy loss can be used in addition to the magnetic fields and allows the construction of powerful fragment separators based on the $B\rho - \Delta E - B\rho$ technique, because the energy loss in material of an ion is proportional to its nuclear charge. The energy loss will be described in the next section in detail.

3.4 Slowing down of relativistic heavy ions in matter

For the construction and operation of fragment separators based on the $B\rho - \Delta E - B\rho$ method it is critical to know the energy loss of ions in matter precisely. Only then the fragment separator can be used for the production of pure secondary beams and a clear identification of the ions becomes possible.

In general if a monoenergetic beam of charged particles penetrates through matter, after the material all particles will have lost energy, some changed their direction or e.g. picked up or lost an electron. In addition the energy distribution of the beam will be broadened.

3.4.1 Energy loss

In a more qualitative description, the energy loss dE per unit of distance dx the ions penetrating through the material is defined as

$$\frac{dE}{dx}(E) = \lim_{\Delta x \to 0} \frac{\Delta \langle E \rangle}{\Delta x}. \tag{3.18}$$

In the classical description following Bohr [Boh13] the energy loss of the ion beam takes place through many inelastic collisions with the target. According to Bohr the probability to lose a certain energy T_i in a single collision can be calculated from the target thickness $N\Delta x$ and the cross-section σ_{T_i}. Integration over all possible energy losses T_i in a single collision allows determination of the mean energy loss

$$\langle \Delta E \rangle = N\Delta x \int \sigma_T \; dT, s \tag{3.19}$$

with σ_T the differential cross-section as a function of the transferred energy T.

The stopping cross section S is defined as

$$S = \int T \; d\sigma \tag{3.20}$$

from which Bohr derived its energy loss formula [Boh13]

$$S = \frac{4\pi Z_1^2 Z_2 e^4}{mv^2} \cdot \ln\left(\frac{1.123 \; mv^3}{2\pi Z_1 e^2 \omega_0}\right) \tag{3.21}$$

for the interaction of an ion with charge $Z_1 e$, mass m, velocity v and with the electrons of a target nucleus being at rest with charge Z_2, with $\omega_0/2$ being the mean circulation frequency of the electron of the target nucleus.

Bohr treated the stopping process classically, whereas in the Bethe approach quantum mechanical perturbation theory is used for the description of the energy loss [Bet30]. Bethe uses a first order Born approximation, which results in the know Bethe formula

$$S = \frac{4\pi Z_1^2 Z_2 e^4}{mv^2} \cdot \ln\left(\frac{2mv^2}{I}\right) \tag{3.22}$$

with the mean ionization potential I, corresponding to the average of all excitation and ionization energies of the target atoms. For light target nuclei this can be calculated according to

$$\ln(I) = \frac{1}{Z_2} \sum_n f_n \ln(E_n - E_0), \tag{3.23}$$

from the atomic level scheme with the energies E_n and E_0. For heavy nuclei a calculation of the mean ionization potential becomes challenging and is in most cases not possible.

In the literature typically the Bethe formula is written as

$$S = \frac{4\pi Z_1^2 e^4}{mv^2} \cdot Z_2 L_{(v,Z_2)} \tag{3.24}$$

where $L_{(v,Z_2)}$ is called the stopping number

$$L_{(v,Z_2)} = \ln\left(\frac{2mv^2}{I}\right). \tag{3.25}$$

Bethe [Bet32] and Møller [Møe32] extended the Bethe formula for projectiles with relativistic velocities. Lindhard and Winter [Lin63] showed that a term with $-\ln(1-\beta^2)-\beta^2$ needs to be added to equation (3.25). This results in the stopping number

$$L_{(v,Z_2)} = \ln\left(\frac{2mc^2\beta^2\gamma^2}{I}\right) - \beta^2, \tag{3.26}$$

which is referred to as the Bethe stopping number L_{Bethe}.

In order to describe experimental values with higher precision, additional corrections need to be added to the Bethe stopping number.

The *density effect* arises from a change of the field which perturbs the electrons far from the projectile track by a dielectric polarization of the atoms between the distant electron and the projectile. This effect in dense media was calculated in classical electrodynamic theory by Fermi [Fer40] and later by Sternheimer and Peierls [Ste71]. The correction is historically written as $\frac{\delta}{2}$ and results for high energies in

$$\frac{\delta}{2} = -\ln(\beta\gamma) + \ln(\frac{1}{\hbar\omega_p}) + \frac{1}{2} \tag{3.27}$$

with ω_p as the plasma frequency of the medium. The density effect reduces the rise at relativistic energies from $\sim \ln(\gamma^2)$ to $\sim \ln(\gamma)$. At low energies the density effect can be described by a parametric fit to the full density effect [Ste71].

The *Barkas effect* was discovered by a measurement of the range of positively charged pions compared to negatively charged pions [Bar63]. The range of positively charged particles is reduced because of dynamic screening which leads to a reduction of the effective collision velocity. The contribution of the Barkas effect to the stopping number decreases with $1/\gamma^2$ and is important only at non relativistic energies [Lin76].

In addition at low energies *shell corrections* need to be taken into account because the energy transfer becomes less efficient when the projectile velocity reaches or undershoots the orbital velocity of the bound target electrons. This correction to the Bethe stopping number also scales with $1/\gamma^2$ and can be ignored at relativistic energies.

Bloch investigated the validity of the classical and quantum mechanical treatment of the stopping power and showed that independent of the projectile charge a first-order perturbation treatment is sufficient to describe distant collisions [Blo33]. However at small impact parameters, the exact scattering amplitudes for a Coulomb field have to be used in comparison to the first Born approximation [Bet30]. Bloch calculated a correction

$$\Delta L_{Bloch} = \Psi(1) - Re\Psi(1 + iZ_1\alpha/\beta) \tag{3.28}$$

where Ψ is the logarithmic derivative of the complex gamma function. The Bloch correction is valid for relativistic as well as for non relativistic energies.

At large impact parameters Bloch and also Bethe still use the first-order Born approximation for the scattering cross section $\sigma_{1.Born}$. In other words, the binding energy of the target electrons is neglected and the cross section for free electrons is used. For elements with high nuclear charge this is no longer valid and the Born approximation deviates considerable from the exact cross section, which can be described better by the Mott cross section σ_{Mott} [Mot29, Mot32]. This deviation results in the *Mott correction* to the Bethe stopping number. The Mott correction only plays a role for high Z_1 and at high β. It is in the order of

$$\Delta L_{Mott} \propto \int \sin^2(\Theta/2)[d\sigma_{Mott} - d\sigma_{1.Born}], \tag{3.29}$$

with Θ as the center of mass scattering angle.

In the above description only point-like charges were taken into account, which is not a good approximation for relativistic heavy ions. Lindhard and Sørenson include the charge distribution of the projectile [Lin96] and it was shown in [Sche94] that a correction term according to Lindhard and Sørenson has to be added to the Bethe stopping. In addition exact solutions are used for the Dirac equation, this means that the LS approach has in principal the Bloch and Mott correction included automatically.

$$\Delta L_{LS} \propto \int \sin^2(\Theta/2)[d\sigma_{fns} - d\sigma_{point}] \tag{3.30}$$

This correction accounts for the difference in cross section between a point-like nucleus (σ_{point}) and a realistic nucleus with finite size (fns) σ_{fns}.

For bare relativistic ions the correction terms for the Barkas effect and the shell correction can be neglected and the stopping power can be written as

$$S = \frac{4\pi Z_1^2 e^4 \mathcal{N}}{mc^2\beta^2} \cdot \left(L_{Bethe} + \Delta L_{Bloch} + \Delta L_{Mott} + \Delta L_{LS} - \frac{\delta}{2} \right) \tag{3.31}$$

where $\mathcal{N}$ is the number of target electrons per unit volume, according to the nomenclature made in [Sche98]. The Bloch and Mott correction are listed in eq. (3.31) for their importance, but are included in principal in the LS theory.

The energy loss is dominated at high energies by electronic stopping and at low energies nuclear stopping plays a major role. The stopping power and therefore the

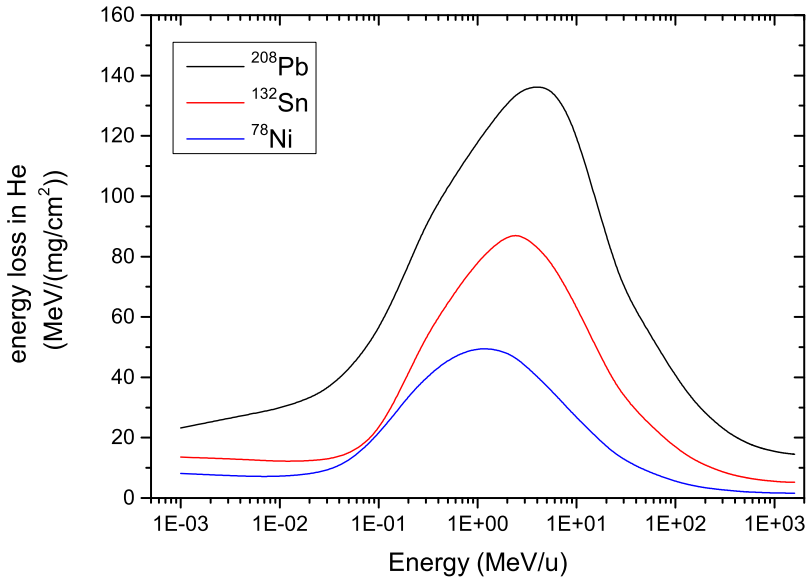

Figure 3.4: Energy loss of ^{208}Pb, ^{132}Sn and ^{78}Ni in He gas as a function of kinetic energy. Calculations of the resulting stopping power were taken from [ATIMA].

energy loss is reduced for light projectile ions, which makes stopping of light ions in a gas filled stopping cell particularly challenging. In figure 3.4 the energy loss of ^{208}Pb, ^{132}Sn and ^{78}Ni in He are plotted as a function of the projectile energy between 1 GeV/u to 1 keV/u.

3.4.2 Energy loss straggling

If a monoenergetic ion beam passes through material, in addition to the absolute energy loss, described above, its momentum distribution will be broadened. This broadening is refereed to as energy loss straggling.

The energy loss straggling Ω can be calculated as the mean square of the energy loss

$$\Omega^2 = \left\langle (\Delta E - \langle \Delta E \rangle)^2 \right\rangle = N \Delta x \int \sigma_T \; T^2 \; dT. \tag{3.32}$$

Following this approach Bohr derived the energy loss straggling Ω to

$$\Omega^2 = 4\pi \cdot Z_1^2 Z_2 e^4 \cdot N \Delta x \tag{3.33}$$

for a target with thickness $N\Delta x$ and number of atoms N [Boh13].

The energy loss straggling was treated by Lindhard and Sørenson similar to their description of the energy loss for relativistic heavy ions in mater and results in

$$\Omega^2 = 4\pi Z_1^2 Z_2 e^4 \mathcal{N} \Delta x \gamma^2 \cdot X \tag{3.34}$$

where

$$X = \left(1 - \frac{v^2}{2c^2}\right) \tag{3.35}$$

is the straggling parameter in a first order Born approximation following [Lin96]. This type of energy loss straggling is often referred to as collisional energy straggling.

In addition charged particles can change their charge state while penetrating through matter by electron capture or ionization processes. A change in charge state has a strong effect on the stopping power and therefore the so called charge-exchange straggling can substantially increase the energy loss straggling and has to be taken into account [Wei00B, Wei02].

3.4.3 Range and range straggling

For the stopping of relativistic heavy ions produced at in-flight facilities in gas filled stopping cells and their usage for low energy high precision experiments in addition to the stopping power, the range of the charged particles is of interest. The range can be derived by an integration over the full slowing down and stopping process of heavy ions in matter from their initial kinetic energy E to rest

$$R = \int_0^E \frac{dE}{S(E)} \sim \frac{A}{Z_1^2}. \tag{3.36}$$

In a coarse approximation the range is proportional to the projectile mass A and inversely proportional to the square of the projectile charge Z_1, following from substituting equation (3.31) above. The energy loss straggling translates into a range straggling respectively.

A comparison between range and range straggling is given in figure 3.5 for a secondary beam of ^{132}Sn at a fixed energy of 500 MeV/u. It shows that for stopping of ions in a He gas volume, the absolute range of the ions leads to minor marginal conditions, because the ions can be slowed down beforehand in a solid material. The width of the momentum distribution needs to be thermalized in the stopping volume in order to archive high total efficiencies. Thus the range straggling needs to be small compared to the size of the stopping volume.

In figure 3.6 the mean range of ^{132}Sn ions in He gas is shown as a function of the incident energy (black). The range has been calculated with the software [ATIMA]. The code is based on the Lindhard and Sørenson theory including the shell correction, a Barkas term and the density effect. The projectiles are treated as ions with a realistic mean charge distribution; nuclear size effects are included.

In addition the range straggling is shown for a monoenergetic beam (blue) and for a realistic beam with a Gaussian energy distribution with a sigma of $\sigma = 2.2\%$, which

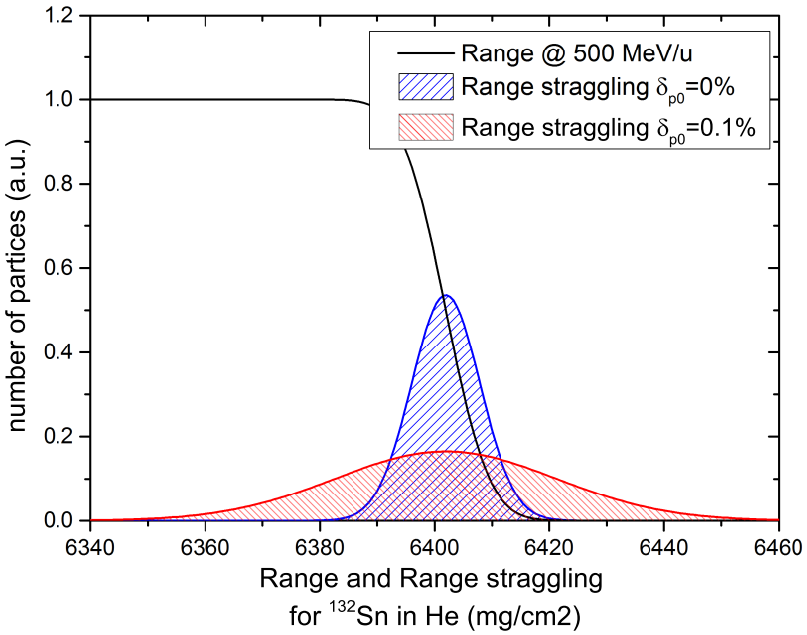

Figure 3.5: Mean range and range straggling of ^{132}Sn in He at 500 MeV/u. The range distribution is shown for a monoenergetic beam and for a beam with momentum spread of ±0.1%.

corresponds to a full momentum spread of 5% (red) [Win13]. For the calculations no spectrometer or ion optics was included, an ion beam was sent onto an infinite amount of He gas and the range and range straggling were reported.

From the figure it is clear that the range straggling of the secondary beam needs to be reduced to the monoenergetic limit in order to stop the ion beam in a stopping volume of reasonable size, corresponding to a stopping volume of 1 or 2 m length. The range straggling can be reduced by slowing down of the fragment beam in a monoenergetic shaped degrader in a dispersive focal plane of a magnetic stage (see section 2.2.3). The required area density for stopping is shown on the right ordinate of the figure in units of a typical stopping cell, with 1 m length and operated at a pressure of 100 mbar helium gas, thus one can get an estimate on the dimension of a stopping cell required for stopping of relativistic ions.

3.5 Manipulation of heavy ions at low kinetic energies

Once the exotic ions are slowed down and thermalized in the He gas volume of a stopping cell, they need to be extracted from this volume into a low-pressure transport beam line and transported to downstream experiments. During this process several environments are passed. In the stopping cell high buffer gas pressures in the order of a few tens to hundreds of mbar are present. The ion motion can be described by mobility theory. In the low energy beam line buffer gas pressures below 10^{-2} mbar are damping the ion motion.

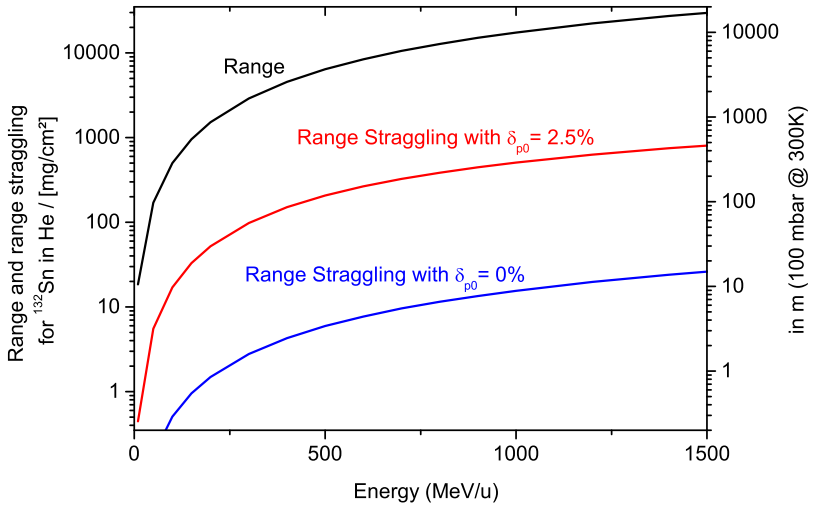

Figure 3.6: Mean range and range straggling of ^{132}Sn in He as a function of energy per nucleon. The range straggling is shown for a monoenergetic beam and for a beam with full momentum acceptance of the Super-FRS of ±2.5% [Win13].

3.5.1 Ion motion in static electric fields at high gas pressures

For the description of the ion motion in the stopping volume, a point-like distribution of ions with mass m and charge q in a buffer gas volume can be considered. The number density (n) of the ions is assumed to be well below the density of the neutral buffer gas atoms. Therefore the ions mainly collide with the neutral atoms. In addition a sufficiently low ion number density allows to ignore Coulomb force interactions. In the case of the absence of a magnetic field the ion motion is determined by collisions of the ions with the buffer gas atoms at a certain pressure p, a possible pressure gradient ∇p and the electric field $\vec{E}$. In this case the fluid equation of motion

$$mn\frac{d\vec{v}}{dt} = mn\left(\frac{\delta\vec{v}}{\delta t} + (\vec{v}\cdot\nabla)\,\vec{v}\right) \tag{3.37}$$

for charged particles can be written as

$$mn\frac{d\vec{v}}{dt} = \pm qn\vec{E} - \nabla p - mnf\vec{v} \tag{3.38}$$

with $\vec{v}$ as the velocity of the charged particles, according to [Moi12, Bat67, Ran12]. The possible change in sign (±) accounts for positive and negative charged ions. The frequency f can be seen as an average collision frequency over particles of all velocities in a Maxwellian distribution. Since the velocity of a particle depends both on time and position, the first line in the above equation describes the motion of the particle in time and space, whereas the second line represents the present physical forces on the particle.

In the case of a slow motion of the fluid compared to the collision frequency a steady state can be assumed. In this case the left side of the equation is zero.

$$0 = \pm qn\vec{E} - \nabla p - mnf\vec{v} \tag{3.39}$$

This yields a solution for the velocity of a particle

$$\vec{v} = \frac{1}{mnf}\left(\pm qn\vec{E} - \nabla p\right) \tag{3.40}$$

In an isothermal conditon this equation can be written as

$$\begin{aligned} \vec{v} &= \frac{1}{mnf}\left(\pm qn\vec{E} - k_B T\nabla n\right) \\ &= \pm\frac{q}{mf}\vec{E} - \frac{k_B T}{mf}\frac{\nabla n}{n} \end{aligned} \tag{3.41}$$

showing that the ion motion is driven by the electric field and the gas density gradient. The coefficients of $\vec{E}$ and $\nabla n/n$ can be summarized as the mobility constant K and the diffusion coefficient D

$$\begin{aligned} K &= \frac{q}{mf} \\ D &= \frac{k_B T}{mf} \end{aligned} \tag{3.42}$$

The known Nerst-Townsend-Einstein relation connects those two coefficients by

$$K = \frac{qD}{k_B T} \tag{3.43}$$

Similar to the electric current a total flux $\vec{j} = n\vec{v}$ of charged particles can be written as

$$\vec{j} = \pm Kn\vec{E} - D\nabla n. \tag{3.44}$$

In the case of zero electric field this results in Fick's law of diffusion [Fic55],

$$\vec{j} = D\nabla n \tag{3.45}$$

describing the expansion of an ion distribution as a result of random collisions between the ion and the buffer gas atoms, with the velocity

$$\vec{v} = D\frac{\nabla n}{n} \tag{3.46}$$

In the one-dimensional case the resulting number density $n(x)$ after time t and distance x of a point like ion distribution, consisting of S ions located at the origin of the coordinate system, can be described by the so called Einstein diffusion equation as

$$n(x) = \frac{S}{\sqrt{4\pi Dt}} \cdot \exp\left(-\frac{x^2}{4Dt}\right). \tag{3.47}$$

By this the mean and the root-mean-square displacement can be calculated as

$$\begin{aligned} |\bar{x}| &= \frac{1}{S}\int_{-\infty}^{+\infty} |x| \cdot n dx \\ &= \frac{2}{S}\int_{0}^{+\infty} x \cdot n dx \\ &= \left(\frac{4Dt}{\pi}\right)^{1/2} \end{aligned} \tag{3.48}$$

and

$$\begin{aligned} \sqrt{\bar{x^2}} &= \left(\frac{1}{S}\int_{-\infty}^{+\infty} x^2 \cdot n dx\right)^{1/2} \\ &= \sqrt{2Dt}. \end{aligned} \tag{3.49}$$

In the three-dimensional space the number density can be written as a function of radius r and time t

$$n(r) = \frac{S}{(4\pi Dt)^{3/2}} \cdot \exp\left(-\frac{r^2}{4Dt}\right). \tag{3.50}$$

resulting in the mean and root-mean-square displacement of the distribution

$$\bar{r} = \left(\frac{16Dt}{\pi}\right)^{1/2} \tag{3.51}$$

and

$$\sqrt{\bar{r^2}} = \sqrt{6Dt}, \tag{3.52}$$

respectively.

In the case of a steady gas, i.e. zero gas flow, the ion motion is dominated by the electric field E applied, resulting in a drift velocity of

$$\vec{v} = K\vec{E}. \tag{3.53}$$

The mobility K is inversely proportional to the number density of the particles. Typically a reduced mobility K_0 is given, normalized to room temperature $T_0 = 273.15$ K and normal pressure $P_0 = 1013.25$ mbar.

$$K = K_0 \frac{T}{273.15\ \mathrm{K}} \frac{1013.25\ \mathrm{mbar}}{P} \tag{3.54}$$

At high pressures the ions, transported by the electric field through the buffer gas, will interact with the buffer gas by long-range interaction due to atoms being polarized and by short-range interactions occurring from collisions between atoms and ions.

The reduced mobility can be derived from the polarization α and the reduced mass $\mu = (m_1 m_2)/(m_1 + m_2)$ of the collision partners; the ion and the buffer gas atom [Mas88].

$$K_0 = \frac{13.853 \cdot 10^{-4} m^2}{\sqrt{\alpha\mu}} \tag{3.55}$$

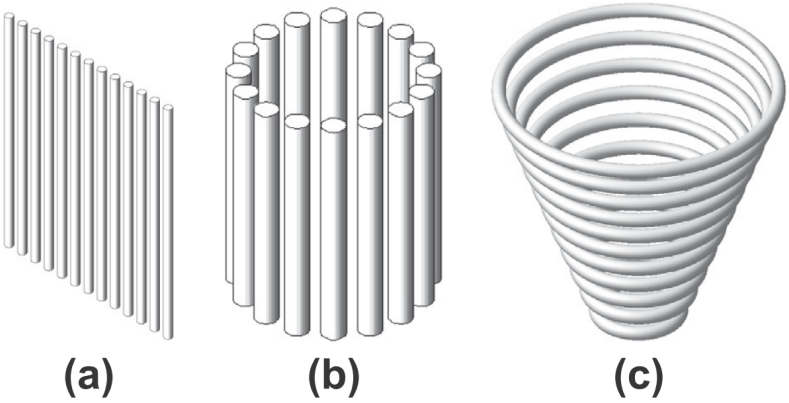

Figure 3.7: Schematic view of three electric curtain devices (a) electric curtain, (b) electric cage, (c) electric funnel developed by [Mas70]. Neighboring electrodes are supplied with a 180° phase shifted RF voltage.

3.5.2 Ion motion at an radio frequency carpet

The ions are transported by a constant electric field to the extraction side of the stopping cell, they reach the area of influence of the effective field E_{eff} produced by an RF structure. This effective field counters the constant electric field and the ions can be stored in an potential minimum in front of the RF electrodes.

The development of the RF carpet technology follows the designs of Masuda and Fujibayashi in the late 1960s [Mas70] and was adopted for transportation and extraction of exotic nuclei from a high pressure stopping volume to a low pressure vacuum beam line [Wad01, Sav01]. Masuda designed three electric curtain devices, an electric curtain, an electric cage and an electric funnel. These are shown in figure 3.7. At an RF carpet not the plain curtain structure is used, but flat concentric ring electrodes. The electrodes are supplied with a radio frequency in the order of a few MHz. Neighboring ring electrodes are connected with a 180° phase shifted RF voltage.

According to Dehmelt and Gerlich [Deh67, Gerl92] the resulting pseudopotential V_p can be calculated as an average over many RF cycles of the actual electric field E_{rf}.

$$V_p(r) = \frac{q}{4m\Omega^2} E_{rf}^2(r) \tag{3.56}$$

with the radio frequency $\Omega = 2\pi f_{rf}$. Following an approach by Wada and Tolmachev [Wad03, Tol97] the resulting field can be described as a quadrupolar field. The RF field is given by

$$E_{rf} = E_0 \cos \Omega t \tag{3.57}$$

where

$$E_0 = \frac{r}{r_0} \cdot E_{max} \qquad \text{for } 0 < r < r_0 \tag{3.58}$$

and

$$E_0 = 0 \qquad \text{for } r > r_0 \tag{3.59}$$

with r_0 as half of the distance between the center of neighboring RF electrodes. From this approach the resulting pseudofield E_P can be derived using

$$E_P = -\nabla V_P \tag{3.60}$$

to

$$E_p = \frac{qV_{rf}^2}{2m\Omega^2 r_0^3} \cdot \left(\frac{r}{r_0}\right) \tag{3.61}$$

with V_{rf} being the voltage of the applied RF.

In order to account for damping of the ion motion by collisions with buffer gas atoms, Tolmachev [Tol97] introduced a velocity relaxation time τ

$$\tau = K\frac{m}{q} \tag{3.62}$$

as the time interval an ion needs in order to lose the velocity gained by the electric field. With this time a damping coefficient γ can be defined,

$$\gamma = \frac{\Omega^2\tau^2}{1+\Omega^2\tau^2} \tag{3.63}$$

allowing the calculation of the effective field in the vicinity of the carpet.

$$\begin{aligned} E_{eff} &= E_p \cdot \gamma \\ &= \frac{qV_{rf}^2}{2m\Omega^2 r_0^3} \cdot \left(\frac{r}{r_0}\right) \cdot \frac{\Omega^2\tau^2}{1+\Omega^2\tau^2} \end{aligned} \tag{3.64}$$

Following Wada [Wad03] E_{eff} can be discussed for two possible cases. In the vacuum case, there are not sufficient buffer gas atoms present and the relaxation time is large compared to the frequency Ω of the RF. Therefore $\Omega^2\tau^2 \gg 1$. In comparison to this, in the high pressure case the relaxation time is short and the ions undergo many collisions within one RF cycle. This results in a small $\Omega^2\tau^2 \ll 1$, which allows a more simple calculation of the effective field E_{eff}, using the expansion $\gamma \sim \Omega^2\,\tau^2 + O\left(\Omega^4\,\tau^4\right)$.

$$\begin{aligned} E_{eff} &= \tau^2 \frac{qV_{rf}^2}{2mr_0^3} \cdot \left(\frac{r}{r_0}\right) \\ &= K^2\frac{m}{q} \cdot \frac{V_{rf}^2}{2r_0^3} \cdot \left(\frac{r}{r_0}\right) \end{aligned} \tag{3.65}$$

For a given RF carpet operating at a fixed temperature and pressure the effective field can be rearranged, using the definition of the mobility K

$$E_{eff} = \frac{1}{2qr_0^3} \cdot \left(\frac{r}{r_0}\right) \cdot \left(K_0 \cdot \frac{P_0}{T_0} \cdot T\right)^2 \cdot m \cdot V_{rf}^2 \cdot \frac{1}{P^2} \tag{3.66}$$

and with the ideal gas law

$$PV = Nk_BT \tag{3.67}$$

the effective field of the RF carpet can be written in terms of the number density $n = N/V$, where V corresponds to the volume of the stopping cell, N to the total number of helium atoms and k_B to the Boltzmann constant,

$$E_{eff} = \frac{1}{2qk_B^2r_0^3} \cdot \left(\frac{r}{r_0}\right) \cdot \left(K_0 \cdot \frac{P_0}{T_0}\right)^2 \cdot m \cdot V_{rf}^2 \cdot \frac{1}{n^2}. \tag{3.68}$$

In the case of a maximal $r = r_0$ this results in the expression

$$E_{eff} = \text{const} \cdot m \cdot \frac{V_{rf}^2}{n^2}. \tag{3.69}$$

It should be noted that the above calculation is only valid for small $\Omega^2\tau^2$.

For state of the are stopping cells using a RF carpet $\Omega^2\tau^2 = 0.022$ results for singly charged ^{219}Rn ions, at a RF carpet frequency of 6 MHz and an ion mobility of 17.5 $\text{cm}^2\text{V}^{-1}\text{s}^{-1}$. Thus $\Omega^2\tau^2$ can be considered small.

The effective field E_{eff} needs to account for the DC electric field of the stopping cell E_{DC}

$$E_{DC} = E_{eff}. \tag{3.70}$$

from equation (3.69) it follows for ^{219}Rn ions

$$E_{DC} = const \cdot \frac{V_{rf}^2}{n^2} \tag{3.71}$$

and in the case of constant DC field

$$n \propto V_{rf} \tag{3.72}$$

results. This relationship allows to test the behavior of the ions at the RF carpet at different number densities n. Experimentally this can be studied by keeping the CSC on a fixed operation pressure and temperature and scanning the required RF voltage of the RF carpet for extraction of ions. With increasing amplitude the effective field gets stronger and from a certain amplitude on it is able to prevent the ions from touching the surface of the RF carpet.

Further Tolmachev [Tol00] mentions a limitation that the ion velocity has to be sufficiently smaller compared to a certain maximal ion velocity given by

$$v_{max} = r_0 \cdot f_{rf} \tag{3.73}$$

which means that the ions should not move more than the distance r_0 between two neighboring electrodes during one RF cycle. This is important for light ions, because the energy transfer in a collision with the buffer gas becomes larger for light ions. The RF carpet can no longer repel the ions from hitting the surface of the electrodes. In order to efficiently transport light ions the RF carpet needs to be operated at higher RF frequencies.

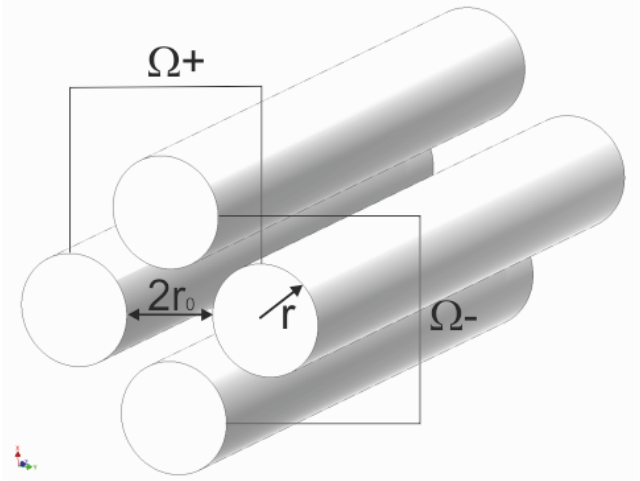

Figure 3.8: Schematic view of an RFQ with cylindrical rods of radius r and distance between the rods of $2r_0$. Opposite electrodes are supplied with same phase RF voltage, neighboring with a 180° phase shifted RF voltage.

3.5.3 Ion motion in radio frequency quadrupoles

A quadrupole consist out of four round, ideally hyperbolic shaped, longitudinal electrodes as shown in figure 3.8. The DC quadrupole lens is a special case as it is focusing along one plane and defocusing along the orthogonal plane. In the case of an RFQ the quadrupole is not operated with a constant electric or magnetic field, but with a radio frequency (RF) voltage. Opposite electrodes are supplied with same phase RF voltage, neighboring with a 180° phase shifted RF voltage. In this scenario the ions are effected by an averaged field, which allows the storage of the ions in the center of the quadrupole.

The quadrupole field of a linear quadrupole can be described according to [Daw76]

$$\Phi = \frac{V(x^2 - y^2)}{r_0^2} \tag{3.74}$$

with the applied voltage between electrodes of opposite phase V and r_0 half of the distance between the electrodes.

Applying a constant electric voltage V_{dc} and a radio frequency voltage V_{rf} the applied voltage can be written as

$$V(t) = V_{dc} + V_{rf}\ f(\Omega t). \tag{3.75}$$

From this Newton's equation of motion can be calculated to

$$\frac{d^2\vec{r}}{dt^2} + \frac{2q}{mr_0^2}\left(V_{dc} + V_{rf}\ f(\Omega t)\right) = 0 \tag{3.76}$$

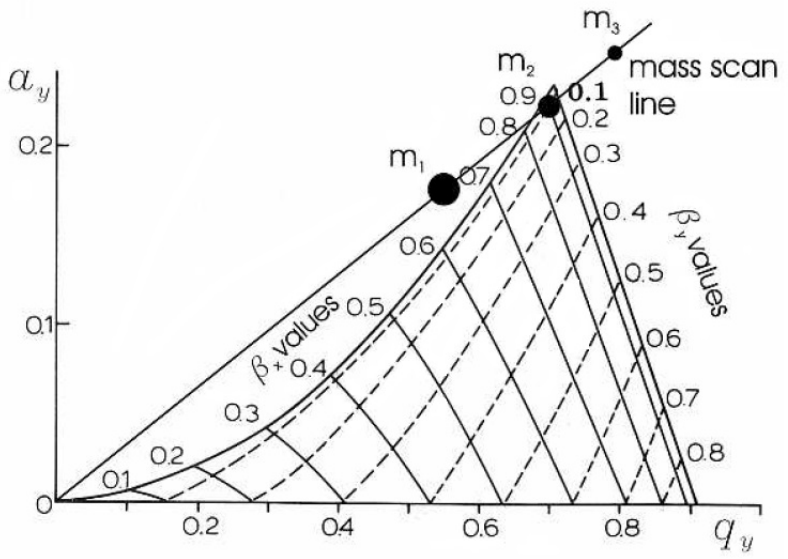

Figure 3.9: First region of stability diagram showing the range of stable ion motion for different combinations of the Mathieu parameters a_x and q_x. Depending on the slope of the mass scan line only the masses in a certain mass window will be transmitted through the RFQ [Daw76].

for an ion with mass m and charge q. Introducing the Mathieu parameters

$$a_x = -a_y = \frac{8qV_{dc}}{m\Omega^2 r_0^2} \tag{3.77}$$

$$q_x = -q_y = \frac{4qV_{rf}}{m\Omega^2 r_0^2} \tag{3.78}$$

results in the so called Mathieu equations, which describes the ion motion in the RFQ. The motion is only stable for certain combinations of a_x and q_x, defining the stability diagram of the ion motion in a RFQ. In figure 3.9 the first region of the stability diagram is shown. Only masses, which are inside the region of stability, will pass through the RFQ, other masses will not be transported through the RFQ. For given parameters of operation of an RFQ, fixed r_0, V_{dc}, V_{rf} and Ω, the Mathieu parameters a_x and q_x only depend on the mass m and the charge q of the ion. This means that all masses lie on a line with a slope $a_x/q_x = 2V_{dc}/V_{rf}$. This line is called the mass-scan-line. Depending on the slope the line may cross the stability diagram at different values for a_x.

Operating an RFQ with RF voltage only, $V_{dc} = 0$, results in $a_x = 0$. In this case stable ion motion is possible up to $q_x = 0.908$, corresponding to the low-mass-cut-off of the RFQ. For $a_x \sim 0.237$ and $q_x \sim 0.706$ the top of the stability diagram is crossed, only masses of a narrow mass window will have stable trajectories. In figure 3.9 only ions of mass $m = m_2$ will pass through the RFQ, while lighter and heavier mass ions will not. Therefore the RFQ works in the mass-filtering mode [Pau53].

Similar to the description of the ion motion at the RF carpet an effective or pseudo-

potential can be defined, by [Deh67] as

$$V_P(r) = \frac{qV_{rf}}{4}\left(\frac{r}{r_0}\right)^2 . \tag{3.79}$$

Behind gas-filled stopping cells high residual gas pressures up to 10^{-2} mbar are achieved under best conditions in a first differential pumping section. At these pressures several effects take place. At pressures above 10^{-1} mbar the vacuum pseudo-potential is reduced by buffer gas collisions [Tol97]. Whereas at pressures between 10^{-3} to 10^{-2} mbar the ions are cooled by collisions with the residual gas atoms. Thereby they lose kinetic energy and the phase space volume of an ion beam can efficiently be reduced.

The technique of buffer gas cooling is very useful because most high precision experiments require ion beams with small phase space and small energy spread. In addition, through collisions the ions are slowed down up to the point where they may get stuck in the RFQ. In order to achieve reasonable transport velocities, especially for low ion currents at high residual gas pressures, where the ions are not pushed through the RFQ by space charge, an additional axial drag field E_d is required.

The drift or drag velocity of the ions through the RFQ can be described by the mobility K (see eq. (3.54)), which is related to the cooling time constant τ of the ions in the RFQ, [Tol97]. If the pressure becomes too high and the mobility K too small, the ion motion can no longer be described well by the pseudo-potential model. The description is only valid if the cooling time is larger compared to the period of the applied radio frequency.

The kinetic energy E_{kin} of ions with mass m, dragged through the RFQ in direction of the electric field E_d can be calculated as

$$E_{kin} = \frac{1}{2}mv^2 = \frac{m}{2}\left(E_d K\right)^2 . \tag{3.80}$$

For efficient storing of ions the kinetic energy should not become too large. A good compromise between fast transport and kinetic energy is about 1 eV, corresponding to a drift velocity of $\sim$ 1 m/(ms) [Dic10].

To create suitable drag fields several methods have been developed

- Segmented RFQ rods
  Using segmented RFQ rods is the most widely used technique [Jav97, Don97]. In this approach the RFQ rods are cut into small pieces, each piece can than be supplied with an additional DC potential, forming a gradient along the axis of the RFQ. This technique is especially useful for short and medium length RFQs, as for long RFQ rods the amount of segments and therefore the amount of connections and vacuum feedthroughs is increased. However using segments with reasonable length does not provide a homogenous drag field along the RFQ. A compromise between length of the segment and number of segments needs to be made.

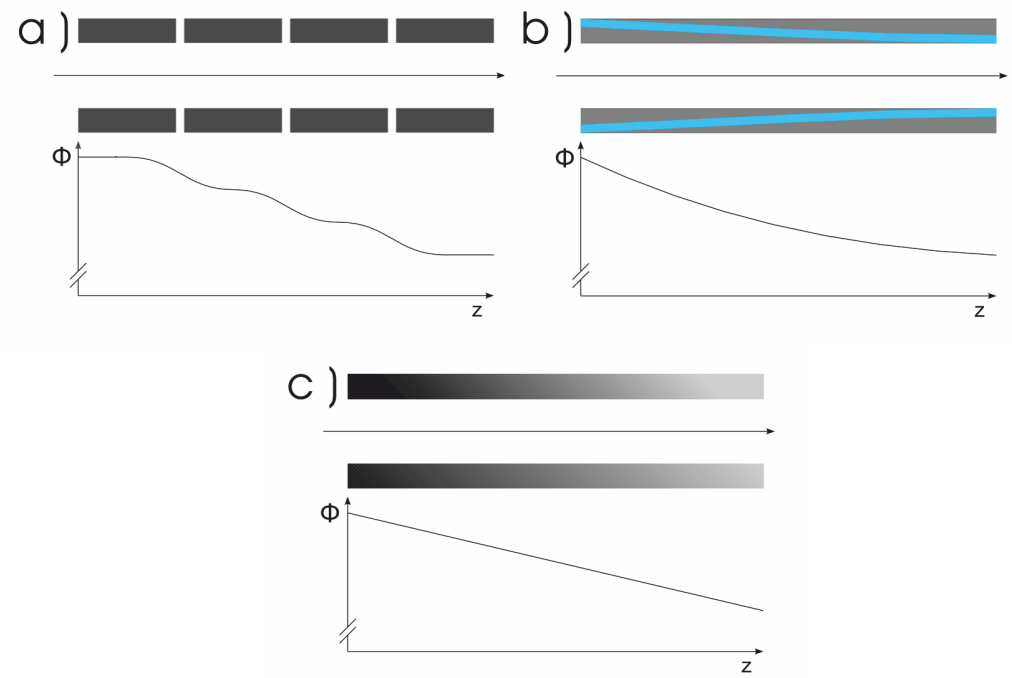

Figure 3.10: Schematic view of potential on the axis of an RFQ for different methods to create suitable drag fields [Dic10]. a) segmented RFQ rods, b) LINAC RFQ rods and c) an RFQ based on resistive rods.

- LINAC RFQ rods
  For longer RFQs it is advisable to use the so called LINAC RFQ rods [Lob00]. Here additional DC electrodes are placed between the rods of the RFQ. These electrodes are tilted about 1% along the RFQ and their effect on the DC potential on the axis of the RFQ is reduced. Therefore a potential gradient on axis is introduced. A disadvantage of this technique is that in order to achieve a well defined potential tight tolerances need to be kept.

- Resistive RFQ rods
  A third approach is to use RFQ rods made out of resistive materials and applying a DC gradient along the RFQ rods themselfes. Compared to the two former methods the technique using resistive materials for the RFQ rods [Tak07], is simple and robust. The RFQ rods are produced out of plastics containing carbon. Resistances of 100 Ω to 1 kΩ can be reached for a RFQ with a length of 30 cm, allowing a sufficient axial DC gradient along the RFQ. In addition these materials can be used to form curved ion guides or switchyards [Sim08, Dic10, Pla15, Jes15].

4 Conceptual design of a cryogenic stopping cell for the FRS/Super-FRS

Gas-filled stopping cells have successfully been used for the thermalization of radioactive ion beams produced by fusion evaporation and fragmentation [Sav01, Wad03, Sav03, Wei04, Neu06]. The feasibility of thermalizing exotic nuclei produced at relativistic energies, by fragmentation of a ^{58}Ni primary beam at 300 MeV/u, has also been shown in a first experiment at the FRS at GSI in 2005 [Sav03, Pet08]. The main limitations during this campaign arose from the low stopping efficiency of (5.0±1.1) % resulting in a total efficiency of (1.8±0.3) %. In addition hydro carbons were present in the stopping cell, thus no clean ion beam could be extracted from the stopping cell and mass measurements were not possible. A typical mass spectra of ions extracted from the stooping cell is shown in figure 4.1. At almost each mass line several molecules were measured. Efficient stopping of secondary beams produced at 1000 MeV/u or above is even more challenging, because of the larger range straggling.

This first proof-of-principle experiment triggered the development of a second-generation stopping cell for the FRS, which acts as a prototype stopping cell for the future low-energy branch [Sche03] of the Super-FRS [Gei03]. Based on the research performed by [Den06] the prototype stopping cell was designed as a cryogenic stopping cell [Ran11, Ran12], thus contaminants in the stopping gas can efficiently be removed by cryo-sorption. For experiments a beam of exotic nuclei is produced by fragmentation or fission, separated in flight and its momentum spread is reduced by range bunching [Gei89, Wei00A, Sche03]. This monoenergetic radioactive beam of high energy enters the volume of the stopping cell through several thin beam windows. The exotic nuclei loose energy and finally thermalize in the buffer gas volume of the stopping cell. As a stopping gas high purity helium gas is used. Once the ions of interest are stopped in the stopping gas a homogenous longitudinal electric field pulls them to the extraction side of the stopping cell. In order to prevent the ions from hitting the chamber walls a RF carpet, positioned at the extraction side of the stopping cell, produces a pseudo potential wall. A superimposed radial DC field transports the ions along the RF carpet towards an extraction nozzle. When reaching the vicinity of the nozzle, the gas flow dominates the ion transport and flushes the ions from the high pressure stopping region into a low pressure beam line. In order to reach a high pressure gradient between the stopping volume and the low pressure beam line an extraction nozzle of $\oslash \sim 0.6$ mm is used. For efficient ion confinement in the first differential pumping section an extraction RFQ is used.

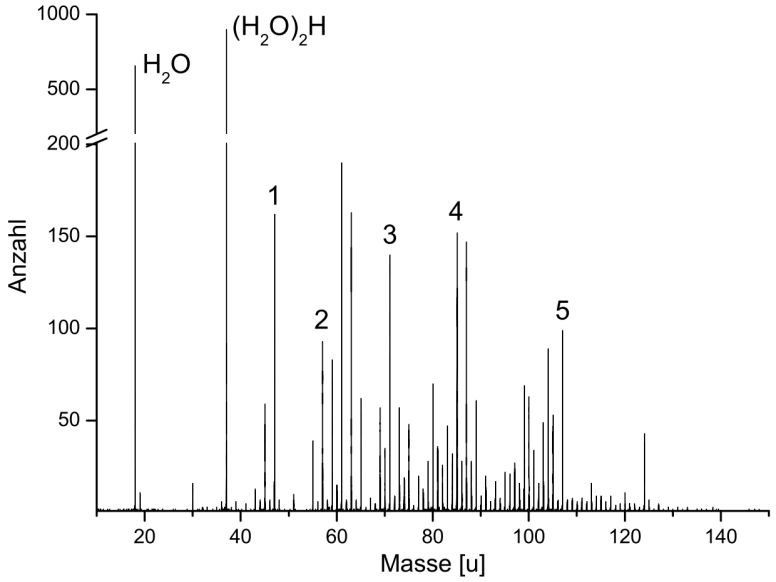

Figure 4.1: Typical mass spectra of the ion composition extracted from the first generation room temperature FRS Ion Catcher stopping cell. The labeled peaks could be assigned to different hydro-carbon molecules [Pet08].

The key performance parameters of stopping cells for exotic nuclei are their efficiency and extraction time. The total efficiency of the device can be split up in (i) the stopping efficiency and (ii) the extraction and survival efficiency. The stopping efficiency represents the fraction of the incoming high energy beam that can be stopped inside the stopping cell. The survival and extraction efficiency describes the fraction of the stopped ions which get extracted from the stopping cells as ions without adducts.

In order to reach short extraction times on the order of a few ms, high longitudinal DC fields are required. DC fields between 10 and 100 V/cm are sufficient to extract exotic nuclei in less than 10 ms from a one meter stopping volume operated at 100 mbar and 100 K [Ran14].

In order to reach the highest stopping efficiencies a stopping cell needs to operate at high area densities. As described in section 3.5.2 the pseudopotential of an RF structure is inversely proportional to the square of the number density in the buffer gas and inversely to the structure size to the power of three. Therefore small structure sizes have to be used in order to reach sufficient strong repelling fields. For a stopping cell operating at the highest area density RF Carpets based on printed circuit boards (PCB) with small structure sizes, compared to RF funnels made from stainless steel electrodes, can be constructed and allow efficient ion transport in a stopping cell.

The survival and extraction efficiency is limited by the cleanliness of the stopping gas. In an ideal stopping cell only helium gas is present. The first ionization potential of helium is higher than the second ionization potential of almost all elements. Thus in collisions with helium atoms the ions of interest can reach a 2^+ or 3^+ charge state. However, in most ultra pure systems still some impurities are present with lower

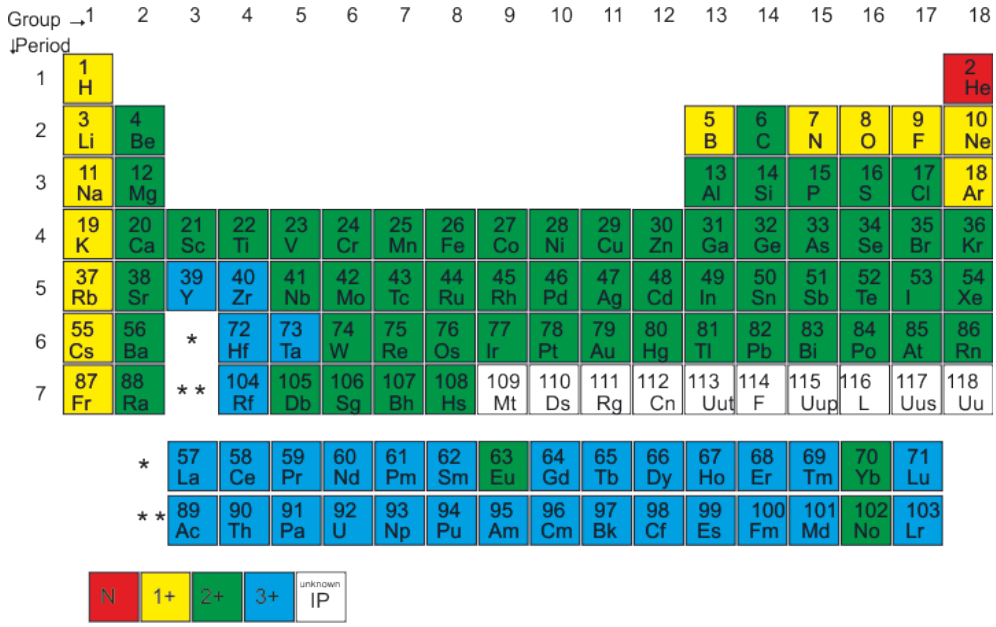

Figure 4.2: Estimated charge states of elements extracted from the CSC for a pure helium-dominated stopping cell. The charge state is derived from the first, second and third ionization potential of each element in comparison the the ionization potential of He of 24.6 eV. Ionization data was taken from the NIST database [Kra14].

ionization energies. These can perform charge exchange reactions with the 2^+ or 3^+ ions of interest. Therefore many ions end up in a 1^+ charge state or are neutralized. Once exotic ions are neutralized they can no longer be transported by electric fields and are lost for experiments. Figure 4.2 gives an overview of the charge state, in which ions of a certain element are excepted to be extracted from a stopping cell if only helium atoms are present in the stopping volume. It shows that $\sim$ 70% of all elements will be extracted in a 2^+ charge state and about 15% as 1^+ and 3^+ ions. The situation changes drastically if hydrocarbons, which may have much lower ionization potential, are present in the stopping cell, many elements will be neutralized during their extraction from the stopping cell. Therefore ultra pure stopping gases are needed for an efficient operation of a stopping cell.

To investigative the required cleanliness of the stopping gas in a more quantitative way, the number of collisions N_0 of an ion of interest was determined. Assuming that each ion of interest is neutralized once it collides with a contaminant atom, the required cleanliness can be calculated as the total probability of a collision with a contaminant during all collisions

$$\rho_{\text{contaminant}} = 1 - \epsilon^{1/N_0}, \tag{4.1}$$

with the concentration of a certain contaminant species $\rho_{\text{contaminant}}$ and the total probability ϵ for the extraction of the ion of interest from the stopping volume. This approach assumes chemical reaction rates of 100% and therefore results in a lower limit requirement. The collision rate of the ion of interest was determined from simulations using the hard sphere and the Langevin collision cross section in the ion

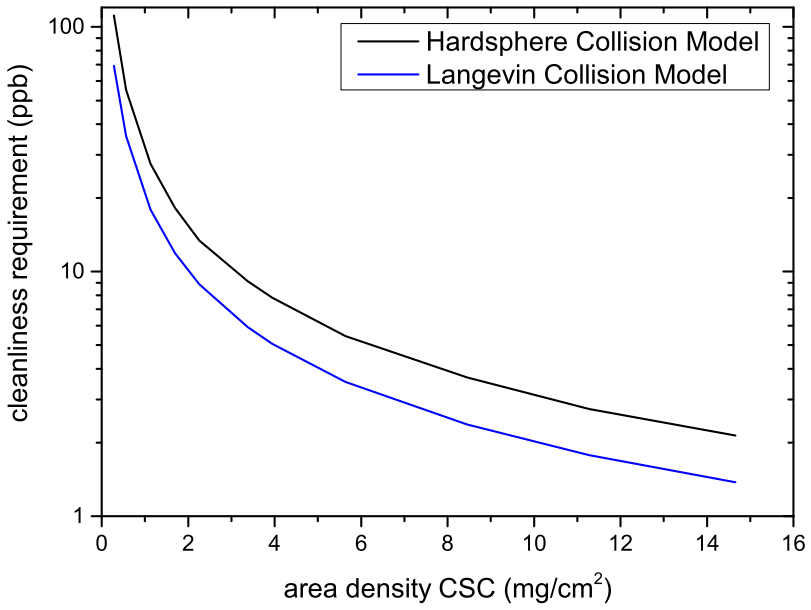

Figure 4.3: Calculation of the required cleanliness for extraction of ions from a stopping cell for different areal densities. The requirement is estimated from the number of collisions ions typically perform until they get extracted from the stopping volume. The collision rate was determined using ITSIM and the Langevin and hard sphere collision cross section models.

trajectory simulation program ITSIM [Pla01]. A hard sphere cross section of 50 $Å^2$ was assumed.

In figure 4.3 the concentration of contaminant, which allows that less than 68.3 % ($\pm$ one σ) of the ions collide not even once with a contaminant, is plotted as a function of the area density of the stopping cell. If the stopping cell is operated at higher area densities the ion of interest performs more collisions until its extraction from the stopping volume. Therefore at higher area densities a cleaner stopping gas is required. For a stopping cell with about 3 mg/cm^2, corresponding to a cell with length 1 m and 180 mbar at room temperature, and an extraction time of 25 ms a He gas purity of about 5 to 10 ppb is required.

Reaching such a buffer gas cleanliness is a challenge for all stopping cells, because only during an initial cleaning period the volume can be pumped. For operation the stopping cell with helium stopping gas, the vacuum pumps need to be separated from the chamber, no additional pumping can be applied to the stopping volume and contaminants, still evaporating from the walls of the chamber, are no longer removed. Different solutions are used to reach the required cleanliness goals.

The strict usage of UHV materials, such as stainless steel and ceramics, is one approach. In this case the stopping cell is baked at high temperatures before operation and contaminates are removed from the stopping volume before operation. It has the disadvantage of complex constructions and which sometimes end up being fragile due to ceramic insulators. In addition electronic components can not be placed inside

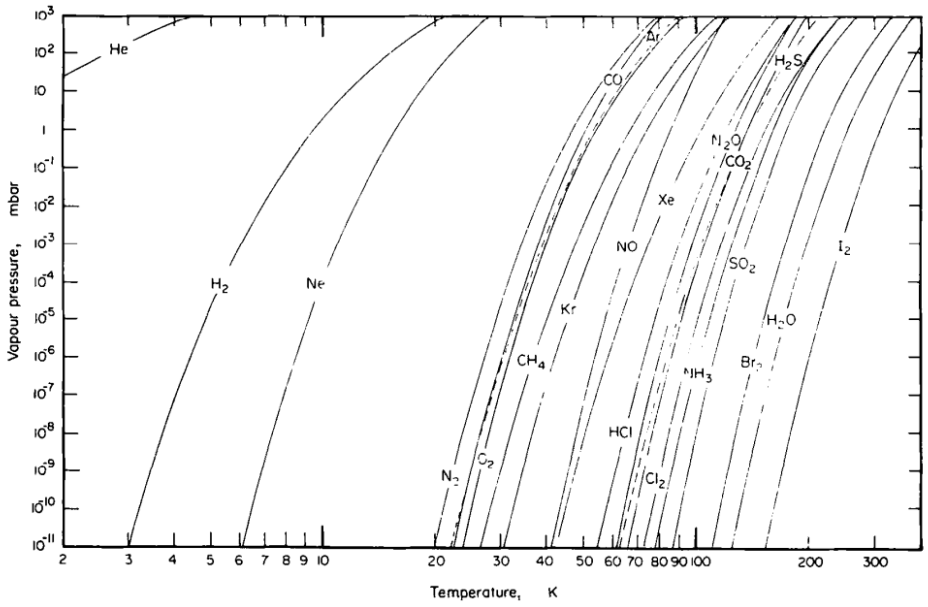

Figure 4.4: Vapor pressure of different gases for different temperatures. The graph shows the working principal of cryo pumps [Ben80].

the stopping cell, because these are typically not UHV suitable. If they are placed inside the stopping cell, they limit the maximal temperature for baking of the vacuum chamber and therefore the cell may not be baked at high temperatures up to 500 to 600 K, which are required for room temperature UHV systems.

A different approach is to clean the buffer gas by cryo-sorption. In this case the stopping cell is cooled down to low temperatures and impurities 'freeze' out on the walls of the stopping cell chamber. Such a cryogenic stopping cell (CSC) allows a wide choice of materials and can be constructed more easily and at the same time can be operated more reliability. Reaching ppb impurity levels by cooling down is more reliable than reaching ultra pure conditions by baking procedures required for room temperature systems.

In figure 4.4 the vapor pressure of different gases is shown as a function of temperature. When cooling down the stopping cell the maximal vapor pressure of impurities is reduced, e.g. for CO_2 at 100 K, a vapor pressure of 10^{-3} mbar can be present, reducing to below 10^{-11} mbar at 65 K. The figure shows this effect for different gases. It can be seen that at about 70 K already many impurities are reduced to the 10^{-9} mbar level. This shows that for the cryogenic stopping cell under operation conditions cryo-sorption takes place and the helium stopping gas is purified constantly. However, the pumping speed of the cold surface is reduced if a first monolayer is absorbed. This means that the residual gas pressure inside the stopping volume before starting of the cooling needs to be sufficiently low, in order to not reach the one monolayer limit.

In addition the contaminants added to the stopping cell by the helium stopping gas need to be considered and additional gas purification before feeding the helium gas to the stopping volume is required.

5 Experimental setup – The FRS Ion Catcher

In the following chapter the experimental setup of the FRS Ion Catcher (see figure 5.1) will be described. The FRS Ion Catcher experiment at GSI consists of four main parts, the fragment separator FRS including a monoenergetic degrader system, the cryogenic gas-filled stopping cell (CSC), an RFQ-based ion beam transport and diagnostics unit (DU) and a multiple-reflection time-of-flight mass spectrometer (MR-TOF-MS) [Pla13a]. For experiments the stopping cell, its diagnostics unit and the MR-TOF-MS are installed at the S4 final focus area of the fragment separator, because so far the stopping cell is not a permanent experiment at the FRS at GSI. The setting-up time is about a few days only, because the individual subsystems of the FRS Ion catcher are designed modular and electronics equipment is directly mounted within their holding frames. Three commissioning experiments were performed at the FRS with the CSC in 2011, 2012 and 2014.

5.1 The fragment separator – FRS

At the projectile fragment separator FRS exotic nuclei can be produced at relativistic energies by projectile fragmentation or fission in-flight on a thin Be target at the entrance of the fragment separator and separated in-flight.

At the future Super-FRS a pre-separator and a main separator will be used for the separation of the ions of interest from unwanted contaminants. In the future a dedicated energy buncher will be placed at the Low-Energy-Branch and allow to perform the range compression [Sche03].

The current FRS has no dedicated energy buncher section. For experiments with the cryogenic stopping cell, the FRS has to be operated in special mode, in such a way, that both separation and range compression are performed using the four dipole stages of the FRS. The variable degrader system at the central focal plane of the FRS can be tuned to act as an achromatic degrader for optimum separation performance, as a monoenergetic degrader for optimum range bunching, or as a degrader that provides both separation and range bunching [Gei89]. To achieve this a variable degrader system consists of two counter-rotating wedge-shaped aluminum discs, two aluminum wedges and uniform degrader aluminum slabs [Gei92]. The operation mode providing

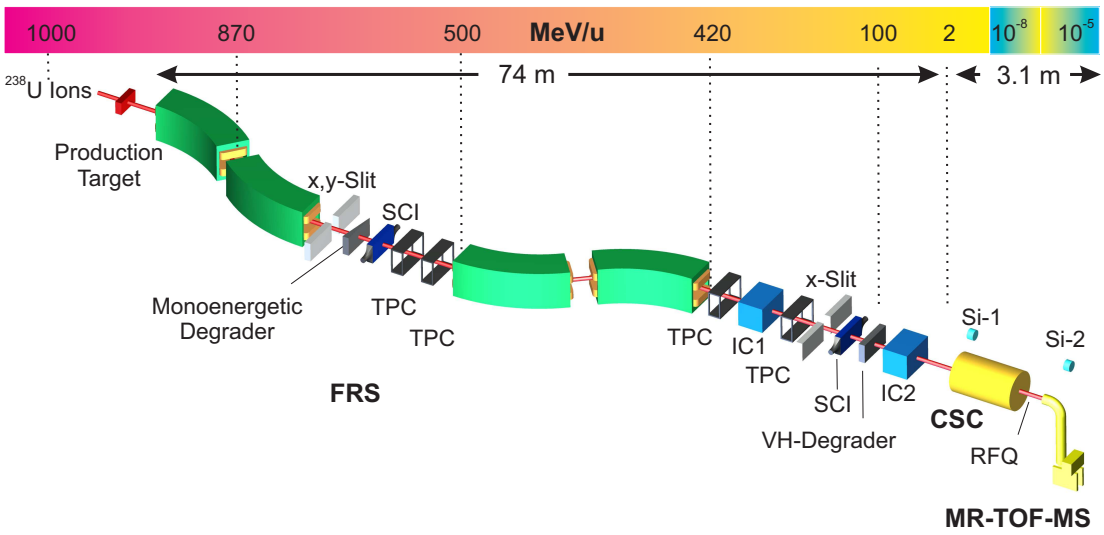

Figure 5.1: Experimental setup of the FRS-Ion-Catcher consisting of the fragment separator FRS with the degrader systems at the central and final focal planes, the detectors for the particle identification in-flight, the cryogenic stopping cell (CSC), the RFQ inside the diagnostics unit and the MR-TOF-MS [Pur13].

both separation and range bunching was chosen for the experiments at GSI. This operation mode does not reproduce the maximum performance of a dedicated range bunching stage [Gei89], but allows for proof of principle experiments using the prototype cryogenic stopping cell at the current FRS. An additional homogenous variable degrader (VH-degrader) at the final focal plane in front of the stopping cell is used to adjust the range of the ions such that they come to rest in the stopping volume of the CSC. A set of a scintillator detectors (SCI) and two time-projection chambers (TPCs) [Jan11] at the middle and final focal plane and two multiple sampling ionization chambers MUSICs (IC) [Pfu94] at the final focal plane are used to provide ion-by-ion identification by measurement of the time-of-flight, the magnetic rigidity, and the energy loss [Pur13].

In addition during two experiments a new detector has been used for identification of ions by their alpha decay energies and life times (alpha tagger) [Far11]. The detector consists of a double-sided silicon strip detector in a separated vacuum chamber that can be moved in and out of the beam directly in front of the stopping cell. In figure 5.1 the alpha tagger is referred to as Si-1.

5.2 The cryogenic stopping cell – CSC

In order to efficiently stop range-bunched beams produced at the Super-FRS a stopping gas with an areal density from about 2 to 20 mg/cm^2 is required [Pur13]. This requirement depends on the reaction type and production mechanism, primary beam energy, charge state, etc. An area 10 cm high and 25 cm wide has to be covered to

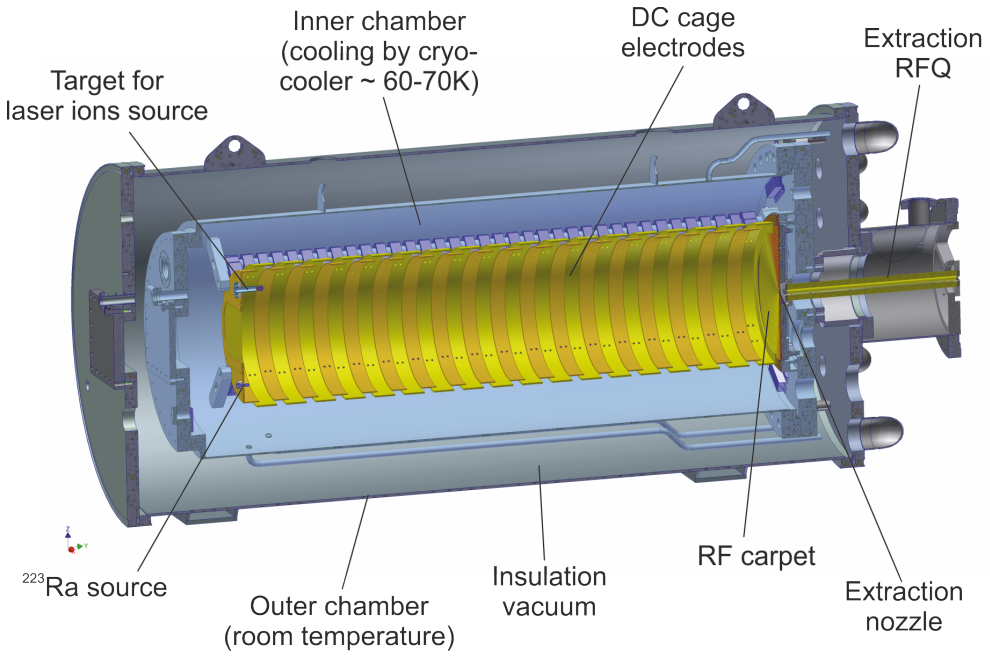

Figure 5.2: Technical drawing of the CSC. Showing the outer chamber, providing thermal insulation, and the inner chamber (light blue) of the stopping cell. Ion optical elements are shown in yellow (DC Cage, RF Carpet and Extraction RFQ).

receive the beams delivered at the low energy branch. Following these requirements, the prototype cryogenic stopping cell with a stopping volume with a length of 104.5 cm and a diameter 25 cm has been designed and built [Scha10, Ran11, Ran14]. It uses high purity helium 6.0 as stopping gas. An outer vacuum chamber with a length of 145 cm and an inner diameter of 66 cm provides the insulation vacuum for the inner cryogenic chamber. The insulation vacuum chamber is pumped by a turbomolecular pump to pressures $< 10^{-7}$ mbar. Relativistic ions enter the stopping cell through two stainless steel windows with a thickness of 100 μm each. A DC electric field created by a cage of DC electrodes through the length of the stopping cell drags the ions towards the exit side of the stopping cell. There, an PCB based RF carpet with a ring electrode density of 4 electrodes/mm (electrodes with a width of 100 μm and a height of 30 μm, spacing of 150 μm) creates a repulsive RF field. A superimposed DC field guides the ions radially towards the exit region in the center of the RF carpet. Once the ions reach the exit region, the gas flow drags them out off the stopping cell through an extraction nozzle of $\varnothing \sim 0.6$ mm into the extraction RFQ.

After the off-line commissioning of the device and first test measurements by [Ran11, Ran12] in the framework of this thesis the cryogenic stopping cell was revised in order to enhance its performance and reliability. Figure 5.2 shows a technical drawing of the current CSC used during the FRS Ion Catcher experiments. The main changes are listed blow:

- New DC cage
  A new DC cage with better shielding of the support rods has been constructed.

The entrance side of the DC cage is formed by a planar stainless steel window with a thickness of 100 μm, similar to the beam windows of the vacuum chambers. The new construction is based on thirty-three overlapping DC electrodes with an alternating inner diameter of 25 cm and 26.7 cm, which are connected by resistors of 3.3 MΩ. The DC electrodes have a distance of 7 cm to the inner chamber walls, held at ground potential. This defines the shortest distance between high voltage and ground. A voltage of up to 3 kV can be applied to the entrance side of the DC cage at a stopping gas pressure of 100 mbar and a temperature of 100 K, corresponding to an area density of 5 mg/cm^2. Thus a DC field of $\sim$ 30 V/cm enables fast extraction of the ions from the CSC [Pur13]. The first DC ring and the beam window are biased separately and are not part of the resistor chain, which allows to measure the electron current on the beam window, produced by the ionization of the beam particles. By a measurement of the electron current during an experiment, the amount of ionization caused by the beam can be monitored. This allows for adjusting of the range and the stopping position of the ion of interest independent of downwards detectors.

- Improved RF carpet design
  The design of the RF carpet was improved with the knowledge gained from extensive ion trajectories simulations using ITSIM [Pla01]. The operation frequency of the RF carpet was optimized for achieving a minimum required RF power at an optimum ion transmission efficiency; it amounts to 6.5 MHz for ions with mass 200 u. In simulations it was observed that the field penetration from the backside of the RF carpet to the front side, along which the ions are transported, is not negligible. In order to reduce this effect and shield the ion path from the electric fields produced by the electronic components on the backside of the RF carpet, the third generation RF carpet of the cryogenic stopping cell is equipped with additional layers of electrodes, resulting in a RF carpet with a total thickness of 1315 μm [Aje14].

  An overview of the layout of the third generation RF carpet is shown in addition to the earlier generations of the RF carpet used during the 2011 (first generation, [Ran14]) and 2012 (second generation) FRS Ion Catcher experiments in figure 5.3. The third generation RF carpet is shown in more detail in figure 5.4. A first inner layer, directly behind the RF electrodes, can be set to a defined DC voltage. In this way the field penetration through the RF electrodes can be tuned. The first inner layer is segmented into ten segments, which are connected by a resistor chain. This allows to operate the carpet at almost any offset potential, because the field penetration through the RF electrodes can be kept independent of the offset potential of the RF carpet. In addition the potential at the outside and the center of the first inner layer can be tuned independently, allowing for a constant field penetration at the outside and at the center of the RF carpet. Simulations as well as test measurements show that by this RF amplitudes for transportation of ions can be reduced by more than a factor of two (see chapter 6.5.2). Additionally this prevents the formation of pseudopotential pockets at the RF carpet. Ions are not stored radially at the RF carpet and can be transported faster along the surface of the RF carpet.

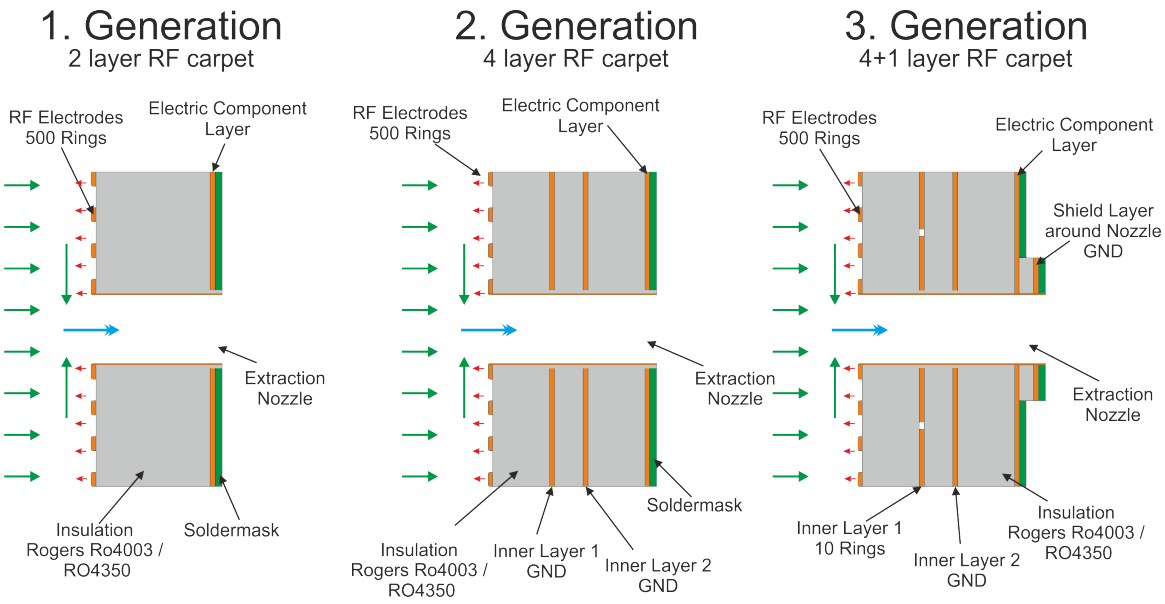

Figure 5.3: Schematic drawing of a cut around the extraction nozzle region trough the RF carpet. The three generations of the RF carpet are shown used at the cryogenic stopping cell during the 2011 (first gen.), 2012 (second gen.) and 2014 (third gen.) FRS Ion Catcher experiments. The forces acting on the ions resulting from the the DC field (green), the effective RF field (red) and the gas flow (blue) are indicated.

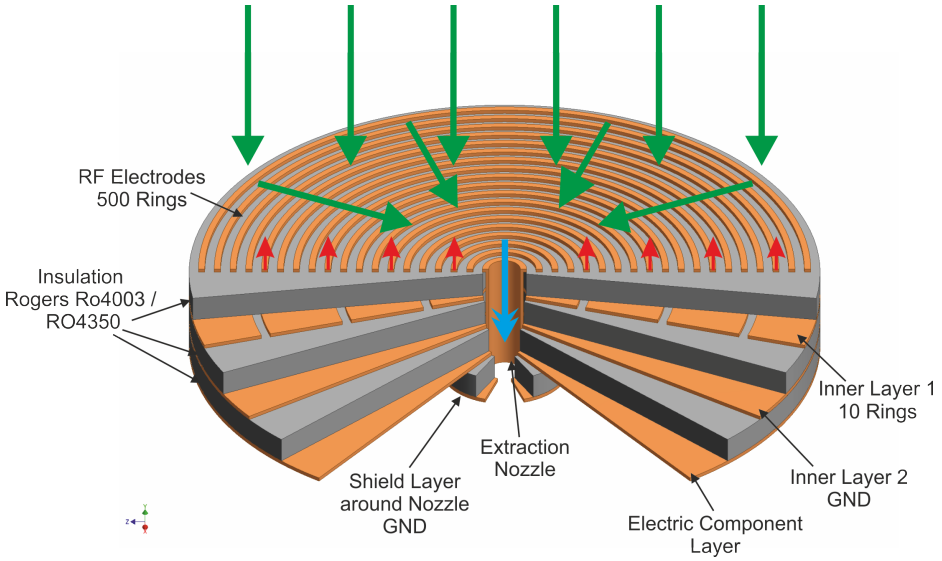

Figure 5.4: Schematic drawing showing the extraction region of the third generation RF carpet from the top view used in the 2014 FRS Ion Catcher experiment. The forces acting on the ions resulting from the the DC field (green), the effective RF field (red) and the gas flow (blue) are indicated.

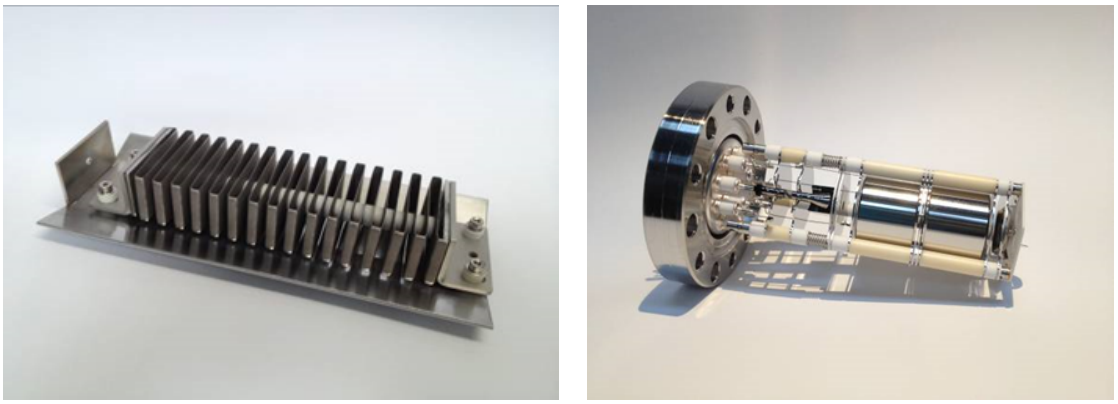

Figure 5.5: Picture of the getter pump and the RGA before mounting inside the inner chamber of the CSC.

Being able to choose the potential of the RF carpet and the extraction nozzle is an important advantage for tuning of the downstream beam line. A second inner layer, placed behind the first inner layer, reduces the electric fields of the electronic components placed on the backside further. No electronics is placed close to the extraction nozzle on the backside in order to reduce the influence on the trajectories of the extracted ions between the extraction nozzle and the beginning of the extraction RFQ. In addition a fifth layer shields the ion pathway behind the RF carpet by reducing the field generated by the supply connections of the most inner RF rings on the back side of the RF carpet.

For the 2014 experiments a new RF carpet support structure was implemented. With this the carpet becomes more stable and the alignment between the extraction nozzle and the extraction RFQ was improved. The extraction RFQ is positioned at a distance of 5 mm from the nozzle. The impedance matching of the RF carpet was adjusted for the operation at low temperatures and the RF carpet was equipped with circuits for direct measurement of the RF amplitude during operation.

- Improved cleanliness of the stopping cell
  The cleanliness of the cryogenic stopping cell was improved by several modifications. The pumping speed for pumping of the stopping volume was improved by about a factor five by coupling a turbomolecular pump as close as possible to the chamber. Thus the base residual gas pressure of the stopping cell before cooling down could be lowered by more than one order of magnitude. In addition in order to enable the pumping of contaminants even during operation of the stopping cell, a getter pump was built using a getter material (SAES WP750 with ST 707 coating), see left hand side of figure 5.5 .

  In order to reach the highest cleanliness the cryogenic stopping cell was modified to allow for baking at intermediate temperatures ($\sim$ 420 K), by using copper sealings and high temperature plastics as electric insulators (PEEK, PPS, PTFE). The inner chamber was equipped with a special PTFE based heating

band, which is permanently warped around the inner chamber and stays in the insulation vacuum. Thus the stopping cell can be baked at up to 420 K before cool down to cryogenic temperatures. In addition the heating band providing about 1 kW of power allows a fast warming up of the stopping cell for maintenance. Further in order to reach lower operation temperatures, the amount of heat radiation was reduced by wrapping the inner chamber in 30 layers of super-insulation (Marke-etc). The resulting enhanced extraction and survival efficiency will be discussed in chapter 6.3.

- Improved cleanliness of the stopping gas
  The main contribution of contaminants in the cryogenic stopping cell arise from the contaminants put into the system by the helium stopping gas (see discussion in chapter 6.3). In order to enhance the cleanliness of the stopping gas before feeding it into the inner stopping chamber, a MicroTorr helium purification getter was added to the system. Furthermore the helium stopping gas bypasses a cold trap inside the cooling system. This reaches temperatures as low as 55 K, purifying the helium gas further.

- Monitoring system of the cleanliness
  The inner UHV chamber of the CSC is permanently equipped with a residual gas analyzer. The custom remodeled RGA (Grandville-Phillips VQM 835) allows to measure the composition of the residual gas atoms. The main advantage of this device is that it can operate during room temperature as well as at cryogenic temperatures, because the control electronics was separated from the inner vacuum chamber. Therefore it can be used to check the cleanliness of the cryogenic stopping cell before operation and filling it with helium gas. At the right hand side of figure 5.5 a picture of the RGA is shown before mounting.

- Improved pumping scheme
  The differential pumping was improved by doubling the pumping speed of the turbomolecular pumps in the diagnostics unit between 2012 and 2014. In addition new rough pumps were implemented to backup the turbomolecular pumps, which allows for a significant lower fore vacuum pressure. An overview of the differential pumping is given in figure 5.6.

  In order to prevent damage of the RF carpet during venting of the system, venting the extraction region before venting the stopping volume, results in an opposite force on the RF carpet, safety valves have been installed. A safety line connects the extraction region and the stopping volume with an one-way valve. This prevents from building up a opposite pressure gradient and protects the RF carpet. Furthermore all vacuum pumps have been equipped with emergency valves, which close in case of a power failure and preserve the vacuum and therefore the cleanliness of the system.

The CSC is equipped with cooling channels around the inner UHV chamber. Through these channels a coolant can be pumped. In 2011 the stopping cell was cooled by pouring liquid nitrogen through the cooling channels of the inner chamber. Since 2012

a cryocooler-based cooling system has been installed, which pumps high pressure (up to 10 bar) cold helium gas through the cooling channels of the inner chamber, which is illustrated in figure 5.6 [Ran14]. The helium gas is cooled by a cold head inside the cooling system and pumped to the CSC. This has the advantage that temperatures as low as 50 K on the walls of the inner chamber can be reached and that continuous operation of the system with minimum user interaction is possible. In addition the cooling system is equipped with an LN_2 pre-cooler, see figure 5.6. With this the coolant helium gas can be pre-cooled before reaching the cold head increasing the cooling power of the system. The pre-cooler acts additionally as a fall back solution if the cold head might fail during an experiment. Using only the LN_2 pre-cooler for cooling of the CSC allows temperatures down to 120 K.

The two-stage approach, separating cold head and stopping cell, allows a more flexible operation and gives better access to both systems [Ran14]. In addition the cooling system provides pre-cooled helium stopping gas for the CSC in order to reduce the heat input. The helium gas passes through a cold trap and thereby the cleanliness of the helium stopping gas is improved.

The CSC is equipped with a ^{223}Ra recoil ion source with a half life of 11.4 days. The first daughter of the ^{223}Ra can be extracted from the CSC. With different detectors (surface barrier Si, Channeltron, MR-TOF-MS) the extraction and transport efficiency can be determined. The source strength of each ^{223}Ra source used in the CSC was measured before mounting inside the DC cage of the CSC. From the measured activity and the extracted ^{219}Rn count rate the extraction efficiency can be calculated directly. In addition a laser ablation ion source is mounted at the entrance of the inner chamber of the cell [Rin12]. A discharge source is mounted about 30 cm away from the RF carpet at the DC ring electrodes of the CSC [Gre14]. These sources provide ions for tests, performance measurements and for calibration of accurate mass measurements with the MR-TOF-MS.

5.3 The RFQ beam line and diagnostics unit

Following the concept of [Pla07, Pet08], the beam line behind the stopping cell is based on a low-energy RF quadrupole transport system. This approach allows the beam line to be compact, provides for differential pumping in the vicinity of the stopping cell, ion cooling, transport, bunching, beam monitoring and mass separation. In principle a disadvantage of this approach is that the complete ion pathway has to be covered with RF structures for ion confinement and therefore gate valves and detectors are hard to implement. In the context of this work an RFQ-based beam line downstream of the cryogenic stopping cell was developed, which does allow the implementation of a gate valve and various detectors for ion identification and counting as well as test ion sources.

RFQs built from resistive RFQ rods with an rod diameter of 11 mm and distance

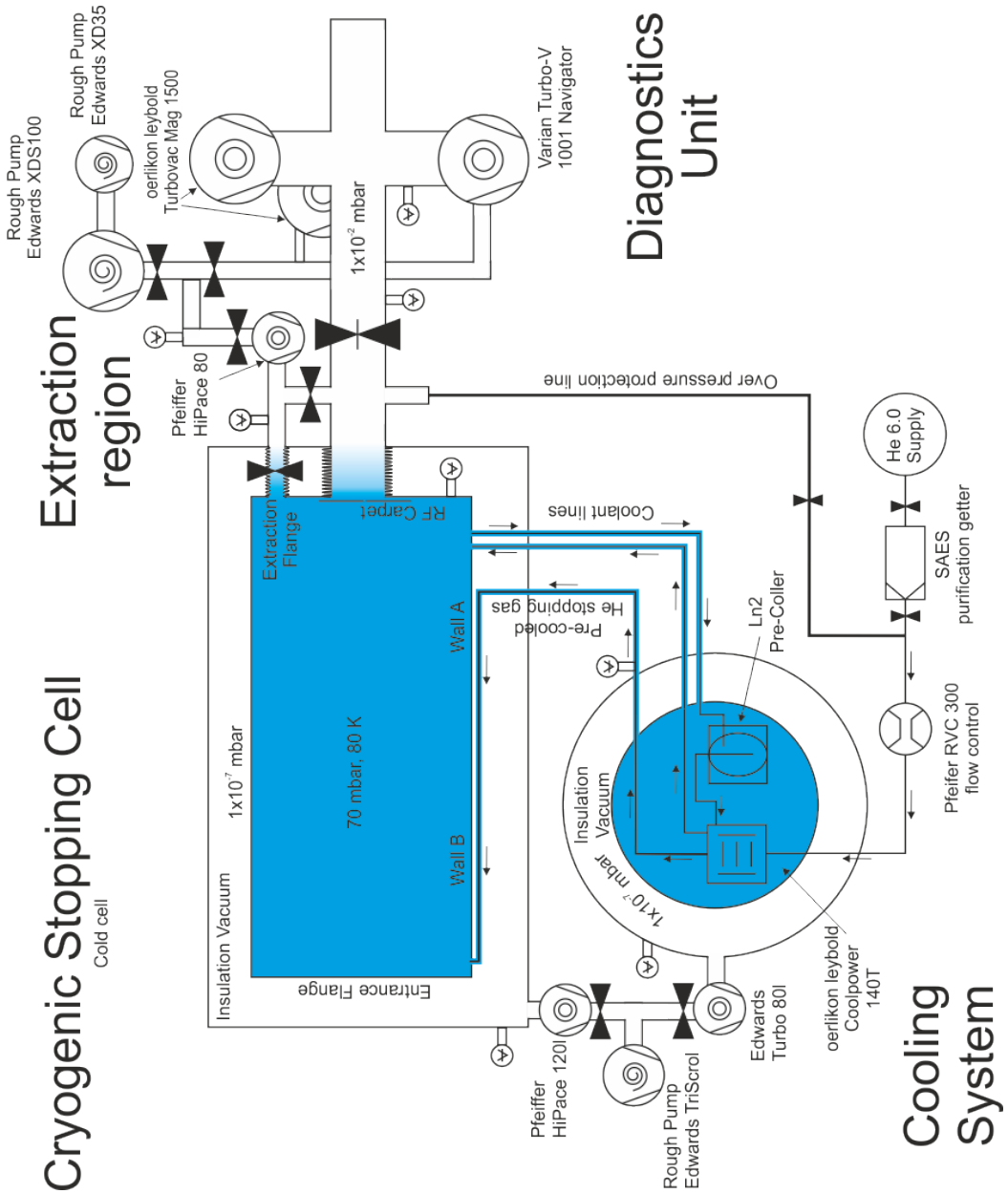

Figure 5.6: Differential pumping of the stopping cell, the cooling system and the diagnostics unit as during the 2014 FRS Ion Catcher experiment. The values for the pressure in the low energy RFQ beam line apply to the conditions during operation of the CSC.

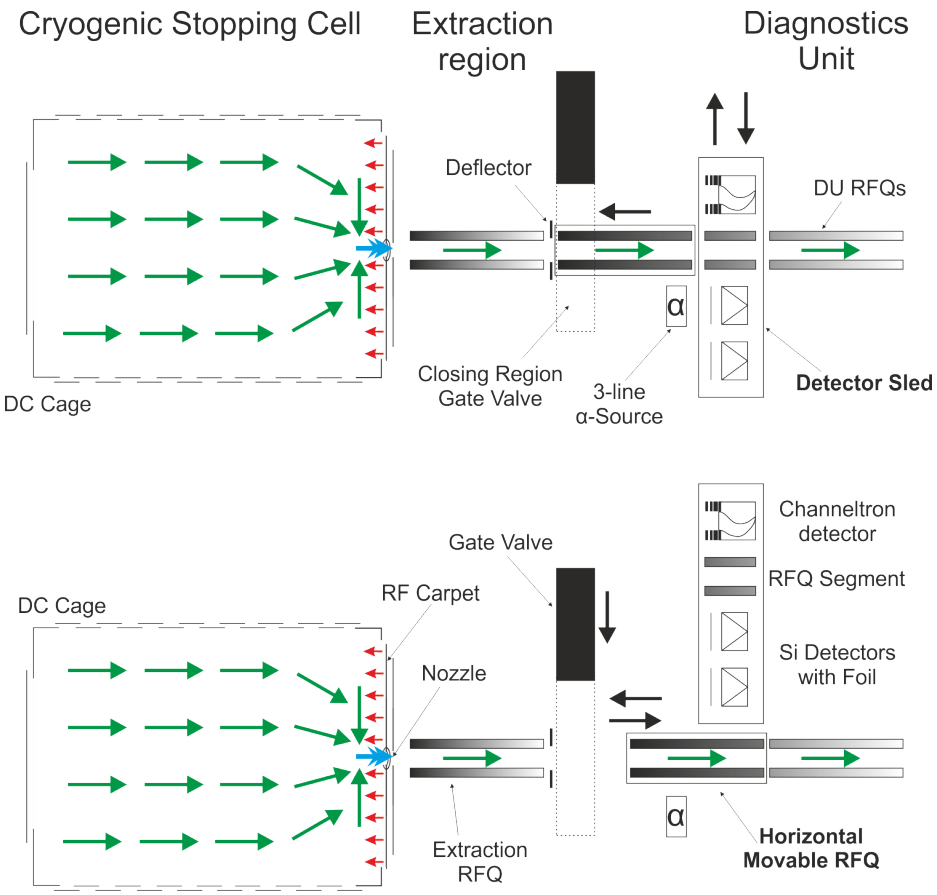

Figure 5.7: Schematic drawing of the CSC and the low energy RFQ beam line. (Top) The RFQ beam line is completed and allows transport of ions from the CSC to downstream experiments - e.g. MR-TOF-MS. (Bottom) The horizontal movable RFQ is retracted and gives enough free space for a gate valve to be closed. This way CSC and downstream beam line can separately be vented. Black arrows indicate the possible movements, colored arrows indicate the forces on the ions, see fig. 6.1 for description.

10 mm, transport the ions through the differentially pumped extraction region to downstream detectors. A set of three turbomolecular pumps, with a total pumping speed up to 4000 l/s, are used to pump the extraction region to a pressure of $8 \cdot 10^{-3}$ mbar during operation of the CSC at 64 mbar and 88 K, corresponding to an area density of 3.6 mg/cm^2. The full differential pumping scheme of the cryogenic stopping cell, the cooling system and the diagnostics beam line is shown in figure 5.6.

The diagnostics unit located behind the extraction RFQ enables detection, identification and quantification of the ions extracted from the stopping cell, see figure 5.7 . It consists out of three RFQ segments. The middle segment is located in an horizontal movable sled (referred to as detector sled), which in addition to an RFQ segment includes two identical setups of negatively biased aluminum foil and silicon surface barrier detector (Ortec Ultra BU-016-150-100 bakeable), a channeltron detector (Photonis 5901 Magnum Electron Multiplier), and a Cs ion source (Heat Wave Labs thermal ion source) for testing of instruments downstream of the diagnostics

unit. By tuning of the horizontal position of the detector sled using an in-vacuum step motor and gear system, the respective function of the diagnostics unit can be used. The channeltron detector setup includes a CuBe conversion dynode and can be operated in single ion detection mode at pressures up to $5 \cdot 10^{-2}$ mbar without increase of dark counts or loss in performance [Rei11]. A segmented aperture, mounted between the extraction RFQ and the diagnostics unit, is used as a dipole deflector. It can be used to attenuate the ion beam for the study of ions of strongly different abundance ratios and to determine the time profile of the extracted ions. In addition it can be used to only transmit ions from the CSC to downstream detectors, when ions of interest are stopped in the CSC. In addition a 3-line alpha source containing ^{239}Pu, ^{241}Am and ^{244}Cm is positioned of axis from the RFQ beam line such, that all detectors can be moved in front of the 3-line alpha source for commissioning or calibration of the Si detectors.

Vacuum separation between stopping cell and beam line for maintenance reasons is realized using a gate valve [Rei11]. The RFQ segment located in the closing region of the valve can be retracted to make way for the valve. This is archived by a dedicated movable RFQ segment mounted on a second horizontal sled. Within minutes the CSC can be vacuum-separated from the downstream beam line allowing e.g. repairs of detectors etc.

The extraction RFQ can be operated in broadband transmission mode or narrow band mass filter mode. Therefore ions from the ion sources and from the stopping cell can be mass-selected using the RFQ mass filter. In combination with different detectors a coarse mass determination or charge state identification of the ions extracted from the CSC can be performed.

5.4 The multiple reflection time-of-flight mass spectrometer

Behind the RFQ beam line a multiple reflection time-of-flight mass spectrometer (MR-TOF-MS) is installed [Pla13a]. It enables several operation modes. As a broadband mass spectrometer it can determine the abundances and identity of all ion species extracted from the stopping cell simultaneously. It can be used to optimize the range of ions delivered by the FRS or at future LEB and to verify the cleanliness of the stopping cell or its correct operation by broadband mass spectra. The MR-TOF-MS can be operated as an high-resolution mass separator to supply an isobarically [Pla08] and even isomerically pure beam [Dic15a] to following experiments. In addition, the device can perform mass measurements of very-short-lived and rare nuclides by itself. The MR-TOF-MS is described in detail in [Dic10, Dic15b].

Ions enter the MR-TOF-MS through a first RFQ segment and an RFQ switch yard [Pla15]. The RFQ segments are build similar to the RFQs in the RFQ beam line. In the RFQ switch yard the ion beam from the CSC can be merged with calibrant ions

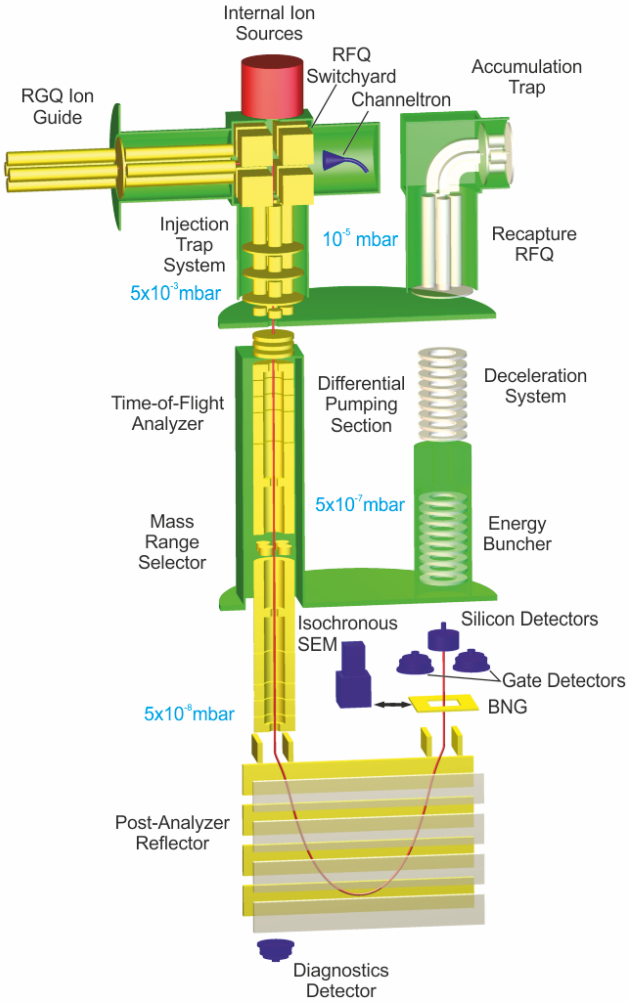

Figure 5.8: Schematic drawing of the MR-TOF-MS. In green the vacuum separation is shown, which provides differential pumping inside the MR-TOF-MS. In yellow ion optical elements are shown. [Dic15b]

from an electron impact ion source. In a triple-stage injection trap system [Jes08] the ions are accumulated, cooled by collisions with a buffer gas and injected as ion bunches into a time-of-flight analyzer. The trap system in addition performs a potential lift of the ions, this allows for tuning of the time-of-flight analyzer independent of the upstream beam line. The analyzer is formed by two electrostatic reflectors [Yav15]. In this the ions travel for a selectable number of turns, which determines the mass resolving power of the device. After ejection from the analyzer, the ions pass a post-analyzer reflector and selectively impinge on an isochronous secondary electron multiplier for measuring of their time-of-flight (mass measurement mode) or pass through a Bradbury-Nielsen Gate [Bra36], in which unwanted ions are deflected and detected by two gate detectors, thus only the ions of interest are transmitted (separator mode) [Vla95].

The performance of the MR-TOF-MS has been determined using off-line ion sources [Dic15b]. After a flight-time of 2 ms a mass resolving power of 100,000 has been

achieved [Pla15].

6 Characterization of the CSC and the RFQ beam line in off-line experiments

In order to use the cryogenic stopping cell during experiments at the FRS the device had to be commissioned beforehand. During the commissioning of the CSC and the low energy beam line its performance parameters, e.g. its maximal operation parameters, extraction and transport efficiency, cleanliness, extraction times etc. were measured. In addition the performance parameters of the prototype CSC give input for the design of the final cryogenic stopping cell for the LEB and are therefore of great interest for the technical realization of the future LEB.

In figure 6.1 the optimized typical voltages, which have been used during the commissioning experiments and at the experiments at the FRS, and their resulting forces are shown schematically. The voltages are given for the DC cage (1), the RF carpet (2) and its inner shielding layer (3), the extraction RFQ (4) and the diagnostics RFQ beam line (DU) (6). In addition the voltages used for the Si detector setup (7) and the channeltron detector setup with the additional conversion dynode (8) are given.

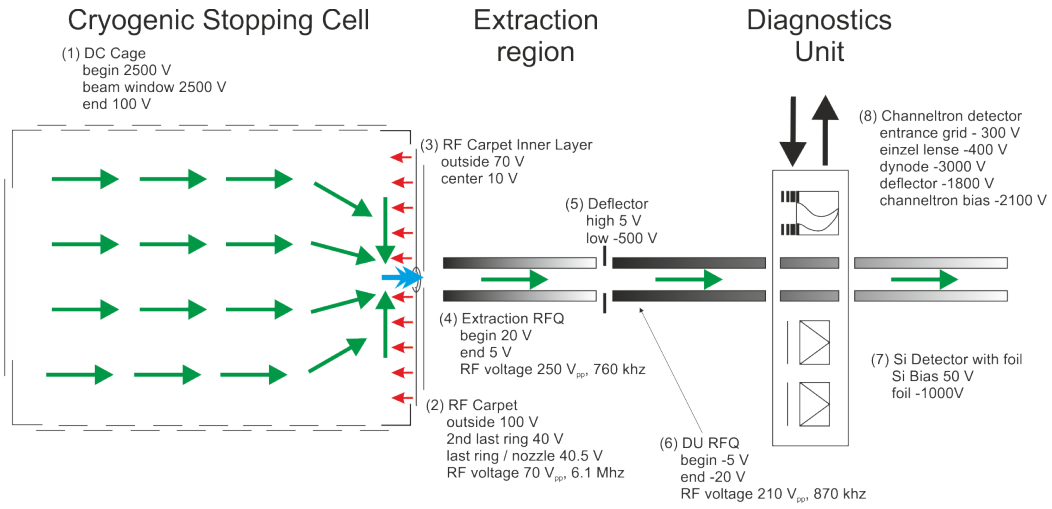

Figure 6.1: Schematic view of the cryogenic stopping cell and the RFQ beam line with typical DC and RF voltages for the individual components. In addition the resulting forces are shown schematically resulting from DC fields (green), effective RF field (red) and gas flow (blue).

6.1 Identification of ions in the diagnostics unit

The diagnostics unit provides first identification of ions extracted from the cryogenic stopping cell. It can be used to measure the identity and quantity of the ion population. The detector sled is equipped with different detectors as described above. In the following the performance of the three different detection schemes, (i) detection by alpha spectroscopy with a silicon surface barrier detectors, (ii) single ion counting and (iii) single ion counting in combination with the extraction RFQ operated as a mass filter, will be discussed.

6.1.1 Performance of the Silicon detector system

In order to perform alpha spectroscopy of exotic nuclei produced by in-flight projectile fragmentation at the FRS Ion Catcher the reliability of the detector system needs to be validated and its performance for alpha spectroscopy investigated.

The silicon (Si) detector system uses aluminum foils in front of a surface barrier Si detector for collection of the radioactive nuclei. It enables reliable operation of the detector, which has not to be floated to a high voltage for collection of the nuclei, but can be operated at ground. Therefore the data acquisition electronics can also be operated at ground. The collection foils need to be sufficiently strong in order to survive the evacuation of the chamber and not to break during motion of the detector sled. In addition, the usage of foils for the collection of the radioactive nuclides has the advantage that the activity is only deposited on the foil and not on the detector itself. Exchanging the foil removes collected activity and therefore removes decay back ground from the detection setup.

The resolution in the alpha spectra is limited by the aluminum foils. The foil causes a peak broadening by two effects. Firstly, energy straggling of the alpha particles, when penetrating the foil straight to the detector σ_{direct} and secondly, peak broadening caused by the difference in energy loss due to different angles of the alpha particle σ_{angle} [Sof77]. The maximal angle is defined by the geometry of the foil detector setup, which causes the particles to penetrate through a different amount of aluminum. The foil is placed 5 mm away from the surface of the Si detector, having an active area with a diameter of 13.8 mm. Thus the setup allows to measure alphas emitted under a solid angle of 0.83 π, resulting in a relative detection efficiency of about 0.21.

For experiments at the FRS in 2011 and 2012 special foils, made by evaporation by the GSI target laboratory, with a thickness of 200 μg/cm^2 aluminum were used, resulting in a peak width of $\sigma_{exp} = 48$ keV. The foils were changed to perform alpha spectroscopy with higher resolving power and to enhance the identification of alpha lines to a 100 μg/cm^2 aluminum foils for the 2014 experiments. Alpha spectroscopy with a peak width of $\sigma_{exp} = 26$ keV is possible. Table 6.1 gives an overview of the aluminum foils used. Figure 6.2 shows the corresponding alpha spectra of ^{219}Rn and

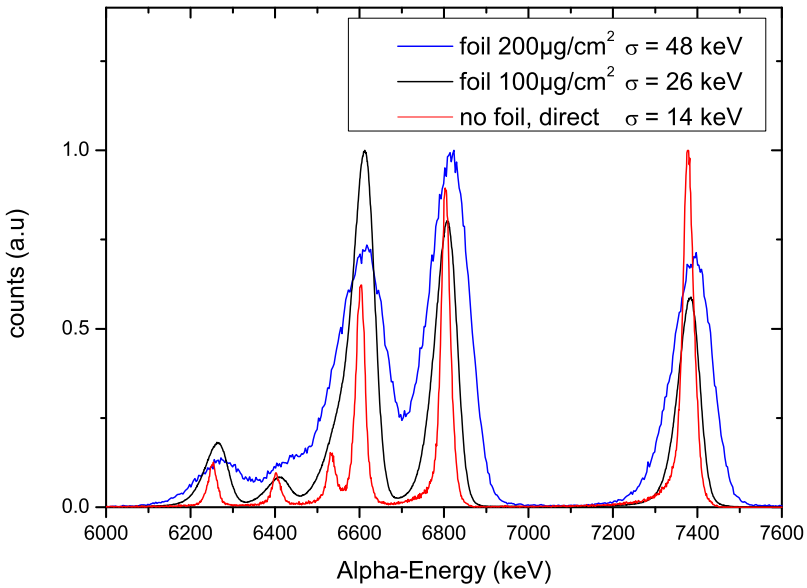

Figure 6.2: Measured alpha decay spectra of ^{219}Rn comparing different detector assemblies using 200 μg/cm^2, 100 μg/cm^2 Al collections foils and no foil in front of the Si detector in the DU.

the decays of its daughters extracted from the cryogenic stopping cell.

For future experiments it can be useful to exchange the collection aluminum foils to foils with a thickness of 50 μg/cm^2. With such thin foils the resolution will be dominated by the intrinsic detector resolution, but still providing stable foils. The detector and data acquisition resolution of 14 keV was determined and fits well with the specifications of the detector. This was verified by taking an alpha spectra without any aluminum foil in a separate vacuum chamber.

Al foil	σ_{direct} (keV)	σ_{angle} (keV)	σ_{cal} (keV)	σ_{exp} (keV)
200 μg/cm^2	8.8	37	40.8	48
100 μg/cm^2	6.1	18	24.2	26
50 μg/cm^2	4.3	11.3	19.3	-

Table 6.1: Comparison of the aluminum foils in front of the silicon detector assembly. The silicon detector has an intrinsic resolution of 14 keV. The energy straggling was calculated using [ATIMA].

6.1.2 Performance of the Channeltron detector system

The diagnostics unit is equipped with a channeltron detector. This type of detector allows the detection of single ions, typically at vacuum pressures below $9{\cdot}10^{-4}$ mbar.

In the vicinity of the CSC the residual gas pressures are typically too high for the usage of single ion detectors. The canneltron was built into a custom ion optics setup,

increasing the amplification by about a factor two and the detection efficiency by about a factor of seven of the detector by an additional CuBe [Rud79] conversion dynode [Rei11]. Thus it was possible to operate the channeltron at higher pressures with single ion sensitivity. Typical single ion pulses have a width of $\sim$ 5 ns and a pulse height of $\sim$ 60 mV. It was shown that the detector is performing well at pressures up to $8 \cdot 10^{-2}$ mbar, without an increased dark count rate. In addition it was possible to distinguish between alpha particles and ions by the pulse height of the single ion events. Alpha particles reach pulse heights of > 100 mV and could thus be omitted using a ΔE-discriminator. With this it is possible to remove the alpha decay background from the channeltron detector signals and use it more efficiently for single ion counting and optimization of the beam line.

6.1.3 Extraction RFQ as a mass filter

For alpha-decaying nuclei the identification of ions in the diagnostics unit of the RFQ beam line is performed by alpha spectroscopy. In order to enable the identification of other ions, in particular stable nuclei or molecules, the extraction RFQ of the CSC was modified to operate as an RF mass filter [Mis14, Mis15] with dedicated electronics [Hea11]. Thus it is possible to identify ions by their mass-to-charge ratio directly behind the stopping cell. The mass filter can provide mass-to-charge information of ions between 30 u/e and 250 u/e. Typical mass spectra can be taken with a resolving power of 10, while achieving a transmission efficiency of 80 %. Besides mass identification, the extraction RFQ can be used as a mass filter, transmitting a narrow mass window only and reducing the number of transmitted ions down to the required mass region.

The mass resolving power can be increased further, but as shown in figure 6.3 higher resolving powers lead to reduced transmission. Despite the high pressures the mass-filter provides mass selective ion transport with resolving powers of up to 150 at residual gas pressures of $8.4 \cdot 10^{-3}$ mbar. The performance of the mass filter at high residual gas pressures is of special importance, as the buffer gas emerging from the CSC is pumped away in the extraction region and therefore the areal density of the CSC is determining the residual gas pressure in the diagnostics unit.

The rough mass-to-charge identification of ions directly behind the CSC allows systematic investigations of the performance of the CSC. Furthermore a measurement of the mass-to-charge ratio directly behind the stopping cells enables optimization of the complete downstream beam line for a certain mass-to-charge range. In addition the mass filter can suppress unwanted ions and decrease space charge effects and contamination inside the more sensitive parts of the downstream low energy beam line.

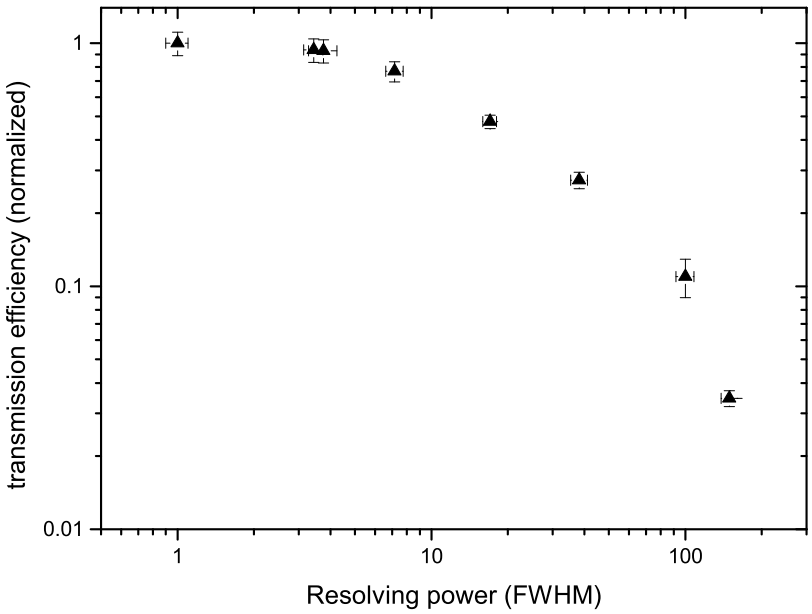

Figure 6.3: Measurement of the transmission efficiency as a function of resolving power of the extraction RFQ operated as a mass filer at an area density of the CSC of 4.0 mg/cm^2 He corresponding to a residual gas pressure of $8.4 \cdot 10^{-3}$ mbar in the diagnostics unit.

6.2 Characterization of the RFQ beam line

6.2.1 Characterization of the differential pumping

In order to achieve the highest possible stopping efficiency the stopping cell needs to operate at the highest possible area density. At the same time the pressure in the differential pumping station, the RFQ beam line and the diagnostics unit, should not be too high for long-term operation of turbomolecular pumps and not limiting the transport efficiency to downstream parts of the beam line. To allow a stable operation of the full setup a compromise between area density of the CSC and the load on the turbomolecular pumps needs to be found. This was done by varying the area density of the CSC while recording the pressure in the DU. In figure 6.4 it can be seen that vacuum pressure in the DU increases linearly with the area density of the CSC. At 3.5 mg/cm^2 a change in slope can be observed. This is caused by the loss in pumping speed of the turbomolecular pumps at vacuum pressures above $1 \cdot 10^{-2}$ mbar. In comparison the differential pumping during the 2012 experiment is shown. At that time the DU was pumped by two Agilent 1100 Navigator pumps. For the 2014 experiment the pumping speed was almost doubled by using two Oerlikon MAG Integra 1700 and one Agilent 1100 Navigator turbomolecular pump, resulting in a lower residual gas pressure at same operation area density of the cyogenic stopping cell. Thus the stopping cell can be operated at a higher area density while resulting in the same residual gas pressure in the fits differential pumping section.

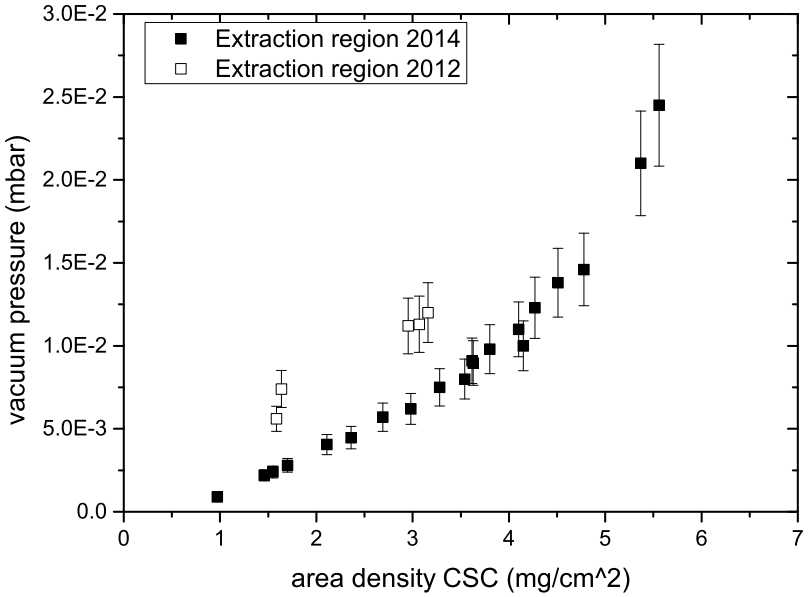

Figure 6.4: Differential pumping of the stopping cell. Showing the pressure measured in the RFQ beam line for different area densities at the CSC. A change in slope can be seen at 3.5mg/cm^2, corresponding to a reduction of pumping speed of the turbomolecular pumps at higher pressures.

From the measurement as a standard working point an area density of 3.5 mg/cm^2 was chosen, resulting in a vacuum pressure of $8 \cdot 10^{-3}$ mbar. This area density allows a stable long term operation of the setup. A high pressure mode with up about 6.3 mg/cm^2 is possible. However this results in a pressure of $1.0 \cdot 10^{-1}$ mbar in the extraction region. Under this conditions the lifetime of the turbomolecular pumps will be reduced and the high pressure mode should only be used for a few hours.

6.2.2 Characterization of the RFQ ion transport system

To achieve high transport efficiencies at high vacuum pressures in the extraction region and the diagnostics unit carbon filled PEEK RFQ rods are used. The transmission efficiency to the silicon detector in the diagnostics unit for ^{219}Rn ions from the CSC was validated over a wide pressure range. To perform the measurement shown in figure 6.5 the three turbomolecular pumps were switched off and the residual gas pressure in the diagnostics unit increased up to 0.5 mbar. At the highest pressures a slight drop in transport efficiency can be seen. The hashed area shows the typical range of vacuum pressure the RFQ beam line is operated at. The transport efficiency to the Si detector is almost independent against pressure changes. In addition the transport to the MR-TOF-MS was investigated up to 0.1 mbar, not showing a significant reduction in transport efficiency.

The movable detector sled in the DU allows to interchange between different detectors and a RFQ segment for transportation of the ions extracted from the CSC to down-

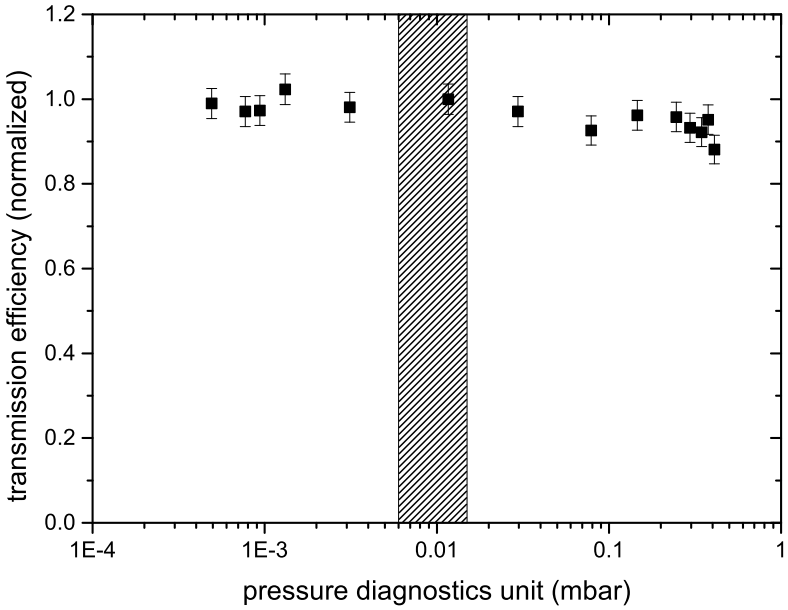

Figure 6.5: Transmission efficiency for ^{219}Rn ion through the RFQ beam line for different vacuum pressures measured with the Si detector in the DU. The shaded area indicates the range of typical operation pressures.

stream experiments, e.g. the MR-TOF-MS. During the optimization of the transport to the MR-TOF-MS the alignment of the RFQ segment within the upstream and downstream RFQs was varied. Figure 6.6 shows a normalized transmission efficiency of ^{219}Rn, ^{211}Pb, ^{207}Tl ions to the MR-TOF-MS. It can be seen that the RFQ segment need to be positioned with an accuracy of 1 mm. The detector sled allows repositioning of the detectors or RFQ segment in the order of 0.2 mm. This means that during experiments the position of the detectors or the RFQ segment does not need to be optimized, as they can be positioned sufficiently precise. In addition the measurement shows how precise subsequent RFQ segments need to be aligned in order to allow a high transmission efficiency $> 90\%$. All RFQ segments in the diagnostics unit are aligned to about $0.2 - 0.5$ mm accuracy, providing efficient ion transport.

RFQs can be used as high transmission ion guides in the vicinity of gas filled stopping cells at high vacuum pressures. An additional advantage compared to beam lines with static fields is the easy tuning and optimization of the voltages required for transmission of ions. The transmission efficiency of the extraction RFQ of the DU for different RF voltages was investigated. It shows that ^{219}Rn ions can be transported at RF voltages of at least 80 V_{pp} with full transmission. In order to prevent discharges the RF voltage was raised up to maximal 550 V_{pp}. Typically the extraction RFQ is operated with about 230 V_{pp} which would allows the transmission of a broad mass window from 120 u to 700 u.

The performance of the low energy beam line at high vacuum pressure environments shows that carbon filled RFQs can provide an efficient ion transport and are an excellent choice for beam lines following a gas filled stopping cell.

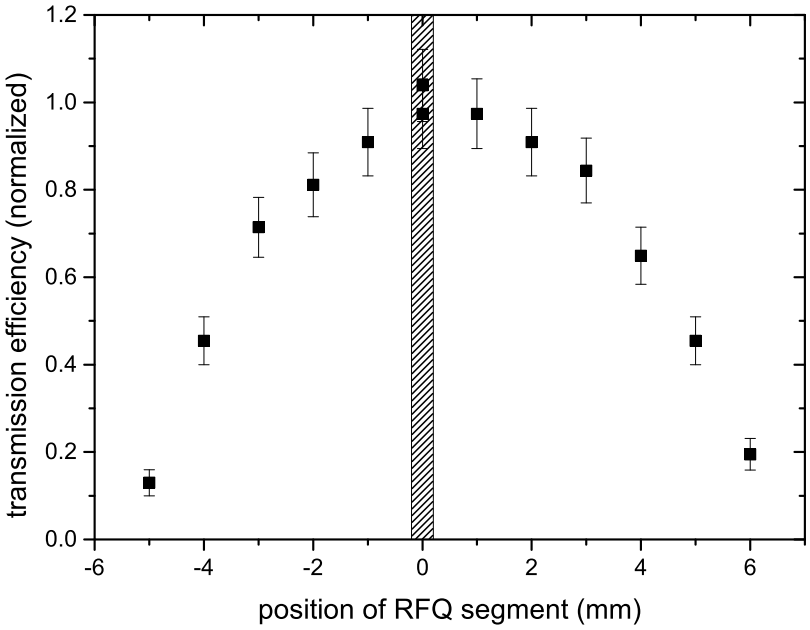

Figure 6.6: Transmission efficiency of ^{219}Rn ions through the RFQ beam line determined with the MR-TOF-MS while varying the position of the RFQ segment of the detector sled. The shaded area indicates the typical positioning precision of the detector sled.

6.3 Cleanliness of the CSC

As discussed in section 4 and shown in figure 4.3 cleanliness is of high importance for all types of stopping cells. The amount and the type of impurities limit the extraction efficiency. If a high amount of impurities is present the ions can form molecules and get extracted with adducts. Also impurities will be ionized by the beam and will be extracted from the stopping cell. Thus a broad mass composition will be detected, which can easily contain contaminants with up to orders of magnitude higher abundance compared to the ion of interest.

The cleanliness of the CSC can be investigated with different approaches. Residual gas spectra (RGA spectra) give information about the type of impurities present in the CSC. A determination of the extraction efficiency for ions in different charge states allows estimates on the total amount of impurities. At high cleanliness levels the extraction of ions in two or three plus charge states become more likely. The final test is the operation of the CSC under online experiment conditions. In this case the ions will deposit energy during their slowing-down and stopping in the stopping cell. By this the residual gas atoms are ionized and a large amounts of He-electron pairs are created. This can be up to 10^7 He-electron pairs per incoming heavy ion [Rei15]. Under these conditions the formation of molecules and the ionization of molecules may be increased, therefore the ratio between exotic nuclei and impurity ions can be reduced. The first two approaches have been investigated offline and the later was characterized during the FRS Ion Catcher experiments at GSI in 2012 and 2014.

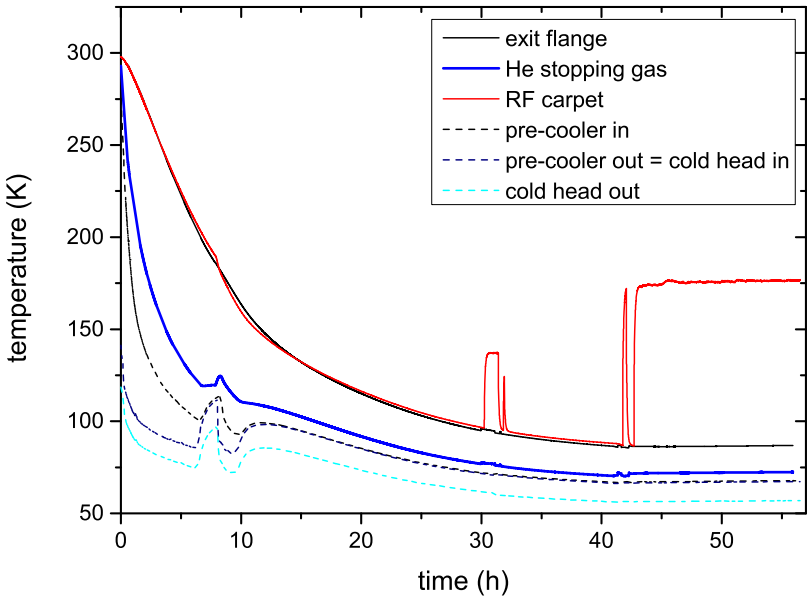

Figure 6.7: Cool down characteristics of the CSC and the cooling system. The temperatures during cool down were measured during the 2012 FRS Ion Catcher experiment at GSI [Ran14].

6.3.1 Cool-down characteristics of the CSC

The prototype stopping cell for the LEB is designed as a cryogenic stopping cell with the goal to reach the required cleanliness and purity of the helium stopping gas.

Figure 6.7 shows the cool down of the CSC during the 2012 FRS Ion Catcher experiment at GSI. The temperature of several parts of the CSC (solid lines) and the cryostat (dashed lines) were logged during cool down. The stopping cell was cooled with maximum cooling power using both, the internal LN_2 pre-cooler and the cold head for supplying coolant helium gas for the CSC. After about 7 h the LN_2 flow to the pre-cooler was switched off. This can be seen by the temperature increase of the pre-cooler sensors after about 7 h. After about 24 h the final temperatures are almost reached and the CSC is ready for operation. Finally the helium stopping gas reaches temperatures down to 74 K.

In addition it can be recognized that the RF-carpet is the hottest spot in the CSC. The coldest spot are the walls of the inner UHV chamber next to the cooling channels, reaching temperatures down to 50 to 55 K. If the RF voltage is turned on, the RF carpet, in particular the coil of the RF circuit, heats up by about 80 to 100 K. For the 2014 FRS Ion Catcher experiment the RF-Carpet was revised, allowing lower temperatures. This was achieve by coupling the coil of the RF circuit thermally to the He buffer gas by placing it in the stopping volume of the cell, resulting in a much lower RF carpet and coil temperature. Now, applying a RF voltage to the RF carpet results in a temperature increase of only ~ 30 K. Typical temperatures during long-term operation during the 2014 experiment are shown in table 6.2.

The CSC can be warmed up with a PTFE based heating band warped around the inner UHV chamber. The heating band provides about one kW of heating power and allows warm up of the CSC in about 6 h.

Sensor	temperature (K)	Sensor	temperature (K)
Entrance Flange	66	He Buffer Gas	84
Chamber Wall A	60	RF Carpet	105
Chamber Wall B	66	Exit Flange	65
pre-cooler in	62.8	pre-cooler out	62.8
cold head out	54.6		

Table 6.2: Temperatures of the CSC (top) and the cooling system (bottom) during long-term operation at the 2014 FRS Ion Catcher experiment. The CSC is operated at a pressure of 65 mbar, corresponding to 3.8 mg/cm^2 area density.

6.3.2 RGA spectra of the inner chamber

The stopping volume can be evacuated down to a pressure of $6 \cdot 10^{-6}$ mbar by a turbomolecular pump. RGA mass spectra at this pressure at room temperature show no mass lines above mass 58 u, which is typical for a clean UHV system. If the stopping chamber of the CSC is filled with 60 mbar helium gas, this partial pressure of rest gas corresponds to an impurity level of about ~ 100 ppb. For operation the system needs to be separated from the turbomolecular pump and the amount of contaminants will increase, because the stopping volume is no longer pumped. Separating the stopping cell at room temperature from the turbomolecular pump results in an residual gas pressure of low 10^{-3} mbar.

When the stopping volume is cooled down, 53 K at the walls of the chamber and 100 K at the inside of the DC cage are reached. This results in a residual gas pressure of $3.6 \cdot 10^{-8}$ mbar while still pumping with the turbomolecular pump. Through the cool-down the residual gas pressure could be reduced by a factor of ~ 150. It was seen in the RGA mass spectra that the mass lines caused by molecules were reduced to a level below the sensitivity of the RGA of $1 \cdot 10^{-11}$ mbar.

In order to estimate the amount of impurities in the helium stopping gas during operation, a RGA spectra was taken after separating the inner chamber from the turbomolecular pump, placed at a room temperature connection. The spectra in figure 6.8 shows the contaminants present in the CSC when the inner chamber is only pumped by the cryogenic surfaces of the CSC. Assuming no impurities are added to the system by the helium gas supply, this would correspond to a cleanliness at the ~ 5 ppb level. Through the cool-down the residual gas pressure of the encapsulated cryogenic stopping cell is improved by a factor of $\sim 10^3$ compared to room temperature, resulting in a residual gas pressure of $2.3 \cdot 10^{-7}$ mbar for the closed cryogenic stopping cell.

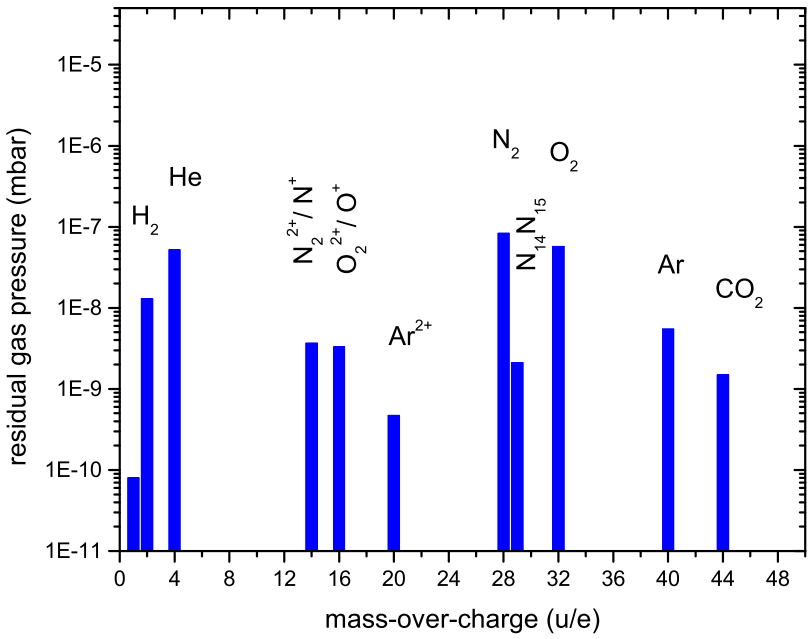

Figure 6.8: Residual gas spectra of the closed CSC measured at cryogenic temperatures. The CSC is separated from any room temperature parts and only pumped by the cryogenic chamber. The spectra shows the composition of the remaining contaminates in the CSC at a chamber wall temperature of 53 K and a temperature of 100 K inside the CSC.

It can be seen that separating the CSC from any room temperature parts completely removes all water molecules from the system, as the water typical mass lines at 17 u and 18 u are not present in the RGA spectra. The remaining impurities can be identified by their mass and by the knowledge of their boiling point and vapour pressure (see figure 4.4) and are labeled in figure 6.8.

6.3.3 Extraction at different temperatures

The effects occurring while cooling down the inner chamber of the CSC can not only be seen in the residual gas spectra but also in the extraction efficiencies. To investigate this, the extraction efficiency of ^{219}Rn ions from the internal source was measured at different temperatures. The ^{219}Rn ions were identified by their alpha decay on the Si detector in the diagnostics unit. For these measurements the CSC was prepared for operation in two ways:

First, the CSC was pumped down to a residual gas pressure of about $1 \cdot 10^{-5}$ mbar without baking, separated from the turbomolecular pump, filled with helium gas and extraction was started. Figure 6.9 shows the extraction efficiency as a function of temperature of the helium gas. For the non-baked CSC a steep increase in efficiency can be observed at a temperature of about 120 K. The extraction efficiency then saturates at about $(62 \pm 6.4)\%$ for temperatures below 100 K. This increase in ex-

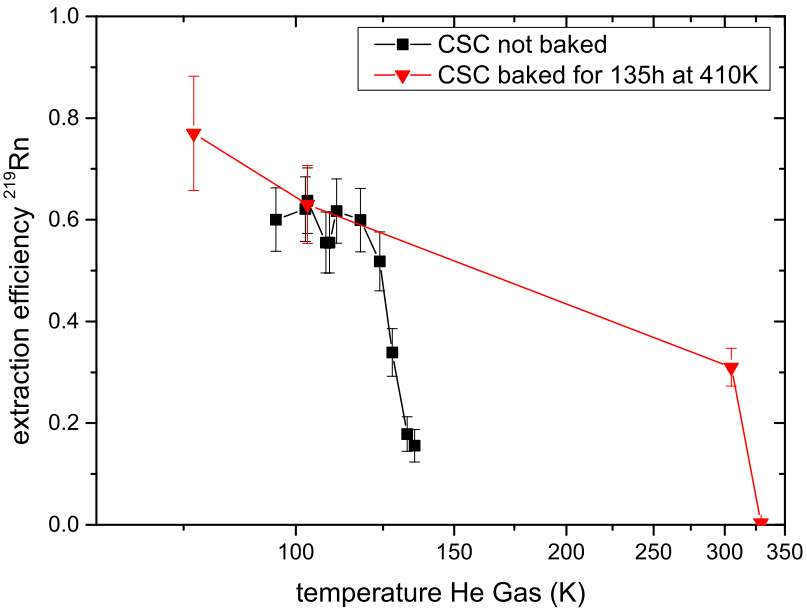

Figure 6.9: Extraction efficiency of ^{219}Rn ions from the CSC at different temperatures of the CSC. The measurement was done for two different preparation cycles of the CSC. Therefore the CSC was one time not baked at all, the other time baked for 135 h at 410 K.

traction efficiency at low temperatures is in agreement with previous measurements of [Den06]. It needs to be mentioned that in the measurements of [Den06] the He gas was polluted with about 300 ppm of room air, resulting most probably in a lower saturation efficiency at low temperatures.

Second, the cool down measurement was repeated, but this time the CSC was baked for 130 h at a moderate temperature of 410 K while being constantly pumped with the turbomolecular pump. During cool-down the extraction efficiency was monitored. It was possible to extract about $(30 \pm 4)\%$ of the ^{219}Rn ions even at room temperature. The extraction efficiency could be increased up to $(77 \pm 11)\%$ at 77 K. This value compares favorably with the results obtained by [Dro14] and other ultra pure stopping cells [Hui04].

The comparison shows that baking the cryogenic stopping cell at moderate temperatures increases the cleanliness significantly. Furthermore baking of a vacuum system at temperatures of 420 K or below does not put strong limitations on the design of the CSC and the choice of materials. Since the need of baking at temperatures of 550 K or above, which are typical for room temperature UHV systems, the use of the RF carpet technology becomes possible with the CSC. The RF carpet of the cryogenic stopping cell would not be able to stand such high temperatures.

In order to get a deeper understanding of the behavior during cool-down mass spectra were recorded with the MR-TOF-MS during cool-down from room temperature down to 100 K using the cooling power provided by the cold head only. While cooling down the CSC a mass spectrum was taken every minute. Two sample spectra of the ion

composition extracted from the CSC are shown in the figures 6.10 and 6.11. Figure 6.10 shows the mass spectrum at room temperature between mass 200 u and 240 u taken at resolving power of $m/\Delta m \sim 5000$ at the MR-TOF-MS. At room temperature at each mass line in the spectra several isobars can be detected. Attempts to measure the mass e.g. of ^{219}Rn would suffer from strong back ground. After cool-down to about 140 to 160 K the mass spectrum changes drastically and the three remaining dominant peaks can be assigned to the characteristic ions produced by the ^{223}Ra recoil ion source, see figure 6.11. During cool-down the total amount of extracted ions is reduced by more than two orders of magnitude. The clean mass spectrum demonstrates the excellent cleanliness of the cryogenic stopping cell under low to medium ionization densities. The ^{223}Ra recoil ion source produces only light ionization in the CSC. A measurement during online commissioning at the FRS Ion Catcher will be shown later.

In conclusion, ions perform about 10^7 to 10^8 collisions before they are extracted from the stopping volume into the RFQ beam line. Collisions in the RFQ beam line can be neglected because of the much lower residual gas pressure. Thus from the extraction efficiency the cleanliness of the stopping gas can be estimated. For the extraction efficiency measurement at 77 K, done at an area density of 1.7 mg/cm^2, the ^{219}Rn ions undergo $\sim 5 \cdot 10^7$ collisions. Thus a helium gas purity of about 10 ppb is derived. This result fits nicely to the estimate of 5 to 10 ppb made in chapter 4 and figurecollision.

For the long term operation of the cryogenic stopping cell the impurities added to the stopping volume by the helium gas need to be taken into account. The impurities of helium 6.0 are listed in table 6.3. The initial level of cleanliness of the helium 6.0 is not sufficient for the usage as a stopping gas. The helium gas needs to be purified further in order to meet the ~ 1 ppb purity level. This can be achieved using a passive purification getter (SAES MicroTorr MC400-902V) and a cold trap. The improved impurity levels expected behind the getter are listen also in table 6.3.

Impurity	Concentration [ppb]	Purification technique	Concentration after purification [ppb]
CO	≤ 100	MicroTorr	< 0.1
CO_2	≤ 100	MicroTorr	< 0.1
hydrocarbons (> 100amu)	≤ 50	MicroTorr + Cryo	< 0.001
CH_4	< 50	-	< 50
H_2	≤ 100	MicroTorr	< 0.1
H_2O	≤ 500	MicroTorr + Cryo	< 0.1
N_2	≤ 500	-	≤ 500
O_2	≤ 200	MicroTorr	< 0.1
Ar	≤ 500	-	≤ 500

Table 6.3: Impurities present in the helium 6.0 before and after the additional purification using a MicroTorr getter material and a cold trap.

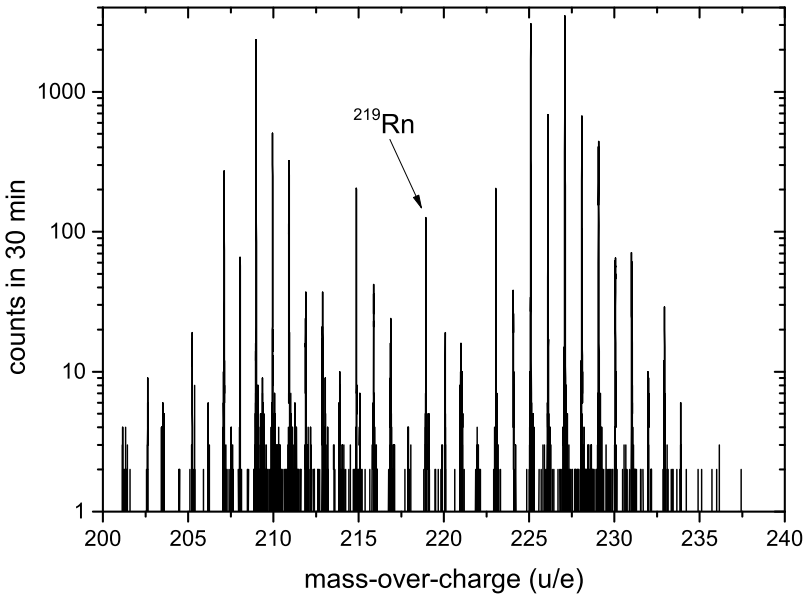

Figure 6.10: Mass spectrum of ^{219}Rn ions extracted from the ^{223}Ra offline source while the CSC is operated at room temperature. The ionization of the recoil source produces a full mass spectrum. The mass line ^{219}Rn is hard to identify.

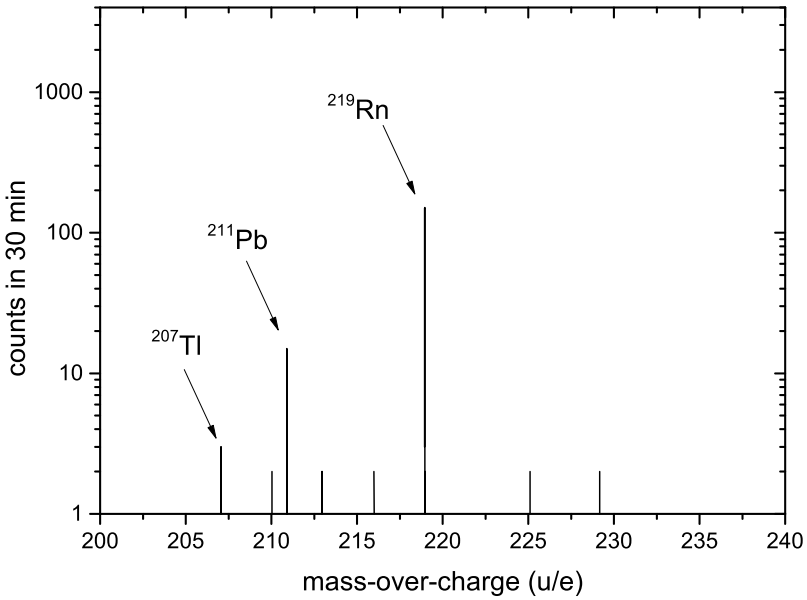

Figure 6.11: Mass spectrum of the recoil ions from the ^{223}Ra source at 140 to 160 K. The characteristic mass lines corresponding to ^{207}Tl, ^{211}Pb and ^{219}Rn are clearly visible, almost no background can be seen in the mass spectra.

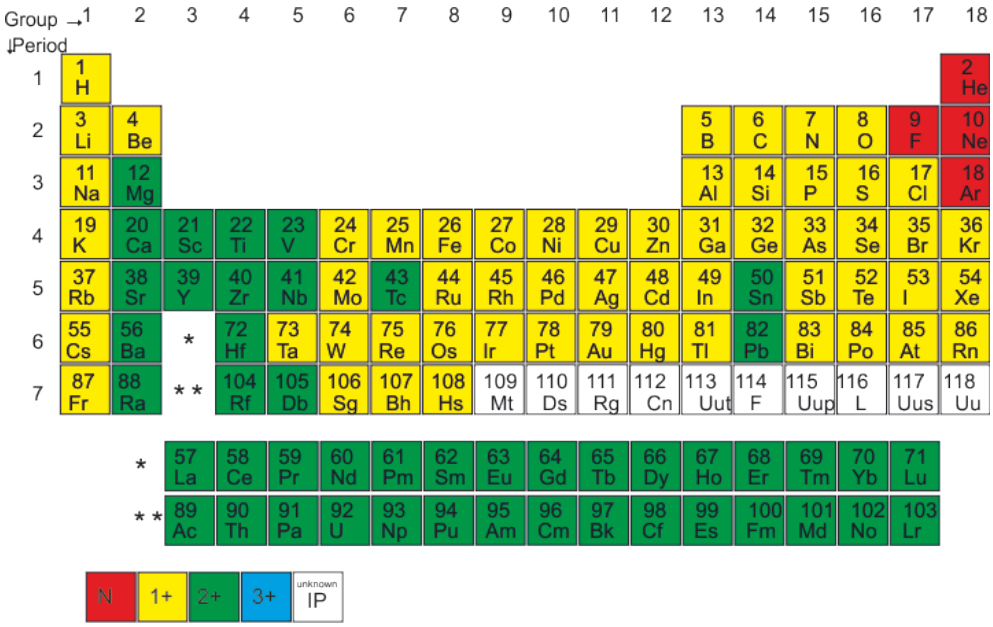

Figure 6.12: Estimated charge state distribution of elements extracted from the cryogenic stopping cell. The charge state is derived from the first, second and third ionization potential of each element in comparison the the ionization potential of N_2 of 15.6 eV. Ionization data was taken from the NIST database [Kra14].

The table shows that the main contamination brought into the cryogenic stopping cell by the stopping gas are N_2, Ar and CH_4, which will not be filtered out by the cold trap or the purification getter. From those N_2 is the most prominent contamination with ≤ 500 ppb. In addition it has a significant lower ionization energy of 15.6 eV compared to helium. Thus N_2 is lowering the charge state in which an ion of interest will be extracted from the cryogenic stopping cell. The expected charge state distribution is shown in the periodic table for N_2 present in the stopping volume, figure 6.12. In order to improve the N_2 and CH_4 impurities levels to below 1 ppb an active (heated) getter material can be used, such as SAES MonoTorr series (Phase I PS3-MT3-R/N).

The expectation for the charge states will be compared to the experimental results, obtained for ions from the offline sources and relativistic ions thermalized in the stopping cell from the FRS, in chapter 7.2.2.

6.4 Extraction time of ions from the CSC

An important performance criterion for a stopping cell is its extraction time, i.e. the time ions need to get extracted from the stopping volume of the stopping cell into the low energy beam line. This time is especially important if short lived ($t_{1/2}$ ~ms) exotic nuclei are the aim of the experiment.

The extraction time was measured by pulsing the potential of the internal ^{223}Ra source. A negative voltage was applied to the recoil source relative to the surrounding electrodes, preventing the recoils from leaving the proximity of the source [Pla13a]. With a repetition rate of 1 Hz the source was pulsed to a positive voltage for a time interval of 20 ms. This allowed the ions to leave the source and get extracted from the cell. A deflector at the end of the extraction RFQ was used to deflect all ions coming from the stopping cell, except those arriving within a 30 ms window, after a selectable delay. This measurement was repeated several times, scanning the delay time between opening the source and the deflector between 0 and 80 ms [Pla13a]. The resulting curve of this measurement is shown in figure 6.13. A Gaussian-like time profile is observed with a mean delay time of 46 ms. Deconvolution of the measured profile with the time windows for pulsing of the source potential and the deflector in front of the detector yields a mean extraction time of 51 ms [Pla13a]. This value is compatible with the drift time of 48 ms calculated using ion mobility theory with a reduced ion mobility value of 17.5 cm^2/(Vs) [Vie95, Vie12] and simulations, which show that under typical operating conditions the transport along the RF carpet takes place with similar velocities as in the drift region of the stopping cell [Rei11]. Simulations that take into account realistic electric fields result an extraction time of 45 ms. It needs to be mentioned that in this experiment the ions had to travel along the whole length of the stopping cell. Therefore the ^{219}Rn ions need to be pulled by a DC electric field of 19.4 V/cm through a length of 103 cm. The stopping cell was operated at 50 mbar and 102 K, corresponding to an area density of 2.5 mg/cm^2 He.

In an on-line experiment relativistic stopped ions will be distributed along the cell with an abundance maximum in the central region of the cell. Hence for ions from a stopped beam the mean extraction time will be only about half of the value measured in the off-line experiment, resulting in a mean extraction time of about 25 ms. The measurement described above was repeated several times for different extraction DC fields. It was found that the extraction time scales with mobility for different DC fields along the body of the CSC. In addition the measurement was performed for two different area densities of the CSC. The measurements indicate that for a higher area density also a higher DC field can be applied to the DC electrodes of the CSC. Therefore a mean extraction time of about 25 ms can be reached at 1.3 mg/cm^2 as well as at 2.5 mg/cm^2 He.

In order to investigate the pressure dependence more quantitatively the maximal applicable DC field along the body of the CSC was measured at different area densities. The DC field is created by applying a high voltage to the first DC ring of the DC body and a low voltage to the last DC ring. A resistor chain connects the 33 rings of the DC body and creates a homogenous DC field. The minimal distance between the high voltage electrodes and the walls of the vacuum chamber, being on ground, is 7 cm. In the following it will be assumed that the maximal DC field is limited by discharges occurring from the first DC ring to the surrounding vacuum chamber. Figure 6.14 shows the maximal high voltage that could be applied to the first DC ring at different area densities of the CSC. The so called break down voltage can be described by Paschen's law [Pas89], giving a relationship between the break down

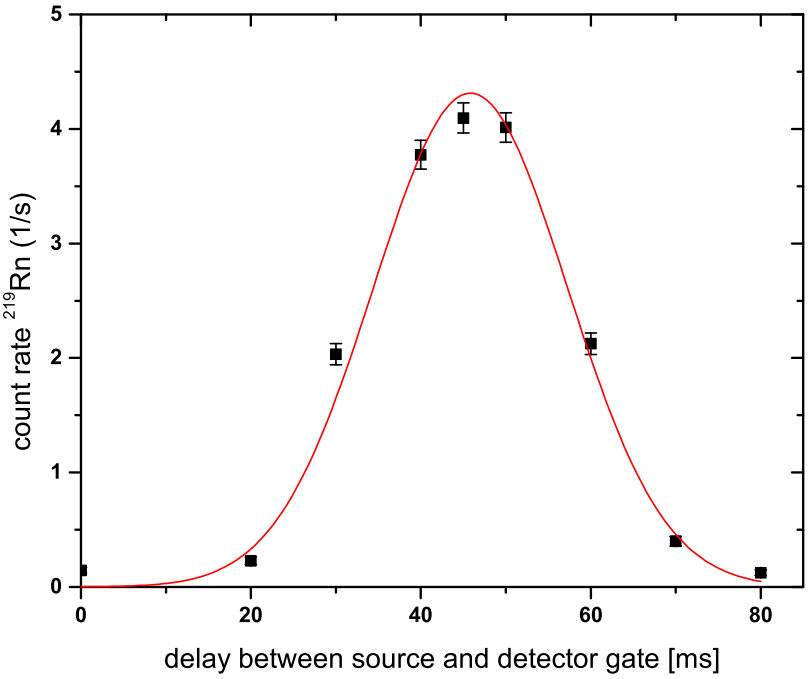

Figure 6.13: Measurement of the extraction time of ^{219}Rn. The count rate of α decay on the Si-1 detector in the diagnostics unit is given in dependence of the time delay between pulsing of the potential of the ^{223}Ra source and the pulsing of the deflector in front of the detector. The curve shows a Gaussian fit to the data. [Pla13a]

voltage and the product of distance and density. In comparison to our measurement the predictions for the Paschen curve are given from [Gerh98, Pet04, CIGRE]. Our measurement of the break down voltage compares to the band given by the different predictions. From this we assume that our assumption was correct and the limiting distance is between the first DC ring and the vacuum chamber.

From the maximal voltage the maximal operation DC field along the CSC can be calculated and by mobility theory the extraction time of ions from the CSC be derived. Figure 6.15 shows the resulting mean extraction time for different area densities between 1 mg/cm^2 and 10 mg/cm^2. A mean extraction time of $\sim$ 25 ms can be achieved almost independently of the area density of the CSC. This shows that the minimal mean extraction time of a given stopping cell is independent of the area density of stopping cell and that the extraction time is defined by the design of the cell.

In order to achieve short extraction times already during the design the path, the ions need to travel inside the CSC, needs to be considered and the system needs to be designed in order to allow high extraction field strengths.

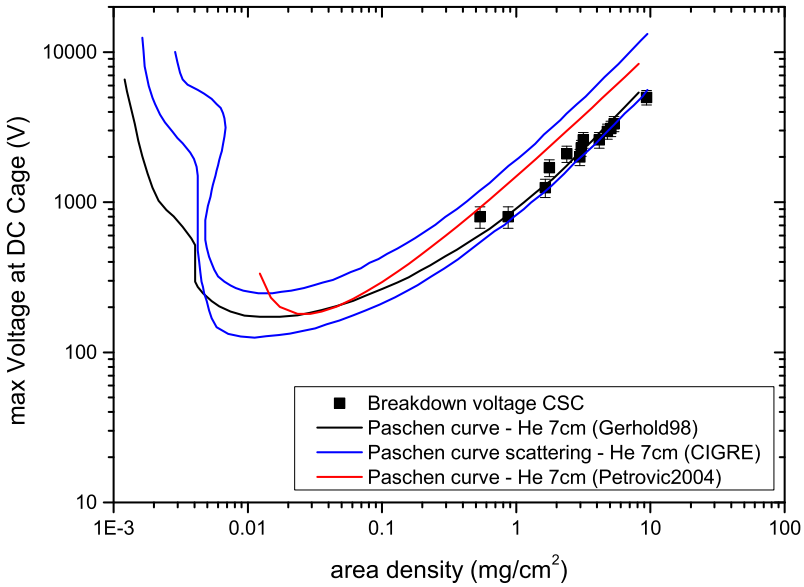

Figure 6.14: Measurement of the maximal applicable voltage at the high voltage side of the DC body of the CSC for Helium as a stopping gas. The resulting DC field is used to perform calculations of the extraction time of ions from the CSC.

6.5 Operation of the RF Carpet

The ions are pulled by the DC electric field to the extraction side of the CSC. There the RF electric field of the RF carpet produces a pseudopotential wall that prevents the ions from hitting the electrodes, as described in section 3.5.2. A superimposed DC electric field transports the ions to the center of the RF carpet, where they get extracted from the CSC into the RFQ beam line through a cylindrical nozzle by the gas flow.

6.5.1 Required RF power for transmission at different area densities

The effective field E_{eff} needs to counter the DC electric field of the stopping cell E_{DC}. The relationship between the two allows to test the behavior of the ions at the RF carpet at different pressures. Experimentally this is studied by keeping the CSC at a fixed operation pressure and temperature and scanning the required RF voltage on the RF carpet for extraction of ^{219}Rn ions. With increasing amplitude the effective field gets stronger and from a certain amplitude on it is able to prevent the ions from touching the surface of the RF carpet. Several such RF scans are shown in figure 6.16 for area densities between 1.5 mg/cm^2 and 5.3 mg/cm^2. All scans show a similar shape. By increasing the RF amplitude the carpet is able to transport the ^{219}Rn ions to the nozzle and the alpha decay can be detected on the silicon detector in the diagnostics unit. An extraction efficiency of about 60% is reached in all measurements

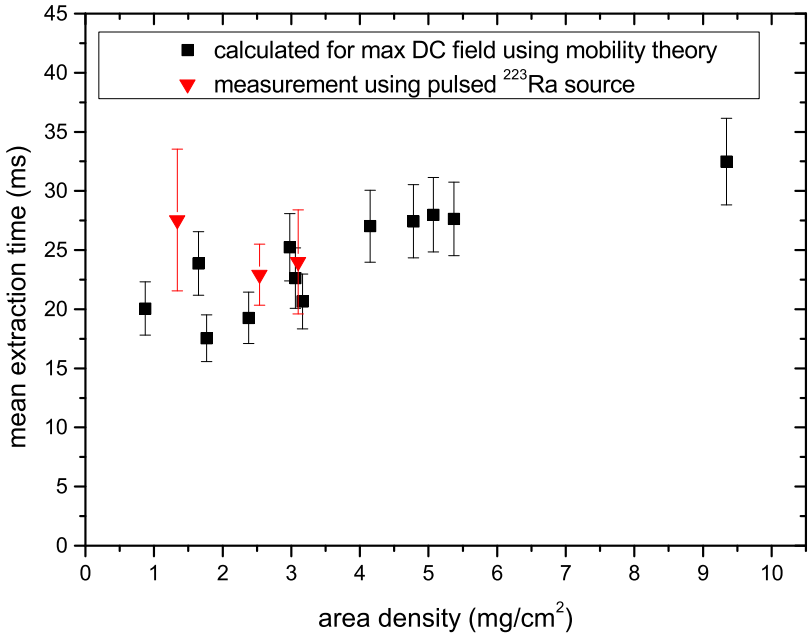

Figure 6.15: Extraction time measurements for different area densities of the CSC. Showing direct measurements and calculations based on mobility and the maximal achievable DC field along the body of the CSC.

at temperatures between 90 and 110 K. By fitting the measurement points of each series with a Boltzmann function the 50% or 90% transmission RF voltage can be found.

The behavior of the ions at the RF carpet was studied in detail and was used as operation check of the RF carpet. A reliable operation of the RF carpet is important for the operation of the full CSC. Without the RF carpet no ions can be extracted from the CSC and no experiments with exotic nuclei can be performed. Figure 6.17 shows the required RF amplitude for 90% transmission as a function of the area density of the cryogenic stopping cell for different RF carpet generations used at the FRS Ion Catcher. In addition to test measurements the ion motion was studied in ion optics simulation using the software packages SIMION [Sim88] and ITSIM [Pla01]. In figure 6.17 the results of the simulation are shown in addition with open black squares.

All measurements show a linear behavior between 2.5 mg/cm^2 and 6 mg/cm^2 area density between RF voltage and area density. At low area densities below 1 mg/cm^2 higher amplitudes are needed for extraction of ions from the CSC. This behavior is not described by eq. (3.69). This is due to the fact that at small number densities the ion velocity becomes larger than the maximal allowed ion velocity determined by the structure size and RF frequency of the RF carpet, eq. (3.73). In order to overcome this smaller structure sizes or higher RF frequencies have to be used. At area densities between 0.5 and 1 mg/cm^2 the ions can be stored further away from the surface of the RF carpet, which can be achieved by applying higher RF amplitudes.

The simulation describes the linear behavior at high area densities as well as the rapid

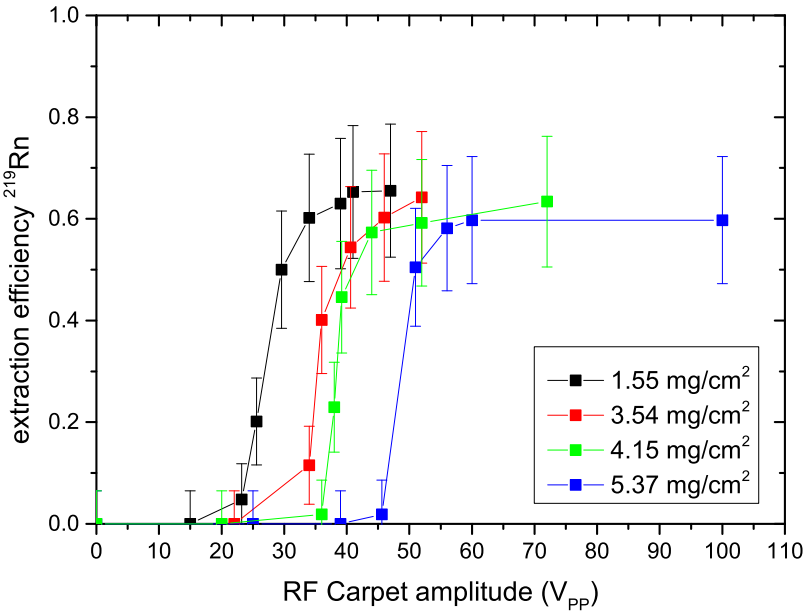

Figure 6.16: Measurement of the required RF amplitude at the RF Carpet for extraction of ^{219}Rn ions from the CSC at different areal densities of the CSC. Showing from which Rf amplitude on the carpet is able to transport ^{219}Rn ions trough the extraction nozzle towards the Si detector in the diagnostics unit.

increase in required RF voltage at low area densities below 1 mg/cm^2. The simulation is in good agreement with all measurements.

With such a good agreement between simulation and experiment the simulation can be used to predict the operation limit of the current RF carpet design. Currently the carpet can be operated with area densities up to $\sim$ 6 mg/cm^2 limited by the differential pumping and the pumping speed in the extraction region. The simulation shows that the current carpet design will be able to transport ions at area densities up to 16 mg/cm^2 when applying RF voltages of 150 V_{pp}. The simulation is done for a fixed DC gradient along the body of the stopping cell, which does not fully reflect how the stopping cell will be operated at such high area densities. In order to keep the extraction time short for experiments at high area densities the DC gradient will be scaled up, therefore equation (3.72) lo longer holds and the required RF amplitude scales with

$$P \propto V_{rf}^{1.5} \tag{6.1}$$

for increasing area density. The operation limit of the RF carpet, including scaling of the DC gradient, will be at an area density of about 11 mg/cm^2 He.

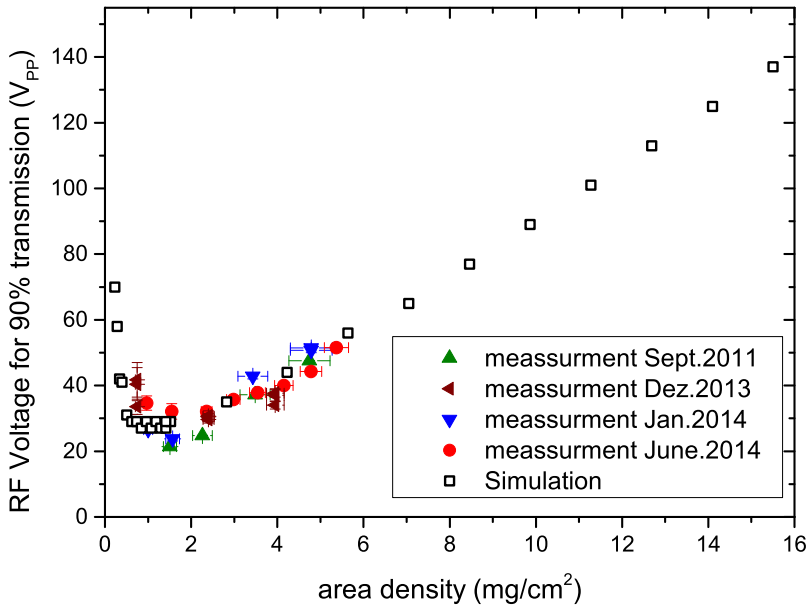

Figure 6.17: Measurement of the required RF amplitude at the RF Carpet for extraction of ^{219}Rn ions from the CSC at different areal densities in comparison to ion trajectories simulations. The required RF amplitude for extraction determined by simulation was done assuming fixed extraction DC fields of 20.0 V/cm.

6.5.2 Optimization of the inner layer for minimal RF power

During the 2012 experiment the inner layer of the RF carpet, shielding the ions pathways on the front side of the RF carpet from the electric fields produced by the electronic parts and cabling on the back side of the RF carpet, was grounded. As a result the RF carpet needed to be operated close to ground potential. This also defined the potential of the downstream RFQ beam line. In addition, if the RF carpet was operated at a different offset potential high RF amplitudes were required for extraction of ions from the stopping volume. In order to overcome this limitation the RF carpet was upgraded for the 2014 experiments.

This new electronic design of the RF carpet allows to operate the RF carpet at an arbitrary offset voltage. This was evaluated by RF scans for extraction of ^{219}Rn from the CSC for several voltage differences between the RF carpet and the inner layer. In figure 6.18 the required RF voltage for transmission is plotted as a function of the voltage difference between the inner layer and the RF carpet.

In the measurement an optimal field penetration between the layers is achieved for a voltage difference between the inner layer and the RF electrodes of -30 V, resulting in a minimal required RF voltage. The measurement also shows that if high voltage differences (< 100 V) are applied, almost a factor of two higher RF voltages are needed to extract ^{219}Rn ions from the CSC. This results also explain, why the RF carpet in the 2011 and 2012 experiments needed to be operated close to ground in order to extract ions with sufficient low RF powers. As a result the RF carpet can transport

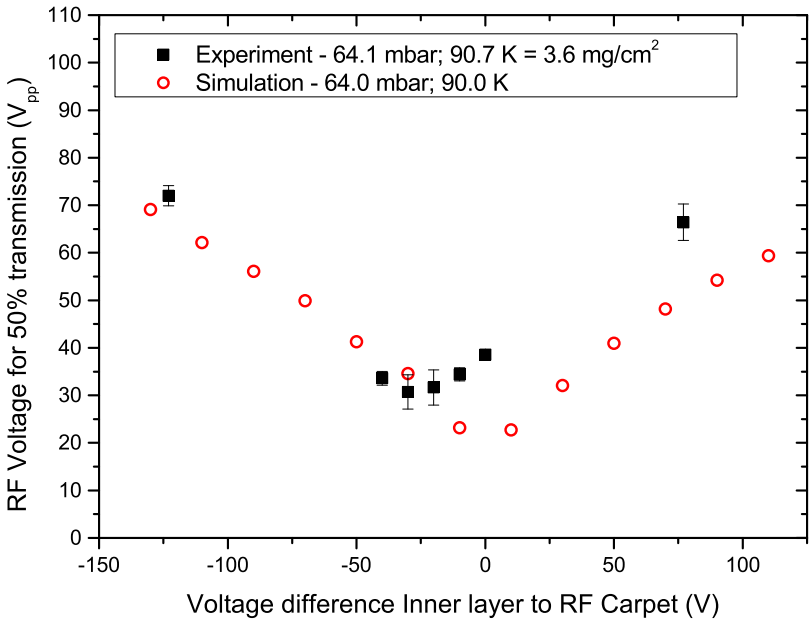

Figure 6.18: Required RF Amplitude at the RF Carpet for extraction of ^{219}Rn ions from the CSC for different voltages of the inner layer. Having the inner layer on a variable potential results in a non ground bound RF carpet. In addition the inner layer can be optimized and ion can be extracted from the stopping volume with a factor of two lower RF amplitudes. This translates into a maximal area density of about a factor of two higher compared to fixed inner layer.

ions at a factor two lower RF amplitude. This translates linearly into a factor of two higher operation pressure or at same area density into a factor of four less heat input into the cryogenic stopping cell.

This effect is well described by simulations. However, at positive voltage differences between the inner layer and the RF electrodes a systematic deviation can be seen in figure 6.18 and the simulation predicts a different optimal operation tuning for the RF carpet. The difference between simulation and the measurement is caused by the fact, that in the simulation no gas flow though the nozzle has been implemented. Thus ions which reach the vicinity of the nozzle are counted as 'extracted' and the ion motion along the RF carpet is considered only.

6.6 Usage of neon as a stopping gas

Stopping cells for relativistic heavy ions require high area densities in order to stop and thermalize secondary beams from fragment separators with high efficiency. The typical limitation of most stopping cells operating with projectile and fission fragments are their pumping speeds in the first differential pumping section or the maximal achievable pseudopotential at their RF structures for extraction of ions from the high

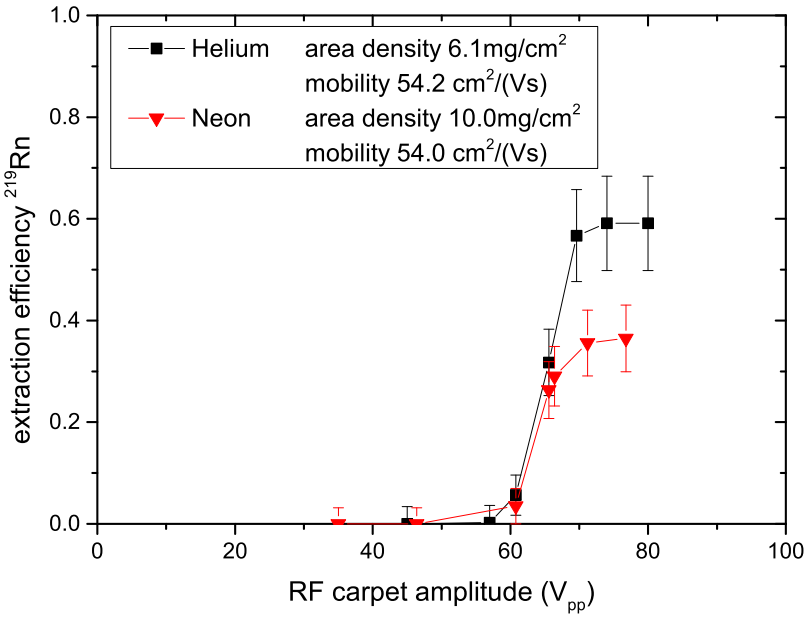

Figure 6.19: Measurement of the extraction efficiency as a function of applied RF amplitude at the RF Carpet for extraction of ^{219}Rn ions from the CSC for helium and for neon at different areal densities, but same mobility. Showing that at the same mobility the same Rf amplitude on the carpet is required to transport ^{219}Rn ions. Further a change in extraction efficiency depending on the stopping gas can be seen.

pressure region to the low pressure vacuum beam line. The limitation by differential pumping can be overcome by using additional differential pumping stages, so called multi-stage systems. A different approach is the usage of heavier stopping gasses.

For the FRS Ion Catcher these gasses should have high ionization potentials and a sufficiently high boiling point in order to be used in a cryogenic stopping cell. The noble gases He, Ne and Ar seem good choices for increasing the stopping power of a given stopping cell. Argon has a disadvantageous vapour pressure curve, because at e.g. 70 K a vapour pressure of only $10 - 100$ mbar is possible. In addition Ar is with its mass of 40 u above the low mass cutoff of the RF carpet. The ionization caused by high energy fragments being thermalized in the stopping cell would cause a huge Ar^+ current in the RFQ beam line. Therefore Ar can not be used at the CSC, which is based on the extraction of charged particles. In comparison Neon has a low boiling point of 27 K not limiting the lowest temperatures in the CSC. It also has the second highest ionization potential of 21.6 eV, therefore all other elements, except He, should not be able to do a charge exchange with Ne and by this remain as ions.

For these reasons neon was choose as a high mass stopping gas for the CSC. The advantage of Ne is its higher mass and much reduced mass flow through the extraction nozzle. Therefore with neon as a stopping gas the prototype CSC is no longer limited by differential pumping in the extraction region. The RF carpet can be tested at highest area densities and the predictions of the simulation can be checked under different conditions.

For the first test measurements using neon in the CSC an area density of 10 mg/cm^2 Ne was chooses with a purity of 5.0+. Similar to the test measurements with helium gas for ^{219}Rn ions the extraction efficiency was determined. Under similar cleanliness conditions an extraction efficiency of $(36 \pm 7)\%$ could be achieved for ^{219}Rn ions from the CSC, compared to $(59 \pm 9)\%$ at same tunings using helium as stopping gas. The relative drop in efficiency was already observed by [Den06] and could be reproduced in the efficiency measurements with the stopping cell. The drop in efficiency may be caused by the lower ionization potential of neon compared to helium or by a changed composition of the Ne gas compared to the ultra pure He gas. The effect is not fully understood. In figure 6.19 the corresponding RF scans for 10 mg/cm^2 Ne and 6.1 mg/cm^2 He are compared to each other. Both area densities match an ion mobility of $\sim$ 54 cm^2/Vs. Given that, from mobility theory and the description of the ion motion at the RF carpet in section 3.5.2 a comparable shape of the RF scan is expected.

The required RF voltage for extraction of ^{219}Rn ions from the CSC was studied over a broad range of area densities, ranging from 3.4 mg/cm^2 Ne up to 18.5 mg/cm^2 Ne. In figure 6.20 the needed RF voltage is shown for the different area densities at the CSC and for two different tunings of the CSC voltages. A maximal area density of 18.5 mg/cm^2 Ne was possible, the limiting factor at that area density is the power of the RF amplifier used for the generation of the RF voltage on the RF carpet. With the used RF amplifier only RF voltages up to 116 V_{pp} were possible. In the future the RF generation will be upgraded and allow for higher RF voltages.

6.6.1 Operation of the RF Carpet at smallest mobilities

Operation of the prototype CSC with Ne as a stopping gas allows a test of the RF carpet at high area densities, which are not possible due to the differential pumping with He as a stopping gas. A comparison of the achieved area density is shown in figure 6.20. The required RF amplitude at the RF carpet is plotted as a function of area density for He and Ne measured for similar conditions in the CSC. The measurement using helium gas allows a maximal area density of about 6 mg/cm^2 He, where as with neon gas area densities up to 18.5 mg/cm^2 Ne are possible.

In order to estimate the limitation arising from the maximal achievable pseudo potential at the RF carpet, the required RF amplitude for transmission can be plotted as a function of the mobility. The mobility can be calculated from equation (3.54). This is shown in figure 6.21. It can be seen, that when plotting as a function of mobility both He and Ne fit nicely together. Small mobilities correspond to high area densities. A minimal mobility of 29.2 cm^2/Vs was possible with Ne as stopping gas. This mobility corresponds to an area density of 11.3 mg/cm^2 when operating with He or to a stopping cell of 1 m operated at 660 mbar pressure at room temperature. Therefore the RF carpet used in the prototype CSC with a spacing of 4 electrodes per mm, will limited to 660 mbar room temperature operation, when applying $\sim$ 120 V_{pp} RF.

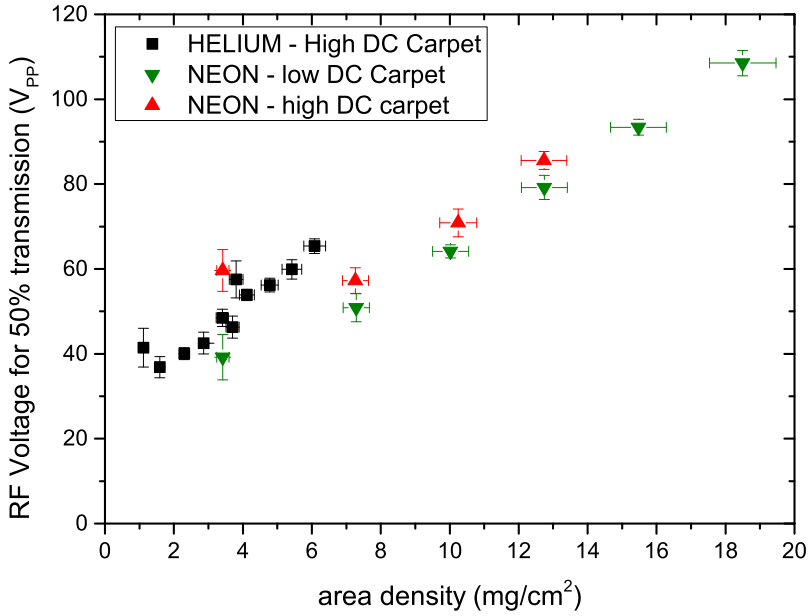

Figure 6.20: Required RF amplitude at the RF carpet for extraction of ^{219}Rn ions from the CSC as a function of area density. The carpet was able to transport ions at an areal density of 18 mg/cm^2 Neon.

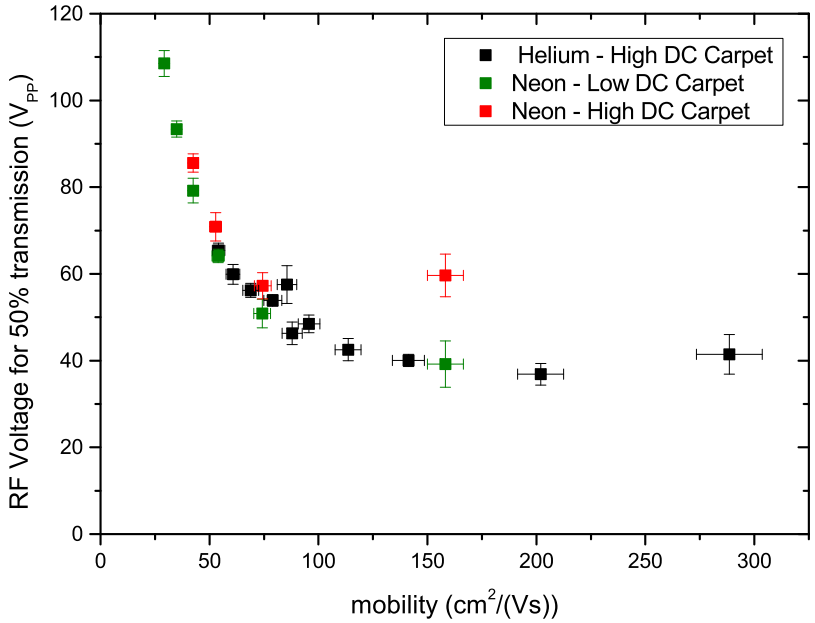

Figure 6.21: Required RF amplitude at the RF carpet for extraction of ^{219}Rn ions from the CSC as a function of mobility. From the measurement it can be concluded that the RF carpet scales with mobility.

6.6.2 Comparison of helium and neon as stopping gases

Using Ne as a stopping gas in the prototype CSC will allow higher area densities and therefore also higher stopping efficiencies. Comparing the achievable area density for He with Ne is not a hundred percent correct, because when operating a stopping cell not its area density but its stopping power has to be taken into account. The stopping power of the CSC is shown as a function of area density in figure 6.22. Because of the reduced electron density for Ne compared to He, at same area densities a reduced stopping power is achieved. This means for a stopping power of 3.2 MeV/u for a ^{223}Th beam an area density of ~ 6 mg/cm^2 He are sufficient, or ~ 9.5 mg/cm^2 Ne.

Comparing the achievable maximal stopping power of the CSC for stopping of a ^{223}Th beam of 7.7 MeV/u when running with Ne, where as only 3 MeV/u when operated with He gas. If the CSC would not be limited by the differential pumping a maximal stopping power of 7 MeV/u should be possible with He gas from the RF carpet point of view. Reaching even higher stopping powers and area densities requires the usage of smaller structure sizes at the RF carpet.

A major disadvantage of Ne is the different Paschen curve and therefore only lower DC potentials can be applied to the electrodes of the DC cage. The resulting lower DC fields along the body of the CSC prolong the extraction time of ions from the CSC. The mean extraction time extends from 25 ms for He to 160 ms for Ne. Thus operating the CSC with Ne limits its access to exotic nuclei with half lifes in the order of hundred of ms. As a comparison the mean extraction time resulting from actual voltage measurements is shown as a function of area density in figure 6.23. In combination with the reduced ion survival efficiency determined for Ne compared to He, using Ne gas seems a niche operation mode for stopping cells. There are cases of long lived exotic nuclei where the increased stopping efficiency will be beneficial. For the study of exotic nuclei far from stability, which reach half lives down to a few ms, it will not be worth operating the CSC with Ne gas. Also the increased cost of Ne gas compared to He gas have to be considered.

However, in the case of performing experiments on nuclides produced by in-flight fission the increased stopping power will give a factor of 1.5 higher count rate for exotic nuclei for low energy experiments downstream of the stopping cell. In addition the factor of 2.5 lager area thickness of the stopping cells allows the stopping of different isotopes at the same time. This allows e.g. to stop an ion species of interest at the same time with a possible calibrant or in the case of isotope or isomer search experiments the stopping point can be scanned with a broader step size, allowing more efficient use of beam time.

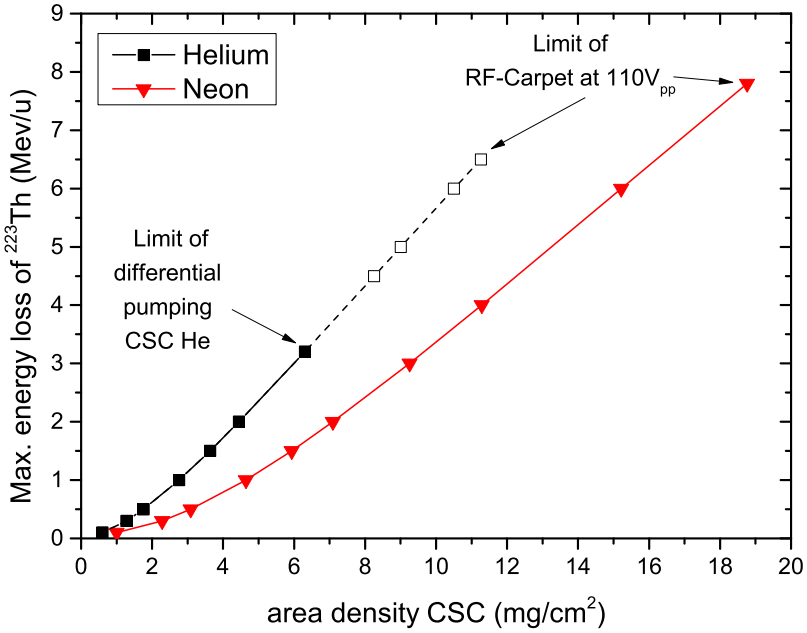

Figure 6.22: Calculation of the energy loss of ^{223}Th ions in the CSC filled with different gasses as a function of the area density. For He a maximal energy loss of 3.2 MeV/u is possible, limited by the differential pumping. With increased pumping power the current RF carpet should be able to work up to a maximal energy loss of 7 MeV/u. Where as with Ne 7.7 MeV/u energy loss is possible.

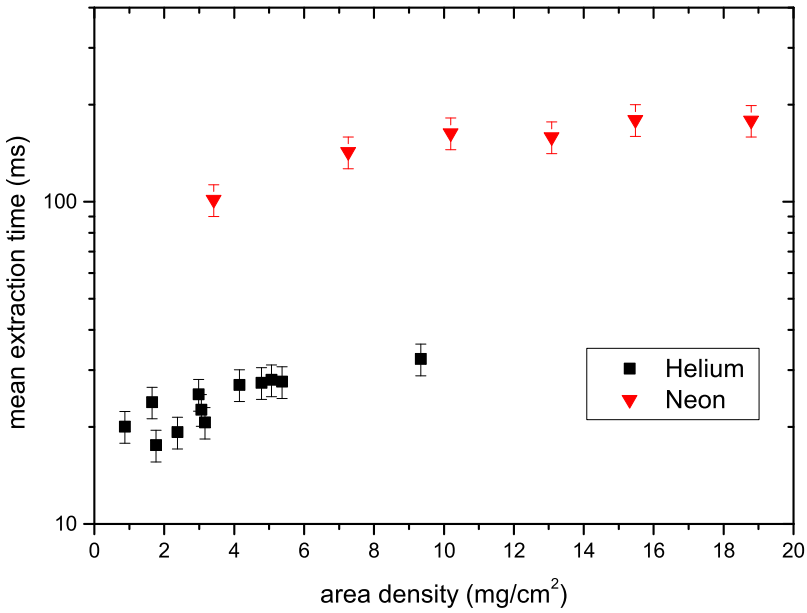

Figure 6.23: Extraction time as a function of different area density of the CSC. The extraction time was calculated from the measured maximal achievable DC field along the cryogenic stopping cell for Helium and Neon as a stopping gas. Using Neon results in a longer extraction time by about a factor ~ 6.

7 Experiments with ^{238}U projectile and fission fragments in a cryogenic stopping cell at the FRS Ion Catcher

The cryogenic stopping cell as part of the FRS Ion Catcher was commissioned in three test experiments in 2011, 2012 and 2014 at GSI. The goal was to investigate the performance of the CSC under experimental conditions similar to those at the future low energy branch. In detail the extraction efficiency of ions produced by in flight fragmentation, the extraction time and the cleanliness of the CSC were investigated. Additionally the CSC was used to enable high-precision low-energy experiments with thermalized exotic nuclei. Major parts of this chapter have been published in an earlier publication [Pur13] especially the results obtained during the 2011 and 2012 FRS Ion Catcher [Pla13a] experiments. The experiment in 2011 will be referred to as Exp.I, 2012 as Exp.II and 2014 as Exp.III.

Ions were extracted from the heavy-ion synchrotron SIS-18 as ion bunches with a length of 2 to 6 s and steered on a production target at the entrance of the fragment separator FRS. Heavy α-decaying nuclides in the element region above lead were produced by projectile fragmentation of a ^{238}U primary beam at an energy of 1000 MeV/u in a Be target with an areal density of 1.624 g/cm^2 followed by a 0.223 g/cm^2 Nb stripper foil. A 4.2 g/cm^2 monoenergetic degrader at the central focal plane was used for separation and energy-bunching of the fragments. Intermediate mass, neutron rich nuclides around to the N=82 shell closure were produced by in-flight fission of ^{238}U primary beam on a 6.333 g/cm^2 Be target and 0.223 g/cm^2 Nb stripper foil.

Spatial separation of the fragments was performed by two-fold magnetic rigidity analysis in front and behind of a monoenergetic degrader positioned at the central focal plane of the fragment separator. Position-sensitive detectors (TPC) [Jan11] and time-of-flight detectors (SCI) combined with two multiple sampling ionization chambers (MUSIC) [Pfu94] provided particle identification for each ion transported through the FRS to the achromatic final focal plane. Together with the selected magnetic fields, the position detectors provide the Bρ values for each particle. The velocity and the charge of each particle have been measured by the SCIs and MUSICs, respectively. During transport through the FRS most of the ions are fully ionized, thus the first MUSIC can provide an element identification. The last MUSIC was used for optimizing the thickness of the homogeneous degrader. For the case of α emitting nuclei, a

verification of the particle identification could be performed with a position-sensitive silicon detector (alpha-tagger), into which the selected fragments are implanted to observe the known alpha decay [Pur13].

The homogeneous degrader of variable thickness (VH-Degrader), placed in between the MUSIC detectors, was used to adjust the energy of the selected fragments such that they are stopped in the second MUSIC or the CSC [Pur13]. The range distribution of the selected fragments is primarily determined by the initial mean energy and the energy straggling. The fragments transmitted through the FRS can have a maximum momentum spread of $\pm 1\%$ which is defined by the size of the magnet and the apertures. The resulting momentum spread would be to large and therefore not allow an efficient stopping in the cryogenic gas-filled stopping cell. Therefore the high ion-optical resolution at the central focal plane and a precision monoenergetic degrader were used in combination to compress the resulting atomic range straggling [Pur13].

7.1 In-flight identification at the FRS

The exotic nuclei were identified in the second half of the fragment separator between S2 and S4 and by the use of equation (3.17). For each particle its $B\rho$ was calculated from the magnetic field and by a set of two TPCs at the S2 and S4 focus. The set of two TPC's allows assigning of the position and angle of each particle, which is applied for the calculation of the effective radius ρ of a particle in the magnetic field.

The velocity was measured via time-of-flight between the SCI at S2 and at S4 with a flight path of ~ 37 m. The SCI have photomultiplier tubes on both sides, measuring the light emitted by the interaction of a single particle with the scintillating material on both sides of the SCI. This enables a correction of the time-of-flight according to the position of the particle. For calibration of the time-of-flight ^{238}U primary beam of different energies was used. For example during the 2012 experiment two energies were requested from the SIS-18 (1000 MeV/u and 600 MeV/u) and two target thicknesses were used (5500 mg/cm^2 and 4200 mg/cm^2), corresponding to four calibration points with velocities between a β of 0.77 and 0.87. A magnification of 1.115 and a dispersion of 7.220 m for the second stage of the FRS from S2 to S4 was derived from optics calculations [Pur13].

The MUSIC is determining the charge of a fragment by the energy deposition in the chamber. The energy deposition (dE) scales with $\sim Z^2$ (see ch. 3.4). Using ^{238}U primary beam the peaks in the dE-spectra can be assigned to the different charge states, counting down individual peaks starting from $Z = 92$. The dE is velocity dependent and therefore needs to be calibrated for different beam energies. In addition the MUSIC identification is position sensitive; on the sides of the detector a reduced dE is measured, because of a non perfect field cage. A sixth order polynomial is used for the position correction.

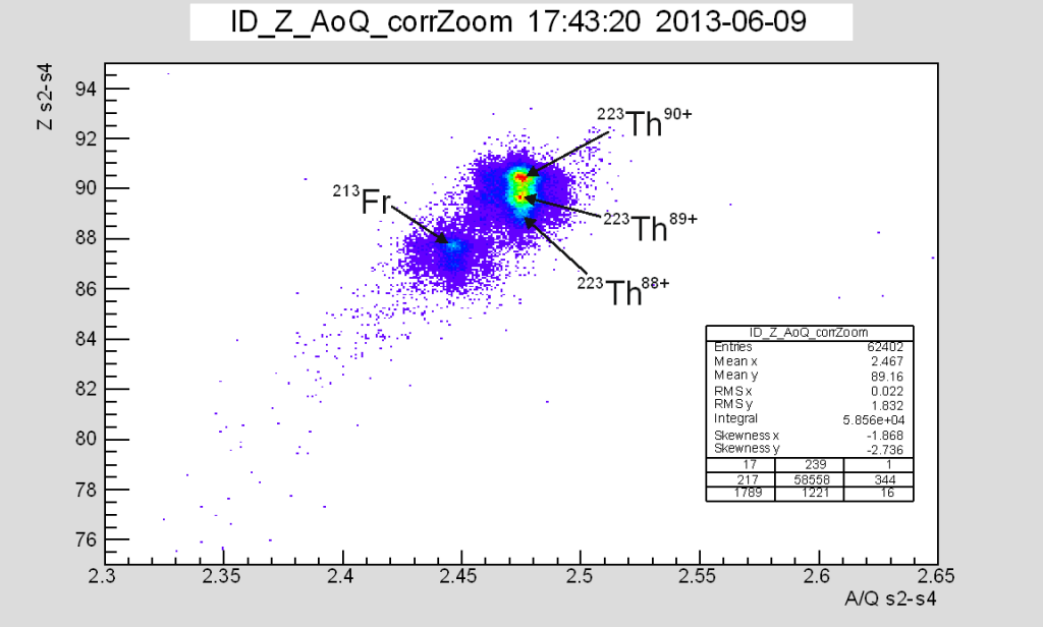

Figure 7.1: FRS identification plot of ^{223}Th produced by in flight fragmentation of ^{238}U at 1000 MeV/u, showing the mass-over-charge (A/Q) measured by the motion in the magnetic field and the charge state measured by the ionization chambers.

The determination of the Z values requires attention due to charge-changing collisions in the exit vacuum window of the FRS and the subsequent material in front of the first MUSIC. The energy deposition in a MUSIC is governed by the ionic charge, and since the fragments are already slowed down to energies of 490 MeV/u, the H-like ions (about 40 %) and He-like (about 5 %) have to be included in the intensity determination. In this way the number of ions of a selected fragment was measured up to the entrance of the homogeneous variable VH-Degrader [Pur13].

In an identification (ID) plot typically the calibrated A/Q measured by the trajectories in the magnetic field is plotted versus the charge measured by the MUSIC, which is the nuclear charge Z of the fragments at this energies. In figure 7.1 at typical ID plot of ^{223}Th can be seen, identified at the FRS.

7.1.1 Range distribution measured in the MUSIC

The thickness of homogenous variable degrader was varied until the selected fragment was stopped in the second MUSIC. Experimentally this can be seen by the appearance of the Bragg peak. In the case of stopping in the CSC, the kinetic energy in the second MUSIC is about 100 MeV/u and although single charge states can no longer be resolved at the strongly reduced energy, the amount of ions passing through the VH degrader can be measured. The value was found to be about 70 ± 2 % and is in excellent agreement with transmission and absorption calculations with the Monte Carlo simulation program MOCADI [Iwa97, Iwa11].

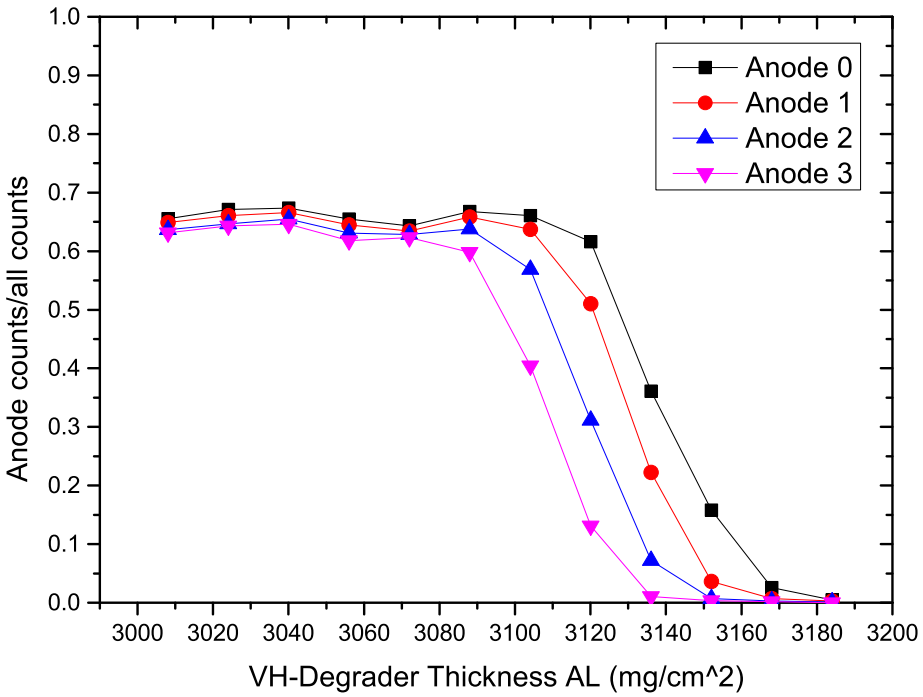

Figure 7.2: Measuring the range distribution of ^{223}Th in the second MUSIC by varying the VH-degrader in front of the MSUIC 3 and the CSC. The measurement was performed during the 2014 experiments.

The result of the so called 'range scan' is shown in figure 7.2 for ^{223}Th ions. The signal on the different anodes of the last MUSIC can be seen as a function of the thickness of the VH degrader. The measurement was performed with the slit settings at $S1 = \pm 10$, $S2 = \pm 15$ and $S3 = \pm 30$. Fitting the slope with an error function allows determination of the width and the mean of the range distribution. The resulting values are given in table 7.1. With this procedure experimentally the starting thickness was found to perform the corresponding range scan for the ions of interest stopped in the cryogenic stopping cell.

Music Anode	R (mg/cm^2)	σ_R (mg/cm^2)
1	3140.7 ± 1.5	14.8 ± 2.0
2	3130.4 ± 0.6	13.3 ± 0.6
3	3119.7 ± 0.5	13.0 ± 0.6
4	3108.8 ± 0.5	13.4 ± 0.6

Table 7.1: Mean range R and width of the range distribution σ_R measured in the MUSIC behind the homogenous variable degrader for the projectile fragment ^{223}Th.

7.1.2 Range distribution measured in the CSC

The correct tuning of the VH-degrader for stopping of ^{223}Th ions in the stopping cell was estimated with the knowledge of the additional material between the second MUSIC and the cryogenic stopping cell. The range has to be adjusted for three stainless steel beam windows. Thus ions can be implanted into the stopping volume of the cryogenic stopping cell and can be extracted.

The ions of interest were extracted from the CSC and transported to the Si detector in the DU. Identification was done by the characteristic α decay energies of the exotic nuclei. The number of extracted ions of the nuclide of interest was determined from the number of decay events, taking into account the solid angle of the active area of the Si detector with respect to the collection aluminum foil. A correction due to non-pointlike distribution of the ions on the foil of 0.994 ± 0.005 were introduced [Gar80], correspond to homogenous spot size on the foil with a diameter between 1 and 2 mm.

The scans of the range distribution for ^{223}Th ions are shown in figure 7.3 for the three experiments. The range distribution determined for the Exp.I in 2011 and Exp.II in 2012 are given on the top. The range distributions measured during the 2014 experiment are given for two area densities (Exp.IIIa and Exp.IIIb) of the stopping cell at two different tunings of the slits of the FRS. All range distributions can be well described with a Gaussian function. The measured range distribution are given in thickness units of the aluminum degrader. With this measurement the energies of the ions stopped in the helium gas are determined and one can convert the areal density of the gas into the aluminum range distribution - see hatched area in figure 7.3.

In comparison the range distribution of a monoenergetic beam is shown for the four cases (red line) in figure 7.3. It can be seen that in 2011 and 2012 the range distribution was closer to the monoenergetic limit compared to in the 2014 experiment. The phase space of the relativistic ion beam strongly depends on the tuning of the slits at the FRS, because opened slits result in a larger energy spread in front of the monoenergetic degrader and thus also afterwards. In addition larger slits allow transport of a beam with bigger diameter and therefore the ions probe increased inhomogeneities while traversing through the material on their flight path. During the 2014 experiment the slits have been opened in order to enhance the transmission and to reach higher secondary beam yields, in addition the monoenergetic degrader was not optimized and only set from optics calculations, because of the limited beam time available, thus resulting in a larger range distribution. The effect of changing the slits can be seen partly in the increased range distribution between the Exp.IIIa and Exp.IIIb range scans. The tuning of the slits at the FRS is given for the different range scans in table 7.2. After deconvolution from the areal thickness of the stopping cell, the one standard deviation of the range distributions can be calculated. The results are listed in table 7.3.

In addition during the 2014 experiment the MR-TOF-MS was used for an optimization

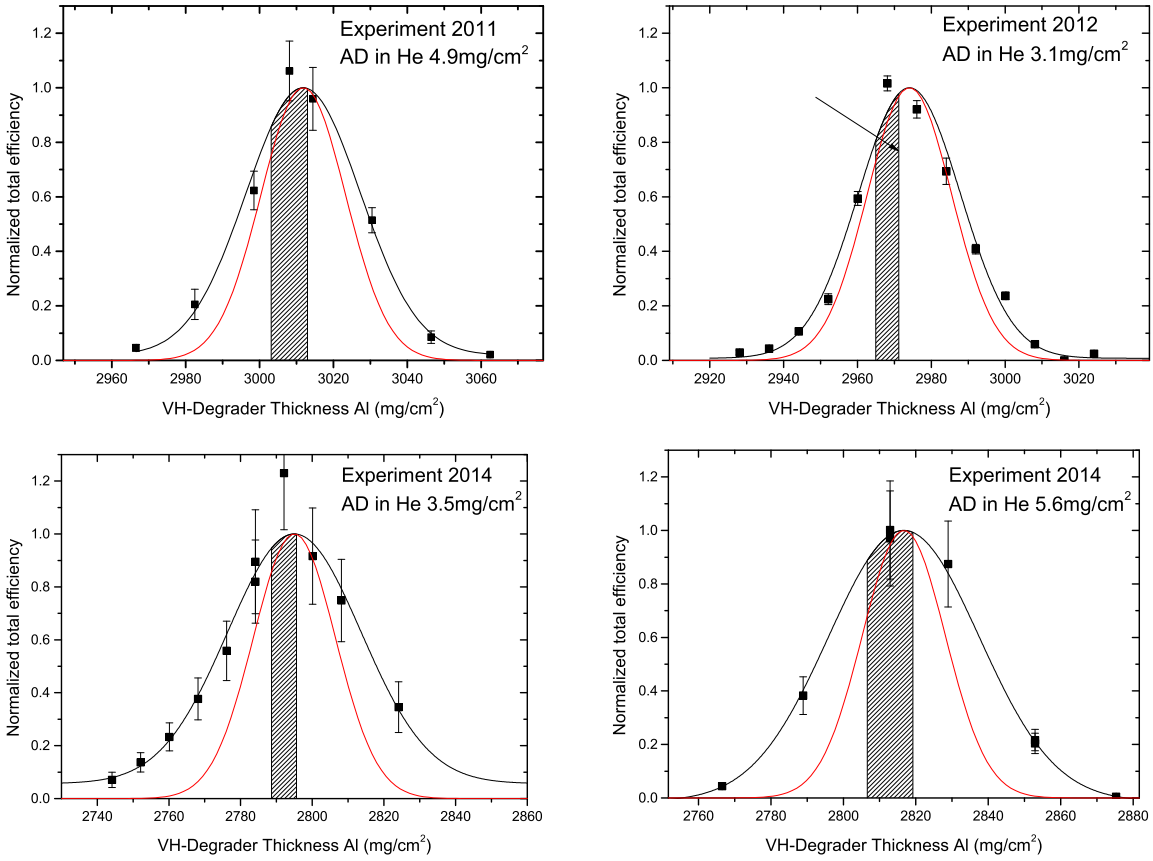

Figure 7.3: Range distribution of ^{223}Th ions in the cryogenic stopping cell during the different experiments. The black solid curve shows a Gaussian fit to the normalized total efficiency. The hatched region indicates the areal density covered by the stopping cell. In red the expected range distribution of a monoenergetic beam is shown with straggling in the VH degrader.

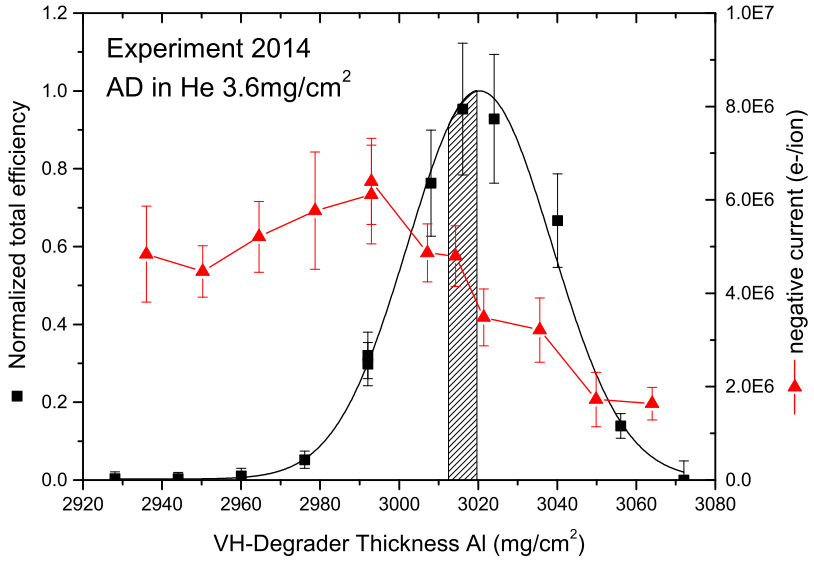

Figure 7.4: Measuring the range distribution of ^{213}Fr during the 2014 experiment, while simultaneously measuring the negative e^- current at the entrance window of the CSC.

of the range of ^{213}Fr produced via projectile fragmentation. High resolution mass spectrometry allowed a clear identification of the fragment and by tuning of the VH-degrader the optimal stopping position for ^{213}Fr ions in the cryogenic stopping cell was found, see figure 7.4. In parallel the electron current, caused by the ionization of the helium stopping gas by the beam particles, on the entrance window of the DC cage was monitored. Measuring the electron current permits a determination of the center of the range distribution without the usage of any downstream detector system, which was validated by the parallel measurement. It needs to be mentioned that this method only allows determination of the average range distribution of the cocktail beam delivered by the FRS to the stopping cell. This technique could be used to estimate the average amount of ionization caused by the stopping of the relativistic beam particles in the stopping cell. It amounts to $\sim 5 \cdot 10^6$ He-e$^-$-pairs per incoming ion **??**.

Slits	Exp. I (mm)	Exp. II (mm)	Exp.IIIa (mm)	Exp.IIIb (mm)
S1	±10	±5	±10	±2
S2	±10	±10	±15	±30
S3	open	open	±30	open
S4	-9 $+11$	±10	±20	±25

Table 7.2: Tuning of the slits at the FRS for the different range scans for the projectile fragment ^{223}Th.

Using the MR-TOF-MS for the optimization of the stopping has the advantage that the identification does not rely on the decay properties of the ion of interest and is therefore element independent. Secondary the identification by mass spectrometry can also be used for stable particles e.g. using primary beam.

7.1.3 Determination of the stopping efficiency

The stopping efficiency ϵ_{stop} is given by the ratio of the integral of the section of the range distribution corresponding to the areal density covered by the CSC to the integral over the full range distribution. The areal density of the CSC is determined by the measured temperature and pressure of the stopping gas, and the length of the stopping volume.

$$E_{stopping} = \frac{\int_{-AD_{Al}/2}^{AD_{Al}/2} \frac{A}{\sigma\sqrt{2\pi}} e^{\frac{-x^2}{2\sigma^2}}}{\int_{-\infty}^{\infty} \frac{A}{\sigma\sqrt{2\pi}} e^{\frac{-x^2}{2\sigma^2}}} \tag{7.1}$$

The degrader material is Al and the stopping cell is He. Thus the areal density (AD_{He}) of the stopping cell in He needs to be converted into an effective areal density in Al (AD_{Al}) for calculation of stopping efficiency. The conversion factor from Al to He amounts to 2.0 ± 0.1 taking the conditions of the experiments into account,

i.e. the different energy in the VH-Degrader and the helium stopping gas, the subsequent material placed in between the VH-Degrader and the He stopping gas [Pur13]. The conversion factor from Al to He was evaluated by a MOCADI simulation of the experiment. The resulting stopping efficiencies are listed in table 7.3.

7.2 Extraction efficiency for different isotopes from the CSC

For the optimum degrader thickness the total efficiency of the CSC for a selected nuclide ϵ_{total} was determined as the ratio of the number of extracted ions of this nuclide to the number of ions of this nuclide entering the CSC. The number of ions of interest was determined from a FRS ID plot and additional corrections were applied taking into account the dead time of the in-flight data acquisition system, misidentification of particles where the signals of the different in-flight detectors could not be collated to a single ion and fragmentation losses in the VH-degrader. For short-lived nuclides decay losses have been taken into account.

The combined ion survival and extraction efficiency is given by the ratio of the total efficiency to the stopping efficiency

$$\epsilon_{sur+ext} = \epsilon_{\text{total}}/\epsilon_{\text{stop}}. \tag{7.2}$$

It reflects ion losses due to neutralization during the slowing-down and thermalization processes in the CSC as well as losses due to collisions of the ions with the electrodes of the CSC during the transport and extraction. The ϵ_{stop} values were only measured for ^{223}Th and ^{213}Fr ions, however, the corresponding values for ^{221}Ac, ^{219}Rn, ^{218}Rn, ^{220}Ra and ^{211}Po ions are within the given experimental uncertainties.

The final results of the three experiments performed at the FRS-Ion-Catcher for the six nuclides under different conditions are summarized in table 7.3. These measurements were performed at low beam intensities of a few hundred ions per second, such that intensity-related efficiency limitations due to space charge and plasma effects in the stopping volume can be ignored [Huy02, Tak05, Moo08, Rei15]. In order to enable a comparison of extraction efficiencies for different elements, the values have been corrected for the lifetime of the ions and the specific extraction time of ions from the CSC. The extraction time was calculated from mobility for the individual experimental conditions. However, for the nuclides ^{223}Th and ^{219}Rn this correction is negligible.

A better comparison of the ion survival and extraction efficiencies ($\epsilon_{\text{sur+ext}}$) can be seen in figure 7.5 for the different experiments and for 3 different analysis. In order to reduce systematic errors all intermediate steps of the data evaluation were performed by two people using different detectors for the identification. The alpha spectra were fitted by OriginPro9 and by IGOR Pro (Sivaji Purushothaman). The in-flight identification of the 2011 and 2012 experiment was additionally checked using a different data

analysis approaches relying on relative abundance of the ions of interest compared to all ions in the in-flight identification (data analysis 2, Emma Haettner). The data analysis of the 2014 experiment was validated by comparing the results to an analysis based on an additionally MUSIC detector, which was positioned in 2014 behind the first MUSIC (data analysis 3, Lisa Schlüter). Deviations in the different analysis, were found to be within the statistical uncertainties.

	Exp. I	Exp. II	Exp.IIIa	Exp.IIIb	Exp.IIIc
p (mbar)	98 ± 5	47 ± 2	64 ± 3	95 ± 5	106 ± 5
T (K)	100 ± 2	78 ± 2	93 ± 2	87 ± 2	86 ± 2
AD in He (mg/cm^2)	4.9 ± 0.3	3.1 ± 0.2	3.5 ± 0.2	5.6 ± 0.3	6.3 ± 0.3
^{223}Th					
σ_R in Al (mg/cm^2)	15.4 ± 0.9	13.7 ± 0.8	17.0 ± 1.5	20.6 ± 0.7	20.6 ± 0.7
ϵ_{stop} (%)	27.0 ± 2.4	15.9 ± 1.8	16.3 ± 1.8	21.0 ± 2.4	23.8 ± 2.7
ϵ_{total} (%)	11.6 ± 1.6	9.9 ± 1.5	13.3 ± 2.2	21.9 ± 3.9	20.3 ± 3.6
$\epsilon_{\text{sur+ext}}$ (%)	43 ± 7	62 ± 12	82 ± 15	95 ± 20	85 ± 20
^{221}Ac					
ϵ_{total} (%)		7.7 ± 1.6			
$\epsilon_{\text{sur+ext}}$ (%)		48 ± 11			
^{220}Ra					
ϵ_{total} (%)			9.1 ± 5.3		
$\epsilon_{\text{sur+ext}}$ (%)			56 ± 18		
^{219}Rn					
ϵ_{total} (%)	14.5 ± 2.0				
$\epsilon_{\text{sur+ext}}$ (%)	54 ± 9				
^{218}Rn					
ϵ_{total} (%)		5.2 ± 1.6			
$\epsilon_{\text{sur+ext}}$ (%)		29 ± 10			
^{211}Po					
ϵ_{total} (%)				20.2 ± 3.9	
$\epsilon_{\text{sur+ext}}$ (%)				78 ± 16	

Table 7.3: Pressures (p), temperatures (T), and areal densities (AD) of the stopping gas during the efficiency measurements, as well as standard deviations of the range distribution (σ_R) in units of the Al degrader, total efficiencies (ϵ_{total}) corrected for decay losses, stopping efficiencies (ϵ_{stop}), and combined ion survival and extraction efficiencies ($\epsilon_{\text{sur+ext}}$) measured in the three experiments.

A reduced ion survival and extraction efficiency for the short lived isotopes (^{221}Ac $\sim$ 52 ms, ^{218}Rn $\sim$ 35 ms, ^{220}Ra $\sim$ 18 ms) can be observed relative to ^{223}Th. Therefore the dependence of the efficiencies corrected for the decays, on the half life was investigated, which allows a validation of the half life correction of the short lived isotopes. Within the error bars no systematic effect was found.

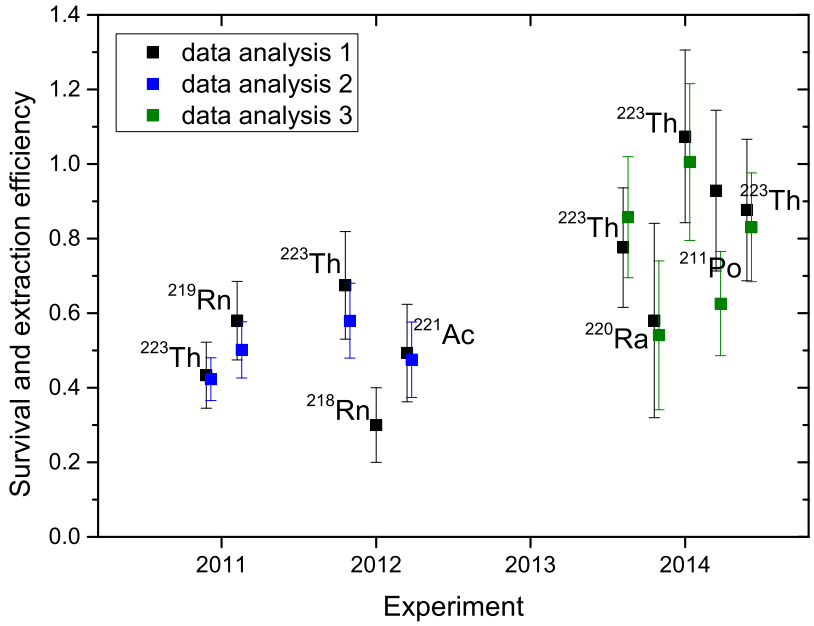

Figure 7.5: Survival and extraction efficiency for different projectile fragments as measured during the three experiments. The enhanced cleanliness of the CSC results in an increased survival and extraction efficiency

The mean survival and extraction efficiency for the 2011 and 2012 experiments amounts to $(47 \pm 8)\%$, for the 2014 experiment to $(79.5 \pm 14)\%$. The increase in survival and extraction efficiency is a result of the effort put into increasing the cleanliness of the cryogenic stopping cell and in particular the stopping gas, e.g for the 2012 experiment an purification getter was added to the helium feeding line, for the 2014 experiment the cryogenic stopping cell was baked at 420 K before the cool-down was started, more details are described in chapter 5.2.

7.2.1 Cleanliness of the CSC

The cleanliness of a stopping cell and of the extracted low energy ion beam is of great importance for all high precision measurement. Only an ultra pure system allows the extraction of the ion of interest as bare ions, without adducts, and in higher charge states. In addition only if pure beams, consisting dominantly of the ion of interest, can be be extracted from the stopping cell a clear identification and background free measurements are possible.

The cleanliness of the CSC was investigated using the MR-TOF-MS in a broadband mode. Broadband mass spectra of ions extracted from the stopping cell were acquired under different conditions. Figure 7.6 shows the mass spectrum of extracted ions while ^{218}Rn was injected into the CSC during the 2012 experiment. The mass lines in the spectrum correspond to ^{218}Rn ($T_{1/2} = 35$ ms) and its decay product, ^{210}Pb, as well as ^{219}Rn ions from the internal ^{223}Ra recoil source in the CSC and its decay products, see insert. The ratio of the number of ions originating from the beam N_{beam} injected

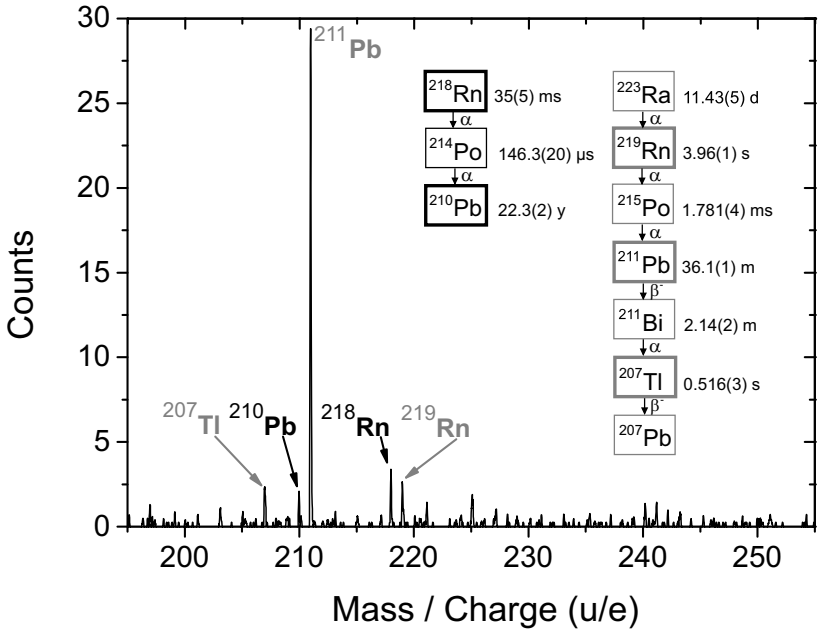

Figure 7.6: Mass spectrum of ions extracted from the CSC during injection of ^{218}Rn ions using the MR-TOF-MS in broadband mode measured during the 2012 experiment, [Pur13].

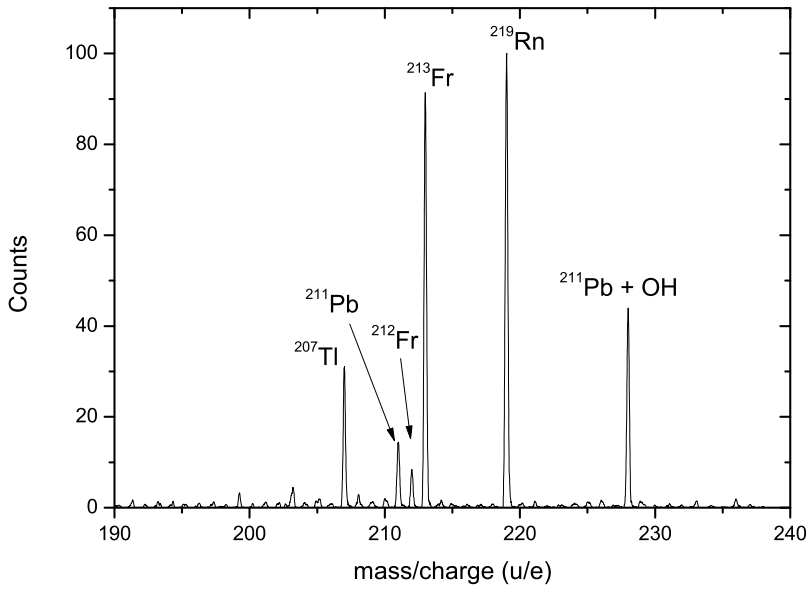

Figure 7.7: Mass spectrum of ^{213}Fr ions extracted from the CSC determined during the 2014 FRS Ion Catcher experiment. The labeled mass lines originate from the beam and from the ^{223}Ra recoil source in the CSC.

into the CSC to the number of contaminant ions $N_{\text{cont.}}$ produced in the CSC, e.g., by charge exchange or chemical reactions amounts to about 0.6 for the mass window shown in figure 7.6. In the mass spectra shown in the figure 7.7 ^{213}Fr and ^{212}Fr from the FRS have been injected into the CSC during the 2014 experimental run. The ratio of ions from the beam to contaminants results to 2.2, in this calculation the mass line corresponding to ^{211}Pb+OH was counted as back ground. At each mass line a average contamination background of 1.2 counts can be seen. Therefore a signal to noise ratio for ^{213}Fr of $\sim$ 70 to 1 is measured. The results are summarized in table 7.4.

Experiment	Ion of interest	$N_{\text{beam}}/N_{\text{cont.}}$	Signal to noise
Exp.II	^{218}Rn	0.6	5 to 1
Exp.IIIa	^{213}Fr	2.2	70 to 1

Table 7.4: Measured ratio of the number of ions originating from the beam N_{beam} to the number of contaminant ions $N_{\text{cont.}}$ and the resulting signal to noise ratio for the 2012 and 2014 experiment.

Clearly, the CSC features such a good cleanliness that contaminant ions are not a major problem, shown by the cleanliness of the mass spectra of the extracted ions. The improved cleanliness results in a significant improved signal to noise ratio for the 2014 experiment.

7.2.2 Extraction in different charge states

A different approach to test the cleanliness of the CSC is to investigate the charge state ions are extracted.

Operating the extraction RFQ as a mass-filter allows a quick determination of the charge state [Mis15]. This technique was used during the 2014 experiment to measure the charge state of ^{220}Ra, ^{223}Th and ^{238}U ions thermalized and extracted from the CSC. The mass filter was tuned to different mass-over-charge settings measuring the characteristic alpha decays e.g. of ^{220}Ra with the Si detector in the diagnostics unit. The mass-over-charge distribution of the detected alpha decays in shown in figure 7.8 for the case of ^{220}Ra. The spectrum was normalized to the total observed activity. This shows that about $\sim$ 80% of the ^{220}Ra ions are extracted in a 2+ charge state and $\sim$ 20% as single charged ions. A 3+ charge state was not observed. For ^{238}U ions extracted from the cryogenic stopping cell the mass filter was used in combination with the channeltron detector. More than 90% of the uranium ions were extracted from the cryogenic stopping cell as 2+ ions [Mis15].

This may be explained by two different phenomena. First, relativistic ions pass through various charge states during their slow down and stopping processes in the solid degrader as well as in the buffer gas of the CSC. They start mainly as fully

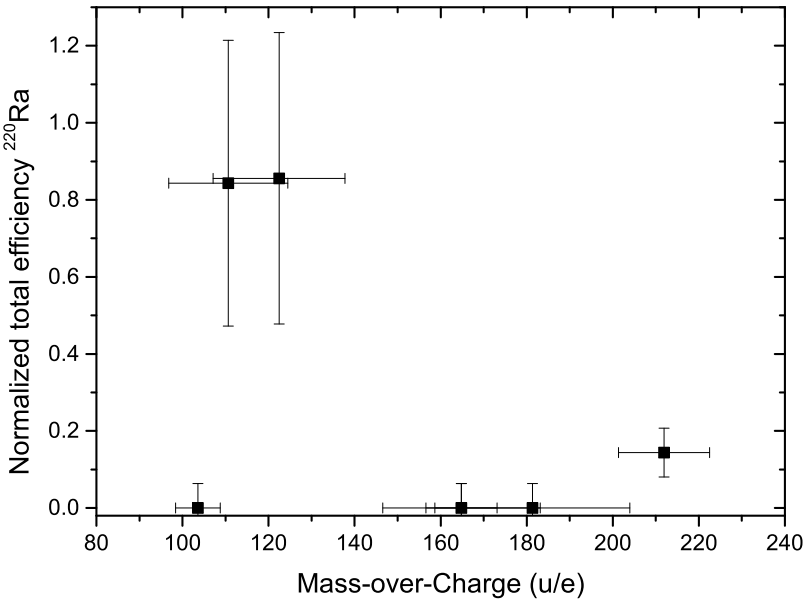

Figure 7.8: Using the extraction RFQ as a mass filter, determining the charge state of ^{220}Ra extracted from the CSC. It shows that $\sim$ 80 % of the ^{220}Ra ions are extracted in a 2^+ charge state.

ionized particles at high energies and end up with a certain charge state distribution of 1+, 2+ or 3+ etc. at rest. Therefore different charge states are expected. Secondly, ions stopped in a higher charge state can perform a charge transfer reaction during their extraction from the buffer gas volume. In this case the ionization potential of the collision partner is defining the probability for the charge transfer reaction. If the collision occurs between an ion of interest with a residual gas atom with a lower ionization potential the probability for a charge transfer reaction is enhanced compared to a collision with a residual gas atom with a much higher ionization potential. Therefore in collisions with helium, which has the highest first ionization potential of 24.6 eV, typically no charge transfer occurs and the ion of interest stays in a 2+ or 3+ charge state.

The cryogenic stopping cell uses ultra pure helium as stopping gas, but still impurities such as O_2, N_2O, OH, CO_2, N are present in the system. These impurities lower the expected charge states an ion of interest is expected to be extracted in, see section 6.3. In figure 7.9 the ionization energy of the buffer gas atoms is shown in comparison to the charge states of the ions of interests. It is indicated which charge states have been obverse as a function of the ionization potential. It can be seen that ions are not extracted from the cryogenic stopping cell in charge states with an ionization energy above of $\sim$ 13 eV, or only with strong losses. The extraction efficiency for lead in a 2+ charge state with an ionization potential of 15.0 eV is only $\sim$ 1%, because of the low extraction efficiency lead was not counted as observed. The result points at the buffer gas contaminates O_2, N_2O, OH and N with ionization energies between 12.1 and 14.0 eV.

In order to get rid of these contaminates the CSC needs to be upgraded to operate at

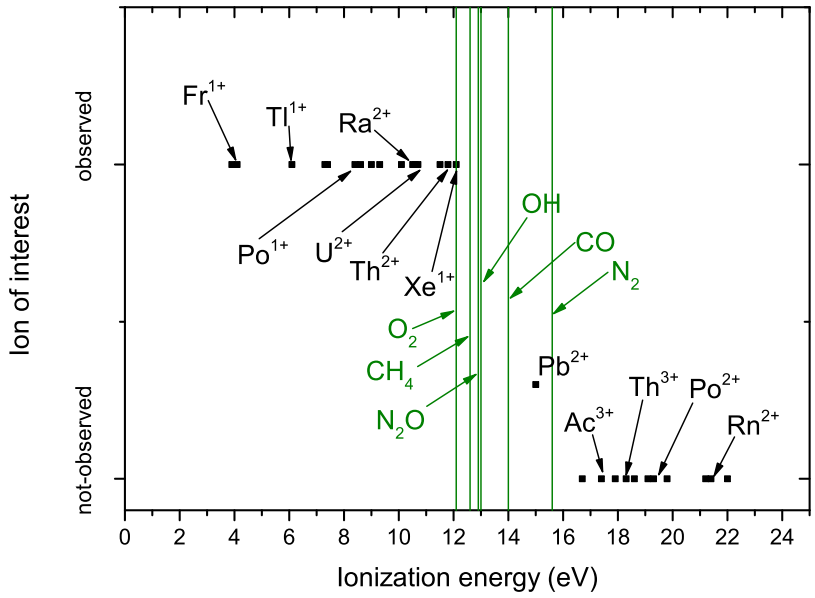

Figure 7.9: Ionization energy of the charge state of the ion of interest extracted from the cryogenic stopping cell in comparison the ionization energy of expected buffer gas atoms and molecules. The ionization energies are taken from [Kra14]. It can be seen that charge states with an ionization energy above $\sim$ 13.0 eV have not been extracted from the CSC, or only with reduced efficiency ($Pb^{2+} \sim 1\%$).

lower temperatures. From figure 4.4 it can be concluded that in a clean 40 K system only impurities of H_2, Ne, N_2, Ar, O_2, CH_4 and Kr can be present. In addition the contamination of O_2 and CH_4 can sufficiently be removed with active getter materials [Neu06].

In conclusion it can be summarized that the cryogenic stopping cell features excellent cleanliness. The combination of baking at temperatures blow 420 K and the cryogenic operation allows for excellent extraction and ion survival efficiencies while at the same time non UHV suitable materials, such as the RF carpet itself, can be used.

In order to demonstrate the element independence of the extraction of ions from the cryogenic stopping cell the chemical reaction rate can be taken into account. For many elements the reaction rates with oxygen are know from chemistry. Among all elements thorium and uranium belong to the most reactive elements in the periodic table [Ani03].

The chemical reaction can be written as

$$X^+ + M \Leftrightarrow X^+M^*, \tag{7.3}$$

for an ion of interest X^+ and a molecule M. The resulting molecule X^+M^* may be unstable with respect to dissociation but be stable by collisions with buffer gas atoms. The net result can be described by the reaction rate constant k. Thus a differential

equation

$$\frac{dn}{dt} = -k\ n\ \rho_M, \tag{7.4}$$

describes the time evolution of the reaction for a number of atoms or ions n with the concentration of a contaminant molecule ρ_M. The time constant T_M^X for the reaction of an ion of interest X^+ and a molecule M can be written as

$$T_M^X = \frac{1}{k\ \rho_M}. \tag{7.5}$$

From the ration rate constant a reaction time for a known concentration inside the stopping cell can be calculated [Kud01]. Inversely to the reaction time an upper limit for the time of stay for ions of different elements can be calculated, based on the time scale of the formation of a compound molecule with a certain contaminant molecule. Typical reaction rate constants for the formation of an ion-molecule adduct are given in table 7.5.

Reaction	Rate constant (cm^3/s)	Reference
$Fe^+ + O_2$	$4.3 \cdot 10^{-13}$	[Koy02]
	$4.3 \cdot 10^{-13}$	[Car02]
$Cd^+ + O_2$	$< 1.0 \cdot 10^{-14}$	[Koy02]
	$< 1.0 \cdot 10^{-14}$	[Car02]
$Ta^+ + O_2$	$4.7 \cdot 10^{-10}$	[Koy02]
	$4.6 \cdot 10^{-10}$	[Car02]
$Pt^+ + O_2$	$1.6 \cdot 10^{-13}$	[Car02]
$Ce^+ + O_2$	$1.05 \cdot 10^{-9}$	[Cor97]
$Er^+ + O_2$	$2.5 \cdot 10^{-10}$	[Kox01]
$Au^+ + O_2$	$1.2 \cdot 10^{-13}$	[Koy02]
$Au^+ + O_2$	$1.4 \cdot 10^{-13}$	[Car02]
$Th^+ + O_2$	$1.2 \cdot 10^{-9}$	[Cor97]
$U^+ + O_2$	$1.17 \cdot 10^{-9}$	[Cor97]
	$9.5 \cdot 10^{-10}$	[Smi02]

Table 7.5: Reaction rate constants of some ions with oxygen contaminant molecules.

For the two reactive elements thorium and uranium the reaction time results to $T_{O_2}^{Th} \sim$ 160 ms and $T_{O_2}^{U} \sim 200$ ms, with a reaction rate constants of $k_{Th} = 1.2 \cdot 10^{-9}$ and $k_U = 9.5 \cdot 10^{-10}$, respectively [Ani03]. A maximal or worst-case oxygen contamination of 1 ppb was assumed at an area density of 3.6 mg/cm^2 helium, corresponding to a oxgen concentration of $\rho_{O_2} = 5 \cdot 10^9$ part/cm^3. For non-reactive elements the reaction rate constants can be four to five orders of magnitude small, therefore reaction times of several minutes are reached.

This estimate shows that even for the most reactive elements molecular formation is not a limiting factor for the cryogenic stopping cell, because of the excellent cleanliness.

It shows that elements with smaller reaction rate constants require less cleanliness and are thus easier to extract from the stooping volume as bare ions.

It needs to be pointed out that reducing the extraction time of ions from the stopping cell at the same time lowers the restrictions on the cleanliness of the stopping gas, because the ions of interest perform less collisions during their extraction. Therefore short extraction times are not only important if the ion of interest is short lived nuclei, but also allows for reduced cleanliness requirements. The extraction time of ions produced at the FRS will be discussed in the next chapter.

7.2.3 Operational stability of the FRS Ion Catcher

During the 2014 experiment the full FRS Ion catcher was repeatedly tuned to the settings for ^{213}Fr, forming a sort of standard settings, in order to monitor the daily efficiency of the full system. The normalized efficiency of five individual measurements is shown in figure 7.10. In addition the black markers on the bottom of the figure indicate the time periods when data was taken at the FRS. The FRS experiment shared the beam with other experiments at GSI and machine experiments and therefore the beam was only available about half of the time during ten days of experiment.

The full FRS-Ion Catcher shows a good stability during the eight days of experiment. Only one measurement after 160 h deviates slightly from the mean efficiency. This may be caused by non-perfect tuning, since the standard settings were not re-optimized for the individual measurements. The stability measurements demonstrates that with the cryogenic stopping cell as part of the FRS Ion Catcher already now, without retuning of the system, measurements are possible with a duration of $\sim$ 200 h, corresponding to more than a week experiment. This means that at the future low energy branch of the Super-FRS precision experiments will be possible addressing nuclides with low production ratios down to a few per day.

7.3 Extraction time of projectile fragments from the CSC

An important performance characteristic of a stopping cell is its extraction time, since that limits the access to nuclides with very short lifetimes. In addition fast extraction of ions from the stopping volume reduces the restrictions on the cleanliness and purity of the stopping gas. The extraction time of ions from the cryogenic stopping cell was investigated offline and found to be area density independent (see chapter 6.4). In order to improve the understanding of the processes occurring during the extraction of ions originating from a relativistic secondary beam, the extraction time of ions produced in-flight at the FRS was measured.

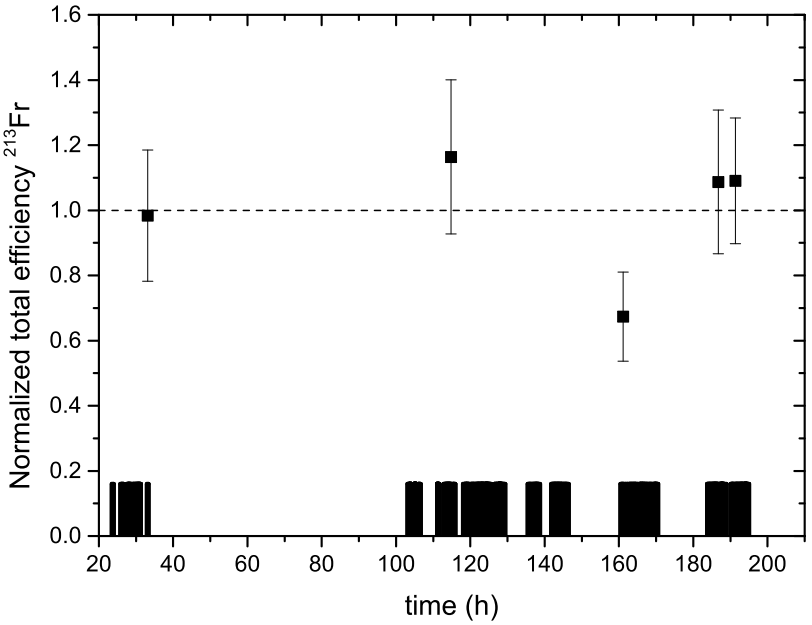

Figure 7.10: Normalized efficiency measured during the 2014 experiment for ^{213}Fr projectile fragments. The efficiency is determined between the FRS high energy identification and the detected ions at the MR-TOF-MS. The efficiency was measured five times during the experiment and shows the stability of the full FRS-Ion Catcher. In addition the black markers on the bottom of the figure indicate the time periods when ^{238}U primary beam was available and data was taken at the FRS.

By the successful extraction of ^{220}Ra, ^{213}Rn, ^{218}Rn and ^{221}Ac ions with half-lives of 18 ms, 19.5 ms, 35 ms and 52 ms, respectively, the short extraction time for ions originating from a relativistic secondary beam from the cryogenic stopping cell was demonstrated.

A quantitative determination of the extraction time was performed using ^{221}Ac fragments [Pur13]. A stopping gas pressure of 49 mbar, a temperature of 74 K and an electric field strength of 22.2 V/cm along the body of the stopping volume were used. While for most measurements ion bunches with a pulse length of several seconds were used, for the extraction time measurement the accelerator pulse structure was shortened to provide ion bunches of 4 to 6 ms. Under this condition ^{221}Ac ions were stopped, extracted from the CSC and identified by the Si detector in the diagnostics unit and a time resolved decay pattern was recorded.

The time dependence of the decay rate of the ^{221}Ac fragments after injection of the ion bunches is shown in fig. 7.11. Let P be the rate of ^{221}Ac extracted from the CSC (without decay losses), N the number of ^{221}Ac collected on the aluminum foil mounted in front of the detector Si, and λ the rate constant for the radioactive decay of ^{221}Ac. Then the rate equation describing the activity of ^{221}Ac ions on the foil is given by

$$\frac{dN}{dt} = Pe^{-\lambda t} - \lambda N. \tag{7.6}$$

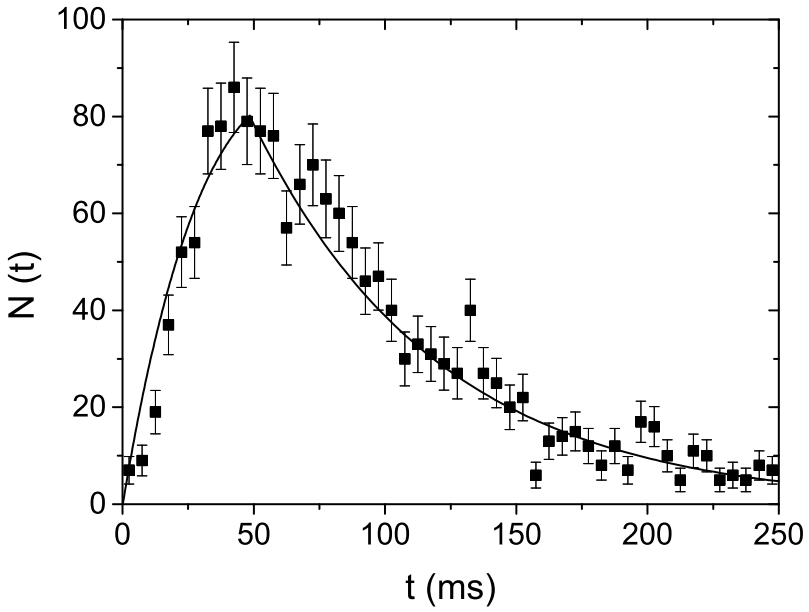

Figure 7.11: Extraction time measurement with ^{221}Ac ions. The number of ^{221}Ac decay events recorded with the detector Si are shown as a function of time after injection of ^{221}Ac ions with a pulse width of 4 to 6 ms. The solid curve shows a fit using eqs. (7.7) and (7.8), [Pur13].

Assuming that the ions are stopped uniformly throughout the gas volume of the CSC and the ion transport is uniform, the rate P is constant up to a time $t = t_{\max}$ when the last ion of the stopped ion distribution leaves the cell, and is zero for larger times. Then the solution of eq. (7.6) is

$$N(t) = P \cdot t \cdot e^{-\lambda t} \text{ for } t < t_{\max} \tag{7.7}$$

and

$$N(t) = N(t_{\max}) e^{-\lambda(t-t_{\max})} \text{ for } t > t_{\max}. \tag{7.8}$$

The average extraction time, t_{extr}, for the ions is then given by $t_{\max}/2$. The fit using eqs. (7.7) and (7.8) in fig. 7.11 shows good agreement with the data. After (45.4 ± 2.8) ms the last ^{221}Ac ions are extracted from the cell, yielding a mean extraction time t_{extr} of 22.7 ms for ions stopped in the center of the CSC. This measurement agrees well with off-line studies that yield an extraction time for ^{219}Rn ions of 25 ms [Pla13a] and with the expectations from mobility theory of 27.5 ms [Pur13].

7.4 Identification of exotic nuclei using the CSC & the MR-TOF-MS – The mass tagger

An big advantage of the in-flight production of exotic nuclei is the single particle identification. However a correct and precise calibration of the in-flight detectors is mandatory, which can be a complex and lengthy procedure. If the ion of interest is

far away in charge Z and mass A from the primary beam, there can be a significant difference between calibration settings and the operation settings of the in-flight detection system due to the large difference in energy lost between primary beam and fragment. This makes it hard to identify the ion of interest correctly and a rescaling of the calibration of the in-flight identification scheme is required.

Typical approach is the usage of a solid stopper at the final focus of the fragment separator in combination with decay detectors e.g. Isomer TAGging detector (ITAG) [ITAG] and alpha-tagger [Far11]. These detectors measure the characteristic decay properties of the produced exotic nuclei such as the energy of alpha or gamma decays, lifetimes or branching ratios between decays. Thus both tagging schemes require knowledge about the decay properties of nuclides in the region of the ion of interest. During the 2011 and 2012 experiments the alpha-tagger was used as an additional identification detector at the FRS. With this detector it was possible to identify radioactive ions in the mass region above lead by their characteristic alpha decay, e.g. ^{211}Fr, ^{223}Th etc.

During the 2014 experiment also non alpha decaying nuclei should be measured. In order to thermalize the radioactive ions of interest for high precision low-energy experiments in a stopping cell a clear in-flight identification is required. In the case of fission fragments an identification becomes difficult because the ions of interest are almost half the nuclear charge of the primary beam. In addition the nuclides are not decaying via alpha emission and therefore the alpha tagger can not be used. Under this conditions the ITAG could in general still be used, which relies on the identification of the ions based on characteristic gamma emission. However this kind of identification only works with radioactive nuclei and particular with those, where characteristic gamma energies are known.

Thus as a new identification scheme is proposed. Using the cryogenic stopping cell, with its high total efficiencies and reliability, in combination with a non scanning high resolution mass spectrometer allows to identify ions by their mass, forming a mass tagger. After thermalization of an unknown ion species with the CSC a high resolution mass measurement can be used to identify the radioactive nuclei by their mass, for this measurement multireflexion time-of-flight mass spectrometers are a good choice.

The new concept was demonstrated at the FRS Ion Catcher. The FRS was tuned for the production of in-flight fission fragments of ^{238}U primary beam at 1000 MeV/u. As shown in figure 7.12 a clean identification plot can be recorded. The different nuclei are clearly separated in the ID plot in their A/Q measured by the time-of-flight detectors and Z measured by the energy loss in the MUSIC. Through the high kinetic energy the produced exotic nuclei are fully ionized. However the calibration of the MUSIC is not applicable for the intermediate mass ions. A re-scaling of the in-flight calibration is possible after identification of one of the produced exotic species. In order to stop a certain nuclei in the CSC the range distribution needs to be determined. This has been done by varying the VH degrader in front of the last MUSIC and monitoring the traversing ions in the last MUSIC detector.

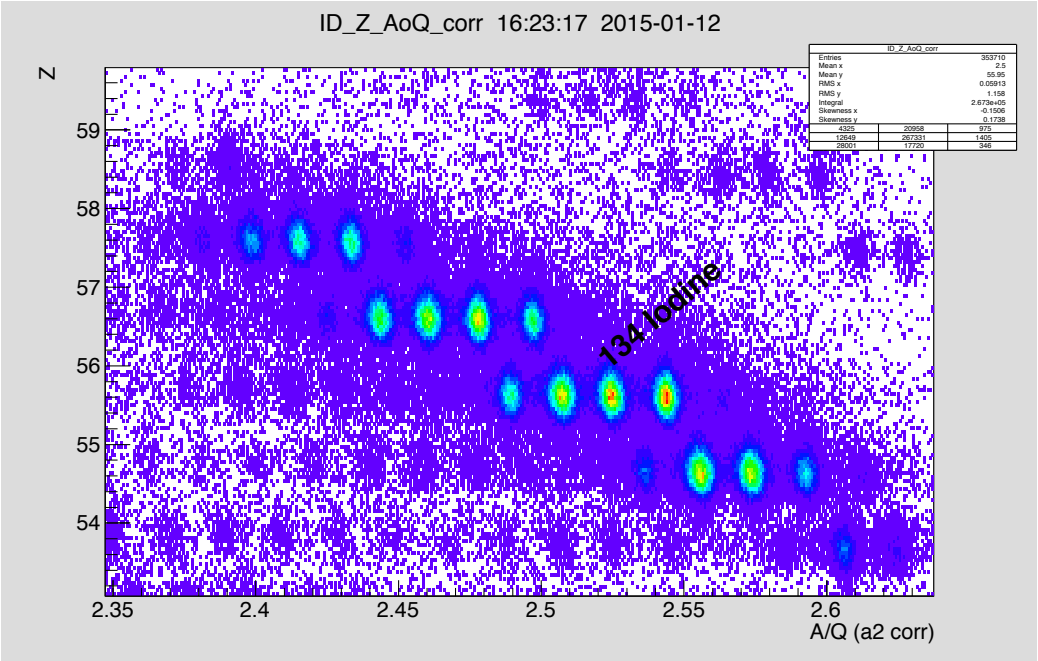

Figure 7.12: FRS online identification plot of ^{134}I, showing the AoQ measured by the trajectories in the magnetic field and the charge state measured by the ionization chambers during the experiment. The spectra was calibrated with ^{238}U primary beam, the online calibration has a deviation about 2.5 e and the calibration was rescaled.

In order to identify one of the produced species, its stopping point is scaled from the MUSIC to the CSC. Starting with a broad mass range the mass number of the thermalized fragment is determined. A high resolution mass measurements reveals the clear identification of the nuclei. In our case the fragment could be identified as ^{134}I, as seen in the high resolution mass spectra in figure 7.13. For the measurement ^{134}Xe ions from an internal electron impact ion source were used as a calibrant for the mass spectrometer. A clear peak at the mass of ^{134}I can be seen in the spectra.

From the mass measurement and the know identity of the nuclide the in-flight ID can be scaled. The fragment labeled in the ID plot (fig. 7.12) is ^{134}I, showing a deviation of 2.5 e in nuclear charge Z, the identification can be scaled by this value. The A/Q shows the correct value.

In the offline analysis the range of all fragments can be analyzed. Assuming a range distribution with known width of the fragments and distance in range between the MUSIC and the CSC the range distribution of the cocktail beam can be derived. In figure 7.14 the range distribution of all radio active ions is shown. In addition the position and width of the CSC are shown (hashed area). This verifiers the tuning of the VH degrader and therefore the stopping. It also shows the separation in range of the different fragments produced by in-flight fission at the FRS. A good control over the stopping point is required in order to stop the correct fragment and to use the combination of CSC and MR-TOF-MS as a mass tagger. Not only ^{134}I is stopped in

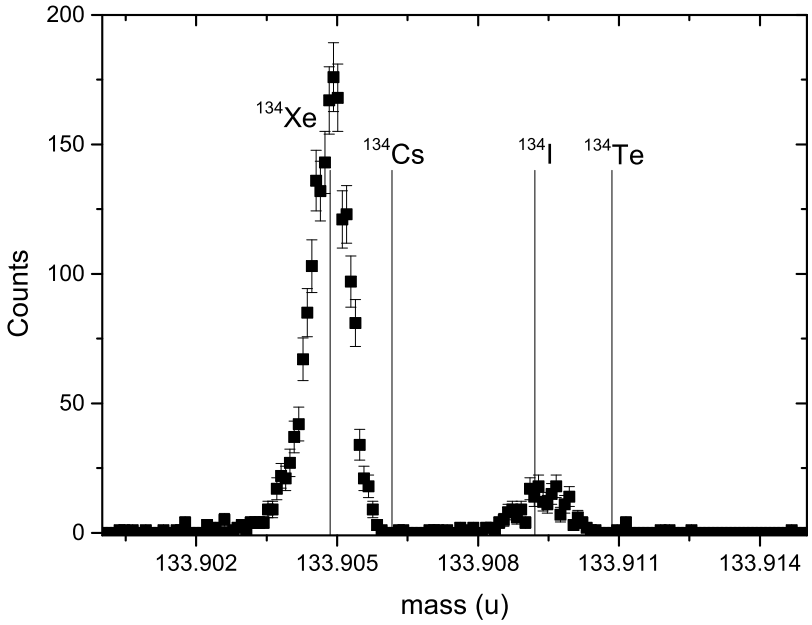

Figure 7.13: Mass spectra of ^{134}I taken with the MR-TOF-MS. The mass line at 134 u was identified as ^{134}I by its mass. This allows a re-calibration of the FRS in-flight ID.

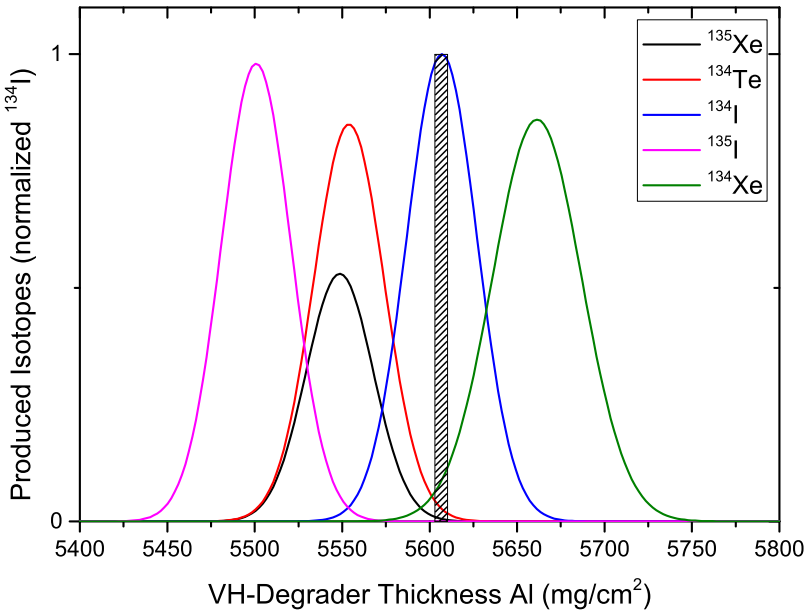

Figure 7.14: Range scan performed using the last MUSIC for the different Isotopes in the cocktail beam of the FRS. From the range in the MUSIC the point of stopping can be scaled to the CSC. In the graph the estimated range distribution is shown for the five closes in range lying isotopes compared to ^{134}I. The area covered by the CSC is shown (hashed area).

the CSC, but also a small fraction in the order of a few % of the fragments ^{134}Xe, ^{134}Te and ^{135}Xe produced by fission. This demonstrates the separation power of the stopping cell, which allows a suppression of neighboring nuclides through selective stopping. Therefore clean beams containing dominantly one ion of interest can be extracted from the stopping cell and used for downstream spectroscopy experiments (see chapter 7.5).

The concept of using the prototype CSC and the MR-TOF-MS as a mass tagger has proofed to be a well suitable technique for rescaling of the in-flight calibration of the fragment separator. It can be used with nuclei with half lives down to < 20 ms up to stable nuclides, because it does not relay on radioactive decays. In only a few hours a fix point for the calibration of the FRS could be determined and high precision mass measurements of six ^{238}U fission fragments could be performed. Taking this approach further and using the CSC and the MR-TOF-MS as a combined detector concept allows identification of ions which are not clearly separated in the in-flight ID plot. Thus also ions, which traverse through the FRS separator in a H-like or He-like charge state can be identified by high precision mass spectrometry after thermalizing in the cryogenic stopping cell. In addition combining the mass tagger approach with the previously used ITAG approach allows for maximal flexibility and the identification of any nuclide by various properties.

7.5 Alpha spectroscopy of thermalized ^{238}U projectile fragments

The FRS Ion Catcher was used to perform alpha spectroscopy of thermalized radioactive nuclides. The alpha decaying nuclides were produced by ^{238}U fragmentation at 1000 MeV/u primary beam energy. The separation power of the FRS in combination with the selective stopping in the CSC allows for alpha spectroscopy of clean samples of the nuclides of interest. Therefore comparable simple alpha energy spectra can be recorded with a clear identification of the alpha lines, arising from the decay chain of the fragment of interest.

As a sample spectra the decay chain of ^{220}Ra and ^{221}Ra are shown in figure 7.15. The nuclides were collected on the foil in front of the SI detector in the DU. The alpha decay lines are separated in the spectra and can be described by exponential modified Gaussian peaks. The alpha decays of ^{221}Ra are covered by the decays of ^{211}Bi. In addition the decays chains of ^{218}Rn, ^{219}Rn, ^{221}Ac, ^{220}Fr, ^{223}Th and ^{224}Th could be measured. The alpha energy was measured and following equation (3.15) the Q-value of the decay was calculated. The decay parameters are reported in table 7.6.

The SI detector was calibrated with a linear function using the ^{219}Rn decays from the offline source inside the CSC and alpha particles form a second 3-line alpha source containing ^{239}Pu, ^{241}Am and ^{244}Cm mounted off beam axis next to the RFQ segment. The Si detector can be moved in front of this 3-line alpha source for calibration. For

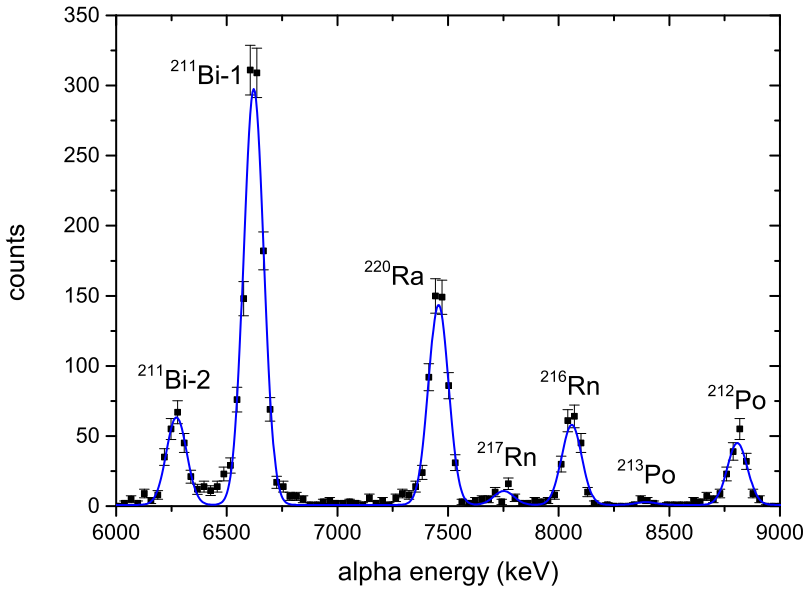

Figure 7.15: Sample alpha energy spectra of ^{220}Ra produced by ^{238}U projectile fragmentation at 1000 MeV/u at the FRS Ion catcher, measured with the Si detector in the DU.

the spectroscopy measurement the recoil source was pulsed to a lower voltage and therefore no ^{219}Rn decays are detected at the SI detector. The alpha decays of ^{211}Bi following the decay of ^{211}Pb with an half life of 36.1 min are still detected and can be used for re-calibration of the alpha spectra.

The linearity of the SI detector and the data acquisition system was validated from a calibration spectra with all calibrant peaks. A quadratic term was added to the calibration and found to be in the order of 10^{-4}. Omitting the quadratic contribution introduces a systematic shift (< 2 keV), which was found to be within the error bars of the alpha spectroscopy set up. Therefore a linear calibration was used for the determination of the alpha energies of the projectile fragments.

The difference in energy loss of alpha particles of different energy in the aluminum foil was investigated by a [ATIMA] energy loss calculation. The difference between the energy loss of an alpha particle emerging the decay of the calibrant ^{211}Bi (e.g. $E_\alpha = 6622.9$ keV) and an alpha particle with an energy of 9000 keV is about 9.7 keV. The calibration using all peaks in the decay pater of ^{219}Rn from the offline source accounts already for the linear component of the energy loss as a function of alpha energy. The final alpha energies listed in table 7.6 have been additionally corrected with an fourth order polynomial for the difference in energy loss at different alpha particle energies.

Plotting the deviation between the measured α energy and the literature value allows determination of the systematic errors of the detector set up, see figure 7.16. The measured alpha energies scatter around the know literature values. The deviation between the alpha energies E_α determined at the FRS Ion Catcher and the literature

value E_α^{lit} is described by a Gaussian distribution, as seen at the right side of figure 7.16. The distribution of the deviation has a width of $\sigma_{E_\alpha} = 9$ keV. This has to be added to the statistical errors listed in table 7.6.

Isotope ^{A}X	$t_{1/2}$	Fed level^{lit} (keV)	E_α (keV)	ΔE_α (keV)	Q_α (keV)	ΔQ_α (keV)
^{211}Po	0.516 3 ss	0	7450.2	5.1	7594.5	5.2
^{211m}Po-1	25.2 6 s	1633.4 10	7272.7	3	9047.0	3
^{211m}Po-2	25.2 6 s	0	8877.3	12.3		
^{211m}Po-3	25.2 6 s	897.77 12	7999.8	27.3		
^{212}Po	0.299 2 μs	0	8800.6	12.1	8970.4	12.3
^{213}Po	3.72 2 μs	0	8386.9	46	8547.9	46.9
^{214}Po	164.3 20 μs	0	7706.2	37.1	7853.4	37.8
^{215}Po	1.781 5 ms	0	7386.6	2.4	7527.0	2.4
^{216}At	0.3 3 ms	0	7793.2	14.7	7940.6	15
^{215}Rn	2.3 10 μs	0	8691.9	18.8	8848.8	14.9
^{216}Rn	45 5 μs	0	8055.2	14.6	8206.6	10.7
^{217}Rn	0.54 5 ms	0	7750.3	25.2	7896.2	25.7
^{218}Rn	35 5 ms	0	7143.3	23.8	7277.2	24.3
^{219}Rn-1	3.96 1 s	0	6821.6	2.2	6949.6	2.2
^{219}Rn-2	3.96 1 s	271.228 10	6557.5	2.9		
^{221}Rn	28 2 s	0	not resolved		–	
^{217}Fr	19 3 μs	0	8312.5	11.9	8469.1	12.1
^{220}Fr	27.4 3 s	0	not resolved		–	
^{219}Ra-1	10 3 ms	0	7989.9	14.3	8135.2	9.1
^{219}Ra-2	10 3 ms	315.82 4	7674.2	12.1		
^{220}Ra	18 2 ms	0	7456.7	6.8	7595.1	7.0
^{221}Ac-1[1]	52 2 ms	0	7636.9	15.3	7778.0	15.6
^{221}Ac-2	52 2 ms	209 20	7438.1	89.8		
^{223}Th	0.6 2 s	140.01 10	7297.1	9.1	7570.7	9.3
^{224}Th-1	1.05 2 s	0	7164.0	11.5	7296.4	10.6
^{224}Th-2	1.05 2 s	178.4 1	6995.7	19.8		

Table 7.6: Alpha energies and Q-alpha values of radioactive nuclei measured during the FRS Ion Catcher experiment at GSI, produced by ^{238}U projectile fragmentation at 1000 MeV/u. A systematic error of $\sigma_{E_\alpha} = 9$ keV needs to added to the statistical errors.

The Q_α values of 16 isotopes could be determined at the FRS Ion Catcher and are plotted in figure 7.17 as a function of the neutron number N and listed in table 7.6. For the calculation of the Q_α values from the alpha energies the binding energy was taken into account. In figure 7.17 characteristic maximum of the Q_α values around the $N = 126$ shell closure is well reproduced in our measurements. The crossing of

[1] improved Q_α value, see discussion in text

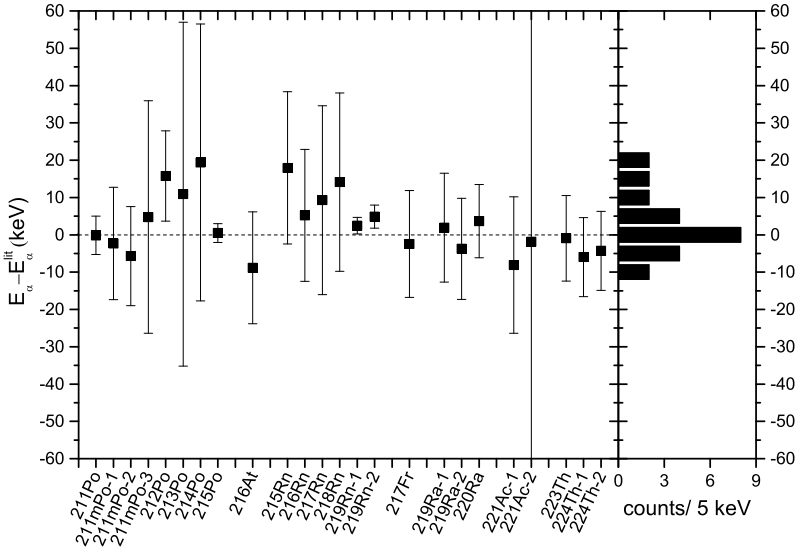

Figure 7.16: The difference between the measured alpha energies E_α at the FRS Ion Catcher and the known literature value E_α^{lit} is shown on the left hand side. On the right side the projection of the deviation is plotted. This allows determination of the systematic error of the alpha spectroscopy.

the Q_α values of the astatine and radon chains at $N = 131$ and of the radon and radium chains at $N = 133$ are reproduced in our measurements.

In the literature the Q-alpha value of ^{221}Ac is stated with a 50 keV error. In the measurements of [Bor70] the nuclide was produced by a ^{208}Pb + ^{19}Fe reaction and measured as part of the decay chain of ^{225}Pa, in the decay of ^{225}Pa two alpha lines were identified, feeding the ground state and a close lying (50 keV) state in ^{221}Ac [Bor70, Huy88]. However corresponding gamma radiation was not detected and no long lived 50 keV state was reported in ^{221}Ac. It is concluded, that alpha spectroscopy of the direct produced ^{221}Ac should not suffer from a possible close lying isomeric state. In the case a shorter lived isomeric state is present, due to the extraction time of 25 ms from the CSC to the detector, the state might have decayed and the alpha measurement should detect the full energy of the decay. In the case a longer lived isomeric state is populated and decaying via alpha emission in ^{221}Ac a half life measurement will allow an identification of the isomeric state. In order to validate this a half live measurement was performed for ^{221}Ac using short ion pulses from the SIS-18, see chapter 7.5.1. From this it was concluded that in our measurements the full Q-alpha value of the decay of ^{221}Ac to ^{217}Fr is observed and in our measurements there is no evidence for an close lying long-lived isomeric state decaying by alpha emission. Therefore the error on the Q-alpha value was not increased, as in [Bor70, Huy88].

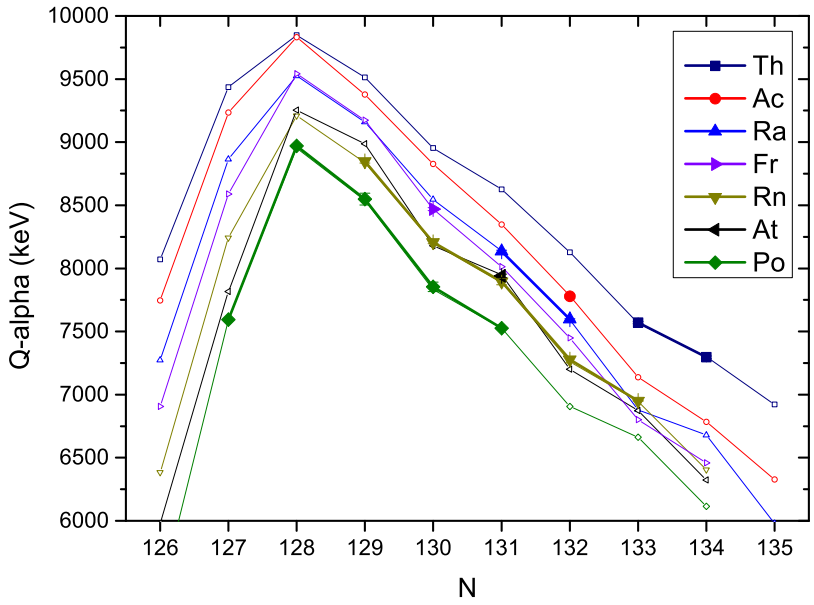

Figure 7.17: The Q_α value of the decay of the isotopes measured at the FRS Ion Catcher during the 2011, 2012 and 2014 experiments is plotted as a function of the neutron number N. The Q_α values are shown as solid symbols within the literature values (open symbols).

7.5.1 Half life measurement of ^{221}Ac and ^{223}Th

The half life of ^{223}Th and ^{221}Ac were measured using short ion pulses from the SIS-18 with a length of 4 to 6 ms. Similar to the extraction time measurement a time resolved decay pattern was recorded on the Si detector in the diagnostics unit. Gating on the characteristic alpha energies of ^{223}Th and ^{221}Ac, respectively, the half life of the two nuclides can be determined. For fitting of the decay pattern a Gaussian peak was convoluted with an exponential function, thus it accounts for the increase dominated by the extraction process of ions from the CSC and for the exponential decay dominating after all ions are extracted. In figure 7.18 the decay pattern are shown for the two nuclides. The solid line represents the fit to the data.

For ^{223}Th the half life was determined by gating on the alpha decay of ^{223}Th and in addition while gating on the alpha decay of its daughter nuclides. The alpha decay line of ^{215}Rn, the second daughter of ^{223}Th, is completely separated in the energy spectra and therefore allow a back ground free determination of the half life of ^{223}Th, because ^{219}Ra and ^{215}Rn have a half life of only 10 ± 3 ms and 2.3 ± 0.1 μs and therefore the decay pattern of ^{215}Rn is dominated by the decay of the mother nuclide ^{223}Th. The half life determined by the two methods is in agreement with each other and in table 7.7 the final result is given.

Similar to ^{223}Th the half life of ^{221}Ac can be derived directly or from the decay pattern of the daughter nuclides ^{217}Fr and ^{213}At with half lifes of only 19 μs and 125 ns. The actinium half life determined from the daughter nuclides results to 50.4 ± 2 ms and

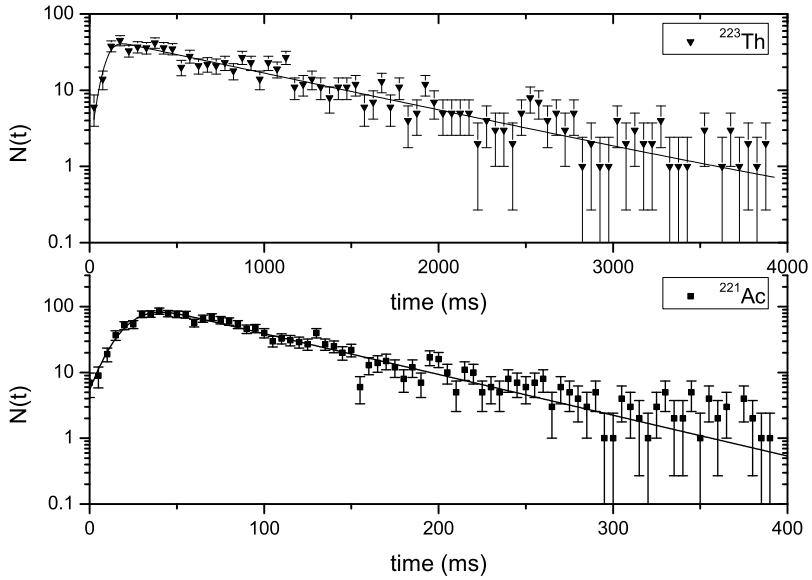

Figure 7.18: Half life measurement of ^{223}Th and ^{221}Ac. The number of ^{223}Th (^{221}Ac) decay events recorded with the Si detector are shown as a function of time after injection of the ions with a pulse width of $4-6$ ms into the CSC. A Gaussian plus exponential decay function describes the extraction process from the CSC and the decay pattern at the same time and was therefore used for determination of the half life.

47.2 ± 3.5 ms, respectively. This indirect method agrees with the direct half life determination of ^{221}Ac resulting in 49.5 ± 3 ms. The actinium decay pattern shows a long lived component with a half live of 444 ± 164 ms and at an alpha energy of 7474.4 ± 49 keV. This could hint on a longer lived isomeric state in ^{221}Ac, but in the decay pattern of ^{217}Fr and ^{213}At no long lived component is observed. The long lived component could be identified and arise from the decay of ^{211}Po, following the subsequent decays of ^{219}Ra and ^{215}Rn, underlying the ^{221}Ac decay pattern with an relative abundance of $\sim 4\%$.

The final half lifes of ^{211}Po, ^{223}Th and ^{221}Ac are listed in table 7.7. The half lifes of ^{223}Th is in good agreement with the know literature values from ENSDF. The half life value for ^{221}Ac deviates about one sigma from the literature value based on the measurements of [Bor70]. The former measurements higher value might be due to an overlap between the peaks of ^{221}Ac and ^{212}At in their complex alpha spectra obtained from a ^{205}Tl + ^{22}Ne reaction without additional mass separation. The large error on the ^{211}Po half life in our measurement is dominated by the low statistics of the decay.

Isotope ^{A}X	$t_{1/2}^{lit}$ (ms)	$\Delta t_{1/2}^{lit}$ (ms)	$t_{1/2}$ (ms)	$\Delta t_{1/2}$ (ms)	Ref.
^{223}Th	600	20	618	47	[ElL87]
	660	10			[Val70]
	900	10			[Tov58]
^{221}Ac	52	2	49.5	3	[Bor70]

^{211}Po	516	3	444	164	[Bar74]
	560	40			[Tov58]
	520	-			[Spi53]
	500	100			[Win54]

Table 7.7: Half life of ^{223}Th and ^{221}Ac determined by time resolved alpha spectroscopy. The reference values are taken from ENSDF.

Recording time resolved decay pattern allows a determination of the half life in correlation to the alpha decay energy. This has proofed to be a very useful technique to disentangle alpha decay energies of underlying peaks even if the relative abundance is only a few per cent. The technique was demonstrated in the measurement of ^{211}Po and ^{221}Ac, which shows that underlying peaks can be efficiently disentangled if short ion pulses are used for alpha spectroscopy of thermalized heavy ions while recoding alpha energy and time of each decay. In addition the data can be analyzed using a alpha-alpha coincidence method, by this the half-life of all daughter nuclides could be obtained in addition to the half-life of the initial fragment.

7.6 Study of the angular momentum distribution populated by fragmentation at 1000 MeV/u

In depth understanding of the reaction process occurring during in-flight fragmentation at relativistic energies is of great interest for nuclear structure and the understanding of the nuclear forces and also for e.g. for the usage of fragmentation at future RIB facilities. The properties of the fragments e.g their production cross sections, transverse and longitudinal momentum distribution or their angular momentum can be determined experimentally and are a good probe for the validity of theoretical models describing the fragmentation process. Measuring the fraction of a nuclei produced in its ground state compared to possible isomeric states can provide information about the angular momentum distribution populated during the fragmentation process. Comparing experimental isomeric ratios to the predictions e.g. by [Jon97] or to the macroscopic, geometrical approach following the ABRABLA code [Gai91], the understanding of the fragmentation process can be tested.

The high-spin isomeric states in ^{211}Po are known since the early work of Jentschke in the sixties [Jen54] and ^{211}Po is a well known isotope with a rich level scheme, which was studied in detail in various experiments e.g. [McG1998, For99]. In figure 7.19 the energy of the known levels in ^{211}Po is shown as a function of angular momentum. The four known high-spin isomeric states are highlighted in red. In addition the Yrast-Line is plotted assuming a spherical shape of the ^{211}Po nucleus, this shows that the high-spin states in ^{211}Po are close to the Yrast-Line and are therefore Yrast-states.

In ^{211}Po an isomeric state with a spin of $(25/2^+)\hbar$, a half life of 25.2 ms and an excitation energy of 1462 MeV mainly de-excites by alpha decay to ^{207}Pb. Similar the spin $(9/2^+)\hbar$ ground state with an half life of 516 ms undergoes an alpha decay. This has the advantage that the isomer and the ground state and their relative abundance can be studied using alpha spectroscopy [Kud89]. Higher isomeric states with half life of 243 ns and 2.8 μs and an angular momentum of $(31/2^-)\hbar$ and $(43/2^+)\hbar$ can be studied by gamma spectroscopy [Bow13], as indicated in figure 7.19. Therefore ^{211}Po is the ideal case to investigate the angular momentum distribution which is populated during the production of the isotope with angular momentum values ranging from $(9/2^+)\hbar$ to $(43/2^+)\hbar$. The isomer ratios and therefore the angular momentum distribution following direct α-beam reactions was studied in detail by α+^{208}Pb [Bar74] and α+^{209}Bi [Ram59] reactions. In addition ^{211}Po was used to investigate the angular momentum distribution populated in complete and incomplete fusion reactions using ^{6,7}Li incident on ^{209}Bi and ^{9}Be incident on ^{208}Pb targets [Gas06]. For the above reasons ^{211}Po was chosen at the FRS Ion Catcher to investigate the excitation and angular momentum distribution covered by in-flight projectile fragmentation at 1000 MeV/u of a ^{238}U primary beam on a ^{9}Be target by measuring the isomeric ratio.

The angular distribution was calculated as described in chap. 3.1 following the approaches by Goldhaber and Jong [Gol74, Jon97]. For the angular momentum distribution a $\sigma_f = 7.0$ was derived using the estimation of the quadrupole deformation

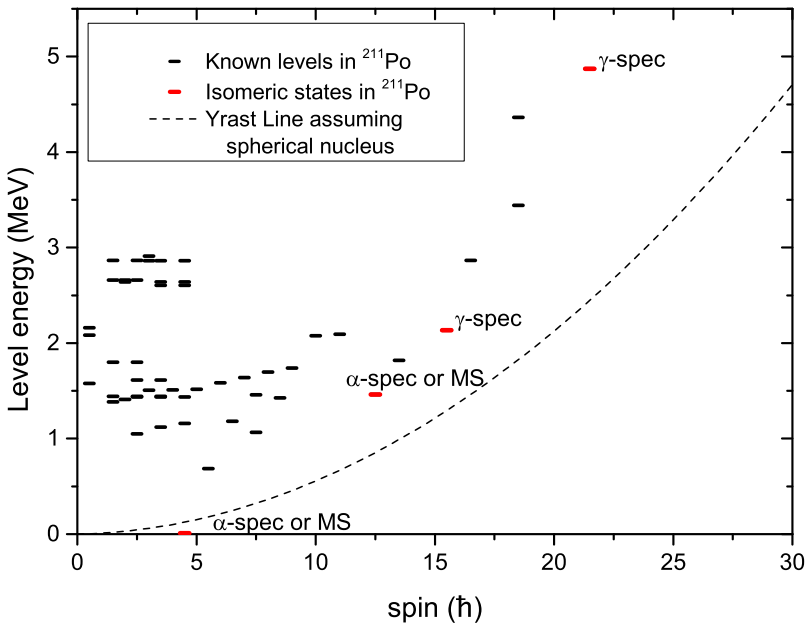

Figure 7.19: Yrast plot for experimentally observed excited states in ^{211}Po from ENSDF. For 53 out of 114 excited levels in ^{211}Po the excitation energy and the spin are known, for the remaining ones only the excitation energy is known. It shows that the measured isomeric states are Yrast states and allow an investigation of the angular momentum distribution following fragmentation with spin values from $(9/2^+)\hbar$ to $(43/2^+)\hbar$.

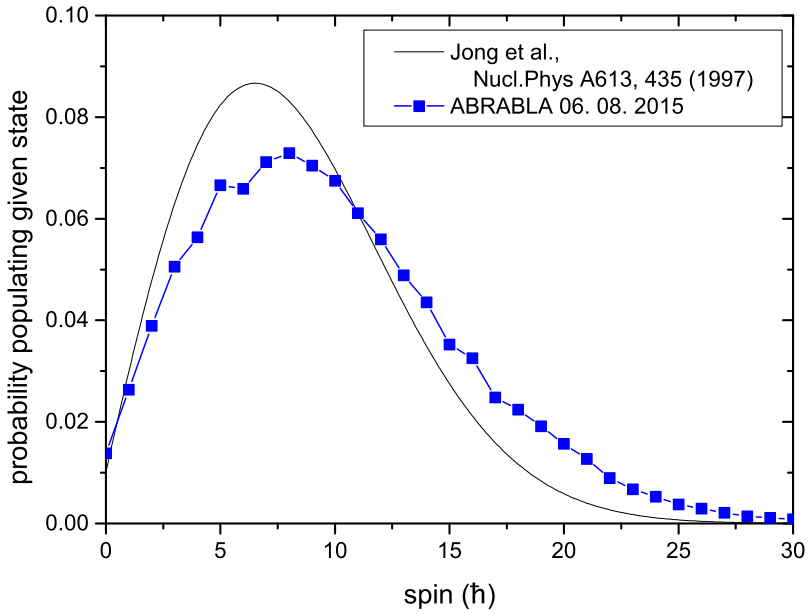

Figure 7.20: Angular momentum distribution for ^{211}Po calculated analytically following [Jon97] and simulated using ABRABLA. [Kel15]

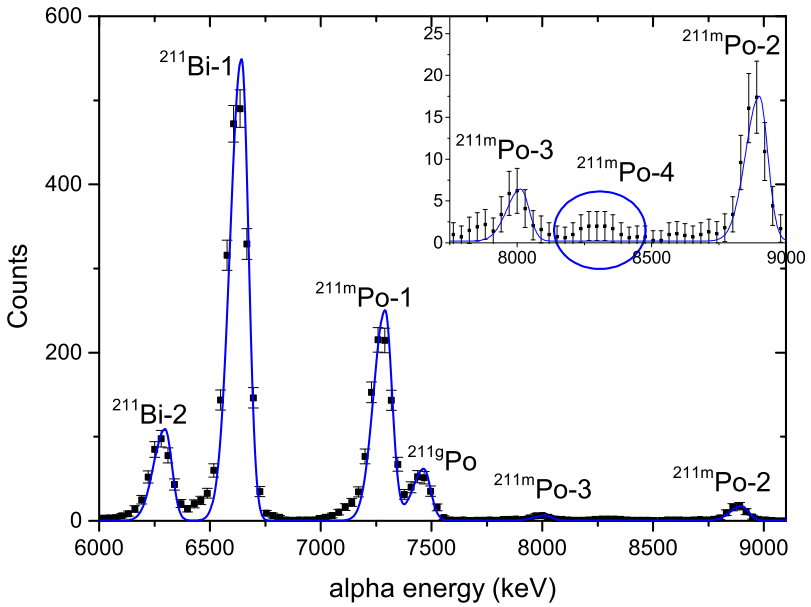

Figure 7.21: Energy spectra of the main alpha decay branches of ^{211}Po are shown, which were measured with the detector Si. From the spectra the ratio of ions measured in the ground and first isomeric state can be determined.

parameter of the projectile $\beta = 0.286$. The resulting distribution arising from fragmentation of ^{238}U to ^{211}Po is shown in figure 7.20. In addition the angular momentum distribution resulting a calculation using the ABRABLA code is shown [Kel15]. It can be seen that the analytic approach and the ABRABLA code fit together, as expected from the underlying abrasion-ablation molded. However, the ABRABLA code predicts the production of higher spin states compared to the analytical calculation, as seen by a tail to higher spin states. Both models describe the angular momentum of the pre-fragment and assume no additional broadening of the distribution during the ablation stage.

At the FRS Ion catcher the production of the $(25/2^+)\hbar$ isomeric and $(9/2^+)\hbar$ ground state in ^{211}Po were measured by high precision mass spectroscopy [Dic15a] and alpha spectroscopy. The data was combined with isomeric ratio measurements preformed by gamma spectroscopy by the RISING collaboration at the FRS at the GSI facility under same primary beam and target conditions [Bow13].
In figure 7.21 the alpha decay spectra of ^{211m}Po and ^{211}Po is shown, obtained with the SI detector behind the stopping cell. The measured alpha energies are listed in table 7.6 and are well in agreement with the literature available. With the measured statistic, there is only a slight evidence for an alpha decay of ^{211m}Po with an energy of 8300 ± 15 keV and relative intensity of 0.25 ± 0.02 %, which has been reported by [Per62] but not in the measurements of [Jen54]. With the taken statistics we can not confirm a decay line with 8300 keV energy. The region is highlighted in the inset in figure 7.21. The isomer ratio R_{exp} was calculated from the relative abundance of the dominant decay channels of the ground state and the isomeric state in the alpha spectra, taking the individual intensities into account. The production ratio for the $(9/2^+)\hbar$ ground state and $(25/2^+)\hbar$ excited state are listed in table 7.8, in addition

to the $(43/2^+)\hbar$ isomer state observed at [Bow13]. The isomeric ratio of the $(31/2^-)\hbar$ isomeric state with an half life of 243 ± 21 ns was not determined during the RISING campaign at GSI.

The higher spin isomeric states decay in the $(25/2^+)\hbar$ state, therefore in our measurement all higher spin isomers will have decayed into the $(25/2^+)$ state, at the time when the ions reach the Si detector. This has been taken into account for the calculations of the isomer ratio and the comparison to the analytical calculations. For the calculation of the isomer ratio from the two different angular momentum distributions several approaches were used, which are only valid for Yrast-states. The sharp cut-off approach was used, see equation (3.8). Assuming all spin states above an isomeric state will decay by gamma emission into this state, integration over the angular momentum distribution beginning from spin I of the isomeric state to the next state results in the isomeric ratio. Following the assumption of Gasques an empirical state mixing was introduced [Gas06]. The introduced effective angular momentum cut-off J_{eff} accounts for a spread in the angular momentum distribution, due to the neutron evaporation and the cascade of gamma rays from the initial compound nucleus to the final state [Gas06]. To account for the angular momentum of the neutrons and gamma rays $\delta = 0.5$ and $J_{eff} = 11.5\hbar$ have been taken similar as in [Gas06] ($\delta = 0.5$ and $J_{eff} = 10\hbar$). The value for J_{eff} was chosen such that the contribution of the angular momentum feeding the isomeric state reaches its maximum at the spin of the excited state, thus $11.5\hbar$, $14.5\hbar$ and $20.5\hbar$ have been assumed for J_{eff} for the isomeric states in ^{211}Po, respectively. A different approach to account for the change in the angular momentum distribution of the initial pre-fragment and the final fragment is take by Pal and Palit, who developed a hybrid model taking the effects on the fragment angular momentum of the abrasion and the ablation stage into account [Pal08]. In this model it was observed that the evaporation of light particles form the initial projectile-like prefragment increases the average angular momentum by about 60% [Pal08]. In addition the effects of a particle-hole spin coupling were considered, but not explicitly. In order to account for the additional broadening of the angular momentum distribution by this effect the spin cut-off parameter σ_f^2 may be multiplied by a factor 2 [Pal08, Bow13]. This has been done for the analytical angular momentum distribution of ^{211}Po where σ_f^2 was multiplied by two.

The calculated isomer ratios using the sharp cut-off R_{th} and the effective cut-off R_{th-mix} are given in table 7.8 respectively. The isomer ratio was calculated for the analytic angular momentum distribution R_{th}^f and for the distribution calculated via ABRABLA $R_{th}^{ABRABLA}$ and are compared to the experimental isomer ratios R_{exp}. In addition the isomeric ratio including the broadening of the angular momentum distribution due to the ablation stage and the a effect of particle-hole spin coupling has been calculated $R_{th}^{2\sigma_f}$. For a better comparison the calculated isomeric ratios are shown relative to the experimental observed isomeric ratios in ^{211}Po produced by in-flight projectile fragmentation at 1000 MeV/u in figure 7.22. For illustration the values for R_{exp}/R_{th} obtained by high resolution mass spectrometry have been shifted by 1 $\hbar$.

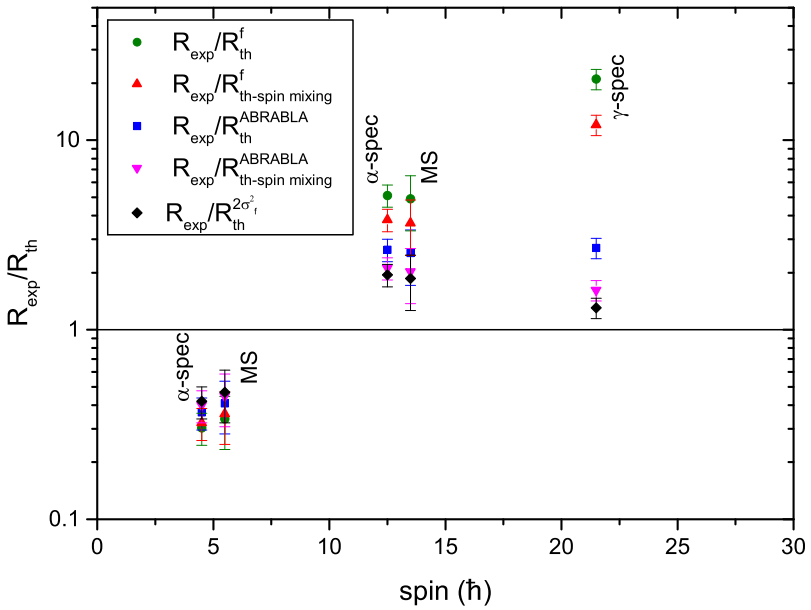

Figure 7.22: The ratio of the experimental isomer ratio R_{exp} of ^{211}Po to the analytical calculations R^{f}_{th} and predictions from ABRABLA code $R^{ABRABLA}_{th}$, using the sharp cut-off approach and the empirical spin mixing approach [Gas06]. For illustration the ratios obtained by high resolution mass spectrometry have been shifted by 1 $\hbar$.

I^{π}_{m} ($\hbar$)	R_{exp}	R^{f}_{th}	$R^{ABR.}_{th}$	R^{f}_{th-mix}	$R^{ABR.}_{th-mix}$	$R^{2\sigma_f}_{th}$	Ref.
$(9/2^+)$	0.26 ± 0.05	0.86	0.71	0.81	0.65	0.62	this work
$(9/2^+)$	0.29 ± 0.09	-	-	-	-		[Dic15a]
$(25/2^+)$	0.74 ± 0.10	0.11	0.28	0.19	0.35	0.38	this work
$(25/2^+)$	0.71 ± 0.23	-	-	-	-		[Dic15a]
$(31/2^-)$	-	0.05	0.12	0.08	0.20	0.17	this work
$(43/2^+)$	0.081 ± 0.01	-	-	-	-		[Bow13]
$(43/2^+)$	-	0.004	0.03	0.006	0.05	0.06	this work

Table 7.8: Isomer ratio R_{exp} of ^{211}Po compared to analytical calculations R^{f}_{th} and predictions from ABRABLA code $R^{ABRABLA}_{th}$ using the sharp cut-off approach, eq. (3.8) and the spin mixing approach [Gas06].

This calculation shows that the analytical as well as the ABRABLA calculation under estimate the production of high spin isomers. Both angular momentum distributions fail to describe the isomer ratio for the $(25/2^+)\hbar$ and the $(43/2^+)\hbar$ state by more than a factor of 4 to 10. Independent of the calculation of the angular momentum distribution the sharp cut-off approach predicts a lower production of high-spin states as the spin-mixing approach. However all calculations predict a much higher production of the $9/2^+\hbar$ ground state compared to the isomeric states. Combining the spin-mixing approach with the angular momentum distribution arising from the ABRABLA cal-

culation predicts higher isomeric ratios and therefore lower ground state production. It underestimates the isomer production by about a factor of ~ 2. This deviation is similar compared to the isomeric ratios including the broadening of the angular momentum distribution due to the ablation stage developed by Pal and Palit [Pal08]. This last two empirical models describes the experimental isomeric ratios reasonably well, by about a factor 2. However the production of the $9/2^+\hbar$ ground state is overestimated.

These results are in agreement with similar experimental isomeric ratios measurements, e.g. the production of $17\hbar$ and $(43/2)\hbar$ states in ^{214}Ra and ^{215}Ra is underestimated by a factor of 3 to 10 [Pod06, Bow13]. It shows that angular momentum distribution arising from fragmentation is not fully understood and new input from isomer ratio measurements and additional models are needed to understand the mechanism of population of isomeric states and the increase or broadening of the angular momentum distribution from the abrasion to the ablation stage of the fragmentation process. A promising approach calculating the angular momentum distribution of the final fragments directly following in-flight fragmentation seems coupling a microscopic, nucleon-nucleon collision code (IntraNuclear Cascade) [Bou02] to the GEMINI++ evaporation code [Cha88] as shown by Mylaski [Mya12]. This model predicts the population of much higher spin states and therefore might describe the measured isomeric ratios better. Dedicated calculations for the case of ^{238}U fragmentation to ^{211}Po at 1000 MeV/u are beyond the scope of our measurements and are planed for the future.

The combination of alpha spectroscopy and mass spectrometry of thermalized exotic nuclei with gamma spectroscopy methods has shown that it allows for an investigation of the angular momentum distribution following fragmentation with spins between $(9/2^+)\hbar$ to $(43/2^+)\hbar$ of the same fragment. In addition combining the three methods allows the study of isomeric states with short half lifes between 100 ns an 1 ms and long lived states with half lifes above ~ 20 ms. In the future isomeric ratio studies and therefore an investigation of the angular momentum distribution of fragmentation can be carried out at the low energy branch of the Super-FRS at FAIR by combining gamma spectroscopy with high precision mass spectrometry of thermalized exotic nuclei by a cryogenic stopping cell.

8 Outlook and perspectives for FAIR

The usage of a cryogenic stopping cell for the thermalization of exotic nuclei produced by in-flight projectile fragmentation and fission at relativistic energies has been proven to be an efficient and reliable technique. The combination of the FRS fragment separator with the cryogenic stopping cell can be used as a two stage separation and purification system and therefore allows for spectroscopy of exotic nuclei with almost zero back ground. The separation power of the stopping cell can be adjusted by tuning of the operation pressure, by the cost of a reduced stopping efficiency.

During this work several aspects, which are of high importance for the stopping cell of the future low energy branch of the Super-FRS, combining relativistic in-flight production with low-energy precision experiments have been addressed, such as e.g. extraction times, efficiencies, cleanliness of the extracted ion composition and required cleanliness of the stopping cell, charge states of the extracted ion of interest. It was demonstrated that the cryogenic stopping cell technique, i.e. the RF carpet technology, are ready for the low energy branch and that the design of the final cryogenic stopping cell can well be scaled from the current prototype CSC [Dic15c].

The current prototype CSC could reach area densities of up to 6 mg/cm^2 He and reached stopping efficiency of up to $(27 \pm 2.4)\%$ at the FRS. In order to reach stopping efficiencies close to unity at the future low energy branch of the Super-FRS at FAIR more than a factor of 5 in area density is needed compared to the current CSC. Therefore based on the experience gained from the prototype CSC a new design for the final cryogenic stopping cell has been designed and proposed in [Dic15c]. In this design several new concepts such as a two stage extraction, orthogonal extraction, multiple nozzles, a dual layer rectangular RF carpet, segmented anodes and additional detectors for particle identification inside the CSC are incorporated. Thus the future CSC will suite all requirements for successful low energy experiments at the future LEB of the Super-FRS at FAIR.

As an intermediate step towards the future CSC, the prototype CSC can be operated with neon as a stopping gas. Particularly for isotope or isomer search experiments at the current GSI facility operating the prototype CSC with neon as a stopping gas will result in a factor 2.5 more stopping power and therefore for a more efficient isotope search, at the cost of extraction times in the order of $\sim$ 150 ms. The area densities in reach with the prototype CSC and the future CSC are illustrated in figure 8.1. In addition the sigma of the range straggling of monoenergetic beams of ^{78}Ni, ^{132}Sn and ^{208}Pb are shown as a function of energy. The future CSC will allow stopping efficiencies close to unity, except for very light ions.

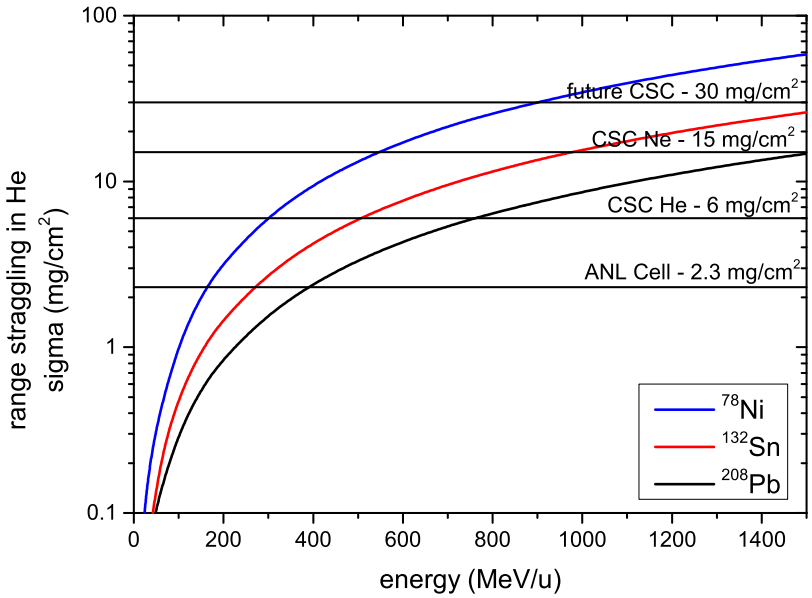

Figure 8.1: Range straggling of a monoenergetic beam of ^{78}Ni, ^{132}Sn and ^{208}Pb in helium as a function of energy. The fraction of the range distribution covered by the area density of the CSC at 6.0 mg/cm^2 helium, the CSC at 15 mg/cm^2 neon equivalent and of the future CSC operated at 30 mg/cm^2. It shows that already the current CSC will provide high stopping efficiencies for heavy fragments.

The potential of the hybrid technique combining in-flight production and separation can be estimated from the production and extraction of ^{211}Po, which was achieved during the 2014 experiment. ^{211}Po was produced by fragmentation of a ^{238}U primary beam on a Be target at 1000 MeV/u. Using the empirical parametrization for fragmentation cross sections EPAX 3.1 ^{211}Po is produced with a cross section of $5.62 \cdot 10^{-2}$ mb [Sue12]. At a total efficiency of $20.2 \pm 3.9\%$ for the stopping and extraction of polonium ions from the cryogenic stopping cell, it was possible to extract during a 12 minute measurement in total $\sim$ 800 ^{211}Po and ^{211m}Po ions into the low energy beam line at a primary beam intensity of $6 \cdot 10^6$ Ions/bunch with a cycle time of the SIS-18 of 6 s.

From the above values the range of expressible exotic nuclei, which can be studied in low energy precision experiments, can be estimated, as indicated in figure 8.2. In the figure the production cross sections for exotic nuclei by fragmentation of a ^{238}U beam on a Be target at 1000 MeV/u along the N=126 neutron shell closure are plotted for the different elements. The cross sections are calculated using the EPAX 3.1 parametrization. The nuclides where experimental mass values are available are indicated, as well as those relying on predictions.

In the near future the SIS-18 will be upgraded to supply up to $1 \cdot 10^{10}$ 1/s ^{238}U for FRS experiments. Assuming similar total efficiencies as achieved during the 2014 experiment of the FRS Ion Catcher the lower limit of the production cross sections in reach can be estimated. Thus the exotic nuclei which should be able to investigate

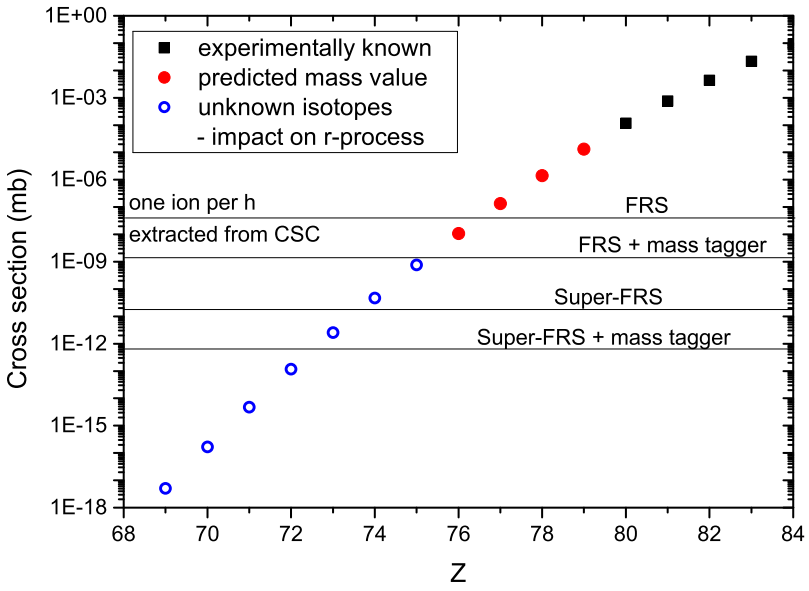

Figure 8.2: Production cross section from EPAX 3.1 [Sue12] for exotic nuclei along the N=126 shell closure produced by in-flight fragmentation of ^{238}U on a Be target at 1000 Mev/u. Indicated are the limit for extracting one ion per hour from the CSC into the low energy beam line. The gain using the mass tagger technique is illustrated for the FRS and for the Super-FRS.

are estimated. In addition the effect of combining the cryogenic stopping cell with the MR-TOF-MS as a mass tagger on the limit of the production cross section is shown in figure 8.2. Using the mass tagger approach for the identification of exotic nuclei allows higher secondary beam rates at the FRS and future Super-FRS while at the same time reducing the sensitivity of the detection.

9 Abstract

High precision experiments and decay spectroscopy of exotic nuclei are of great interest for nuclear structure and nuclear astro-physics. They allow for studies of the nuclear structure far from stability, test of fundamental interactions and symmetries and give important input for the understanding of the nuclear synthesis in the universe.

In the context of this work a second generation stopping cell for the low energy branch of the Super-FRS was commissioned at the FRS at GSI and significant improvements were made to the device. The prototype stopping cell is designed as a cryogenic stopping cell (CSC), featuring enhanced cleanliness and high area density. The CSC was brought into full operation and its performance characteristics were investigated including the maximal area density, extraction times, cleanliness and extraction efficiencies. In three commissioning experiments at the current GSI FRS facility in 2011, 2012 and 2014 up to 22 isotopes from 14 elements produced by in-flight projectile fragmentation and fission of ^{238}U could be thermalized and extracted with high efficiency. For the first time projectile and fission fragmentation produced at 1000 MeV/u could be thermalized in a stopping cell and provided as a low-energy beam of high brilliance for high precision experiments.

The technical improvements of the CSC, such as an improved RF carpet, new cryocooler-based cooling system, a monitoring system of the cleanliness and the high density operation, made it possible to thermalize heavy ^{238}U projectile fragments with total efficiencies of about 20% in the 2014 experiment. In addition the improvements lead to an increase in the stability and reliability of the CSC and the performance of the CSC during online experiments at the FRS Ion Catcher showed that the utilized techniques are ready for the final CSC for the low-energy branch of the Super-FRS at FAIR.

The CSC was operated with an area density of up to 6.3 mg/cm^2 helium during online experiments, which is about three times larger than any stopping cell, using RF structures for the extraction of ions, has demonstrated. The area density and therefore the stopping power of the CSC is limited by the differential pumping. To overcome this limitation the CSC was tested with neon as a stopping gas with area densities of up to 11.3mg/cm^2 helium equivalent, demonstrating a unprecedented area density for stopping cells based on RF structures. The RF carpet performed reliably and its potential for the future FAIR stopping cell was shown.

During the experiments at GSI the mean extraction time of ^{221}Ac ions from the CSC to a silicon surface detector was measured, it amounts to 24 ms. This value is well in

agreement with offline measurements using a pulsed ^{223}Ra recoil ion source.

The combination of a high density stopping cell with high total efficiencies and a non-scanning high-resolution mass spectrometer can be used as an independent identification detector for exotic nuclei by their mass, allowing a recalibration of the in-flight detectors of any fragment separator. As a proof-of-principal experiment the CSC and a MR-TOF-MS have been used as a mass tagger for the FRS at GSI. ^{134}I ions were produced by in-flight fission from an ^{238}U primary beam at 1000 MeV/u and identified by the mass tagger. The new method does not rely on specific decay properties and therefore allows a recalibration of the fragment separator independent of the fragment and can also be used with stable nuclides. The usage of the CSC and a MR-TOF-MS will allow fast recalibration and a more effective usage of the limited amount of beam time for all experiments with exotic nuclei even in the case the nuclide of interest is not clearly identified by the in-flight detection scheme. In addition the mass tagger allows higher secondary beam rates at the current FRS, while at the same time increasing the sensitivity for exotic nuclei.

The high performance characteristics of the CSC allowed low energy experiments such as high-precision mass measurements and decay spectroscopy, the half lifes of ^{221}Ac and ^{223}Th have been measured, alpha spectroscopy of short lived nuclides (^{220}Ra, 17.9 ms) were performer. Due to the selective stopping of only one nuclide in the stopping cell the characteristic alphas of 24 nuclides were measured with almost zero background and their Q_α-values could be confirmed.

Following a new approach, data from gamma spectroscopy, alpha spectroscopy and high resolution mass spectrometry of ^{211}Po were combined to study the angular momentum distribution arising from in-flight projectile fragmentation. This was possible by measuring the isomer ratio of ^{211}Po and comparing it to current predictions from the two-step abrasion-ablation model. It was shown that current models can not describe the angular momentum distribution of in-flight projectile fragmentation and that new measurements of isomer ratios are required in order to understand the angular momentum distribution.

Zusammenfassung

Präzisionsmassenmessungen und Zerfallsspektroskopie an exotischen Kernen sind für die moderne Kernphysik von großem Interesse. Sie geben Aufschluss unter anderem über die Schalenstruktur fernab der Stabilität, fundamentale Wechselwirkungen und Symmetrien und stellare Nukleosyntheseprozesse.

Im Rahmen dieser Arbeit wurde eine kryogene Stoppzelle (CSC) vollständig in Betrieb genommen, weiterentwickelt und ihrer Leistungsfähigkeit untersucht, welche die Vorteile der ISOL Methode an der in-flight Beschleunigeranlage GSI zur Verfügung stellt.

An der aktuellen GSI Beschleuniger-Anlage, sowie in Zukunft an der FAIR Beschleuniger-Anlage, können Ionenstrahlen aller Element produziert werden. Hier stellt die kryogene Stoppzelle einen einmalige Möglichkeit dar, Präzisionsexperimente an Nuklide, die für den dritten r-Prozess Peak wichtig sind, durchführen zu können. Vor allem die niederenergie Experimente MATS (Precision Measurements of very short-lived nuclei using an Advanced Trapping System for highly charged ions) und LaSpec (LAser SPECtroscopy) benötigen niederenergetische Ionenstrahlen mit kleiner Emittanz.

Die kryogene Stoppzelle wurde während drei Teststrahlzeiten in 2011, 2012 und 2014 an der GSI Beschleunigeranlage als Teil des FRS Ion Catcher Experiments erprobt. Der FRS Ion Catcher fungiert als ein Prototyp für den zukünftigen Low Energy Branch (LEB) des Super-FRS. Erstmals konnten relativistisch produzierter ^{238}U Projektil- und Spaltfragmente mit hoher Gesamteffizienz abgestoppt, thermalisiert und zu einem niederenergetischen Ionenstrahl geformt werden. Es wurden vielfältige Verbesserungen an dem System durchgeführt, z.B. die Überarbeitung der RF-Carpet Elektronik sowie die Umstellung der Kühlung des Systems von flüssigem Stickstoff auf einen externen Kryostaten. Alle diese Maßnahmen haben zu einer Steigerung des Leistungsvermögens (Stopp- und Extraktionseffizienz) und der Zuverlässigkeit der CSC geführt. Eine verbesserte Stabilität des Betriebs der Stoppzelle erlaubten erfolgreiche Experimente am FRS Ion Catcher.

Die Stoppzelle wurde dabei mit einer Flächendichte von bis zu 6.3 mg/cm^2 Helium betrieben. Das ist mehr als das Dreifache, was bisher mit einer RF-basierenden Stoppzelle erreicht werden konnte. Durch die hohe Flächendichte ließen sich Stoppeffizienzen von bis zu 27% für ^{223}Th Projektilfragmente erzielen. Durch die Verbesserungen der Sauberkeit der kryogenen Stoppzelle ergaben sich sehr hohe Extraktionseffizienzen von ungefähr 80%. Weiterhin konnten die exotischen Kerne als reine Strahlen, teilweise auch als doppelt geladene Ionen und ohne Addukte extrahiert wer-

den. Dadurch konnten sie erfolgreich für hochauflösende Massenspektroskopie und Zerfallsspektroskopie bereit gestellt werden. Aus der Kombination von hoher Stopp- und Extraktionseffizienz ergaben sich Gesamteffizienzen von bis zu 20%.

Die Flächendichte und somit das Stoppvermögen der CSC war durch das differentielle Pumpen limitiert. Um das Verhalten des RF-Carpets bei höheren Dichten zu testen, wurde Neon als Stoppgas eingesetzt. Der Einsatz von Neon erlaubte den erfolgreichen Betrieb bei Flächendichten, die für Helium dem von 11.3 mg/cm^2 entsprechen. Dies entspricht fast dem Sechsfachen, was mit RF-basierten Stoppzellen bisher erreicht werden konnte. Der Betrieb des RF-Carpets bei diesen hohen Drücken zeigt das Potential der Technik für den Einsatz am zunünftigen LEB des S-FRS. Weiterhin ermöglicht ein Betrieb der kryogenen Stoppzelle mit Neon eine Steigerung des Stoppvermögens, was in der Zukunft bei Experimenten zur Isotop- oder Isomersuche eine Effizienzsteigerung bewirken kann.

Die mittlere Extraktionszeit von exotischen Ionen aus der Stoppzelle bis zu einem Halbleiter Detektor wurde für ^{221}Ac Ionen bestimmt und beläuft sich auf 24 ms. Dies konnte zusätzlich in offline Experimenten bestätigt werden.

Die Kombination aus einer Stoppzelle mit einer hohen Flächendichte und einem sensitiven, nicht scannenden, hochauflösenden Multireflektions Flugzeitmassenspektrometer (MR-TOF-MS) erlaubt eine direkte Identifikation von exotischen Kernen anhand ihrer Masse. Der Einsatz der CSC und eines MR-TOF-MS als sogenannter Mass-Tagger, ermöglicht eine Identifikation der Ionen und somit eine Kalibration der Detektoren zur Teilchenidentifikation Im-Fluge am FRS. Diese Methode ist deutlich flexiebler als die bisherigen Verfahren und erlaubt eine viel effizientere Nutzung von Strahlzeiten für fast alle Experimente am FRS und zukünftigem Super-FRS, da sie nicht auf Zerfällen basiert und somit für alle Nuklide verwendet werden kann. Weiterhin können dadurch auch Nuklide identifiziert werden, die in der Identifikation Im-Fluge nicht aufgelöst werden können. Das Konzept wurde erfolgreich mit der Identifikation von ^{134}I am FRS Ion Catcher gezeigt.

Das hohe Leistungsvermögen erlaubte eine Vielzahl an Messungen an über 22 Isotopen von 14 Elementen. Unter anderem wurde die Lebensdauer von ^{221}Ac und ^{223}Th mittels Zerfallsspektroskopie gemessen sowie Experimente mit extrem kurzlebigen Nukliden durchgeführt (^{220}Ra, 17.9 ms Halbwertszeit). Hierbei wurde selektives Abstoppen von Nuklieden in der Stoppzelle als zusätzliche Separation nach der Separation Im-Fluge eingesetzt. Dies erlaubte Alpha Zerfallsspktroskopie mit fast isotopenreinen niederenergetischen Ionen und somit die Bestimmung der Q-alpha Energien von 19 Nukliden.

Die Alpha Energien von 24 Zerfällen konnten bestätigt und der Fehler des Q-alpha Wert von ^{221}Ac verbessert werden.

Weiterhin erlaubte die kryogene Stoppzelle Experimente zum Isomer zu Grundzustandsverhältnis von ^{211}Po und somit eine Überprüfung der Drehmomentverteilung bei der Fragmentation von ^{238}U bei relativistischen Energien. Das Isomerenverhältniss

wurde mit Vorhersagen verglichen. Dies zeigte, dass aktuelle Modelle zur Bevölkerung von angeregten Kernzuständen dieses nicht ausreichend beschreiben und Abweichungen bis zu einem Faktor 4 bis 10 vorliegen können. Modelle, die eine empirische Verbreiterung der Drehmomentverteilung während der Kernabregungsphase des Fragmentationsporzesses annehmen, beschreiben die gemessenen Isomer zu Grundzustandsverhältnis deutlich besser.

Alle durchgeführten Konzeptexperimente zeigen, dass durch die kryogene Stoppzelle neue Experimente an exotischen Kernen ermöglicht werden, die bisher nicht erreichbar waren, bzw. nicht produziert werden konnten. Für FAIR ist die Stoppzelle das Schlüsselsystem für den LEB, speziell die Experimente MATS und LaSpec sind ohne eine kryogene Stoppzelle nicht denkbar.

Acknowledgements

At this point it is a pleasure to thank those who contributed to this thesis either by scientific or personal support, in specific the full FRS Ion Catcher collaboration.

I am grateful to professor Dr. Christoph Scheidenberger and Dr. Dr. Hc Hans Geissel for having me in their research group and giving me the possibility to work on the cryogenic stopping cell. I enjoyed working together with you on the data analysis of the online experiment and I am thankful for your personal support.

I want to thank Dr. Timo Dickel for his supervision of my work and for the long discussions and conversations not only about stopping cells, carpets, etc., which typically just started with an easy question. Thank you for listening to my concerns and for your help during my thesis. I also want to acknowledge the guidance of Dr. Wolfgang Plaß, you recommendations on the interpretation of data was always very welcome.

I would like to offer my special thanks to Dr. Sivaji Purushothaman for all those hours we worked together in the labs at GSI and for your personal support during the last years.

I am particularly grateful for the assistance given by Dr Stephane Pietri concerning isomers and their production and by Dr. Aleksandra Kelic-Heil for contributing the calculations of the angular momentum distribution. The advices given by Dr Emma Haettner have been a great help during setting up of the RFQs and working together with you on the efficiencies was a pleasure. I wan to thank the FRS Ion Catcher daily crew, Ann-Kathrin Rink, Christine Hornung, Ivan Miskun, Jens Ebert, Samuel Ayet, for the good working environment and nice discussions during measurement plans or pumping of the system. Samuel with out your contribution there would have not been any operational RF carpet. In addition I want to thank all present and former members of the Giessen group (only to name a few Christian Jesch, Florian Greiner, Johannes Lang, Julian Bergmann, Marcel Diwisch, Wayne Lippert) and of the FRS group at GSI for their help during my work and in specific during the FRS Ion Catcher experiments at GSI. In addition I want to thank Christa Momberger and Evelin Prinz for taking care of all smaller and bigger things around and keeping the university bureaucracy as far as possible from us. A big thank you goes to the team of the technical workshop in Giessen and GSI.

Last but not least I want to thank my family, by blood or choice, my parents Sigrid and Gerald Reiter for their endless support during all those years and Simon Reiter for being my brother and my friend. Thank you.

Bibliography

[Ani03] Vincent G. Anicich, An Index of the Literature for Bimolecular Gas Phase Cation-Molecule Reaction Kinetics, NASA JPL Publication 03-19 (2003).

[Aje14] Samuel Ayet San Andres, RF Carpet for the Cryogenic Stopping Cell, GSI Internal Report (2014).

[Arj81] J. Arje, K. Valli, Nucl. Instr. Meth. 179 (1981) 533.

[Arj85] J. Arje, J. Ayst, H. Hyvnen, et al., Physical Review Letters 54 (1985) 99.

[Ast20] F. W. Aston, Isotopes and atomic weights, Nature, 105(2646) (1920) 617-619.

[ATIMA] ATIMA, Atomic Interaction with Matter, https://web-docs.gsi.de/ weick/atima/.

[Bar63] W. H. Barkas, J.N. Dyer, H. H. Heckman, Resolution of the Σ^--Mass Anomaly, Phys.Rev. Lett. 11 (1963) 26.

[Bar74] A. R. Barnett and J. S. Lilley, Phys. Rev. C 9, (1974) 2010.

[Bat67] G. K. Batchelor, An Introduction to Fluid Dynamics, Cambridge University Press (1967) ISBN 0 521 66396 2.

[Ben80] P. D. Bentley, The modern cryopump, Vacuum, vol. 30 num. 4/5, 0042-207X/80/0501-0145$02.00/0 (1980).

[Bet30] H. A. Bethe, Ann. Phys. 5 (1930) 325.

[Bet32] H. A. Bethe, Z. Phys. 76 (1932) 293.

[Bet36] H. A. Bethe and R. F. Bach, A stationary states of nuclei, Rev. Mod. Phys., 8 (1936) 82.

[Boh13] N. Bohr, Phil. Mag. 25 (1913) 10.

[Bor70] J. Borggreen et al., Production and Decay Properties of Protactinium Isotopes of Mass 222 to 225 Fromed in Heavy-Ion Reactions, Phys. Rev. C 1841 (1970).

[Bou02] A. Boudard et al., Phys. Rev. C. 66, (2002) 044615.

[Blo33] F. Bloch, Ann. Physik 5 (1933) 285.

[Blu13] Y. Blumenfeld, T. Nilsson and P. Van Duppen, Facilities and methods for radioactive ion beam production, Physica Scripta, T152 (2013) 014023.

[Bow73] J. D. Bowman, W. J. Swiatecki and C. E. Tsang, LBL-2908 (1973), UNCLAS Reprint

[Bow13] M. Bowry et al., Populatin of high-spin isomerc states following fragmentation of 238U, Phys. Rev. C, 024611 (2013).

[Bra36] N. E. Bradbury, R. A. Nielson, Absolute values of the electron mobility in hydrogen, Phys. Rev. 49 (1936) 388-393.

[Car02] D. Caraman and D. K. Bohme, Periodic trends in reactions of benzene clusters of transition metal cations, M(C6H6)1.2 with molecular oxygen, J. Phys. Chem. A, 106 (2002) 9705-9717.

[CDR] FAIR CDR, An International Accelerator Facility for Beams of Ions and Antiprotons, Conceptual Design Report, (2001).

[Cha88] R. J. Charity et al., Nucl. Phys. A476, 516 (1988).

[CIGRE] CIGRE-Symposium S05-87, Vienna/Austria, (1987), pp. 100-04/1-04/4.

[Cor97] H. H. Cornehl et al., A comparative study of oxoligand effects in the gas-phase chemistry of atomic lanthanide and actinide cations, Chem. Eur. J., 3 (1997) 1083-1090.

[Dan74] H.Daniel, Beschleuniger, Teubner Studierbücher (1974).

[Daw76] P. H. Dawson, Quadrupol Mass Spectrometry and its application time-of-flight mass specrometer, Rapid Commun. Mass Specrom., 3(5):155-159 (1976).

[Deh67] H. G. Dehmelt, Radiofrequency spectroscopy of stored ions I: STORAGE, ADV. AT. MOL.PHYS., 3:53-72 (1967).

[Den06] P. Dendooven, S. Purushothaman, K. Gloos, On a cryogenic noble gas ion catcher, Nucl. Inst. Meth. A 588 (2006) 580-583, (2006).

[Dic10] T. Dickel, Design and Commissioning of an Ultra-High-Resolution Time-of-Flight Based Isobare Separator and Mass Spectrometer, PhD thesis, Justus-Liebig-University Giessen (2010).

[Dic15a] T. Dickel et al., First spatial separation of a heavy ion isomeric beam with

a multiple-reflection time-of-flight mass spectrometer, Physics Letters B Volume 744, 11 May 2015, Pages 137-141 (2015).

[Dic15b] T. Dickel et al., A high-performance multiple.reflectioni time-of-flight mass spectrometer and isobar separator for the research with exotic nuclei, Nucl. Inst. and Meth. A 777 (2015) 172-188.

[Dic15c] T. Dickel et al., A Novel Next-Generation Cryogenic Stopping Cell for the Low-Energy Branch of the Super-FRS, EMIS Proceedings, Nucl. Instrum. Methods B, submitted (2015).

[Dro14] C. Droese et al., The cryogenic gas stopping cell of SHIPTRAP, Nuc. Inst and Meth B, 338 (2014) 126-138.

[Don97] A. Dononov et al., A new technik for decomposition of selected ions in a molecular ion reactor coupled with ortho-time-of-flight mass spectrometry, Rapid Commum. Mass Spectrom.,11:1649-1656 (1997).

[Eis54] Y. Eisenberg, Phys. Rev. 96 (1954) 1378.

[ElL87] A. M. Y. El-Lawindy et al., Low-lying structure of 215-Rn and 219-Ra, J. Phys. G: Nucl. Phys. 13 (1987) 93-101.

[FAIR] FAIR Baseline Technical Report, http://www.gsi.de/fair/reports/btr.html.

[ITAG] F. Farinon et al., GSI internal report: ITAG Manual, (2010).

[Far11] F. Farinon et al., Development and test of an alpha-tagger detector at the FRS, GSI Scientific Report 2011, PHN-NUSTAR-FRS-06 (2011).

[Fer40] E. Fermi, The ionization loss of energy in gases and in condensed materials, Phys. REv. 57 (1940) 485.

[Fic55] A. Fick, Ann. Der. Physik, 94,59. (1855) DOI: 10.1002/andp.18551700105.

[For99] B. Fornal et al., Spectroscopy at the neutron-rich edge of beta-stability valley, Acta Physica Polonica B, Vol. 30 (1999) 1219.

[Gam30] G. Gamow. Mass defect curve and nuclear constitution, Proc. R. Soc. London, 126(803):632-6444 (1930).

[Gai91] L. F. Gaimard and K.-H. Schmidt, Nucl. Phys. A 531 (1991) 709.

[Gar80] R. P. Gardner, K. Verghese and H.-M. Lee, The Average Solid Angle Subtended by a Circular Detector Coaxial to a Circular Isotropic Source, Nucl. Instrum. Methods 176 (1980) 615-617.

[Gas06] L. R. Gasques et al., Isomer ratio measurements as a probe of the dynamics of breakup and incomplete fusion, Phys. Rev. C, 064615 (2006).

[Gei89] H. Geissel, Th. Schwab, P. Armbruster, J.P. Dufour, E. Hanelt, K.-H. Schmidt, B. Sherrill and G. Münzenberg, Ions penetrating through ion-optical systems and matter - non liouvillian phase-space modelling, Nucl. Inst. Meth. B, 7(1992)71 (1989)

[Gei92] H. Geissel et al., The GSI projectile fragment separator (FRS): a veritile magnetic system for relativistic heavy ions, Nucl. Inst. Meth. B,70 (1992) 286.

[Gei95] H. Geissel, G. Müenzenber, Secondary Exotic Nuclear Beams, Annu. Rev. Nucl. Part. Sci., (1995) 45:163-203.

[Gei03] H. Geissel, The Super-FRS project at GSI, Nucl. Inst. Meth. B 204 (2003) 71-85.

[Gei14] H. Geissel, M. Huyse, G. Münzenberg and P. Van Duppen, Exotic Nuclear Beam Facilities, Volume 1. Wiley, (2014).

[Gerh98] J. Gerhold, Properties of cryogenic insulants, Cryogenics 38 (1998) 1063-1081 PII: S0011-2275(98)00094-0.

[Gerl92] D. Gerlich, State Selected and State-to State Ion-Molecule Reaction Dynamics, Part 1. Experiment, Vol. LXXXII, C.Y. Ng. M Bear (Eds.), Wiley, New York(1992).

[Gre14] F. Greiner, Bachelor Thesis, Justus-Liebig-University Giessen (2014).

[Gol74] A. S. Goldhaber, Phys. Lett. B 53 (1974) 306.

[Hea11] E. K. Heattner, A novel radio frequency quadrupole system for SHIPTRAP and New Mass measurements of rp nuclids, Phd Thesis, JLU Giessen (2011).

[Huy02] M. Huyse et al., Nucl. Instrum. Methods B 187 (2002) 535.

[Hof79] S. Hofmann et al., Alpha decay studies of very neutron deficient isotopes of Hf, Ta, W, and Re., Z. f. Phys., A291 (1979).

[Hue75] J. Hüfner, K. Schäfer and B. Schürmann, Phys. Rev. C 12 (1975) 1888.

[Hui04] J. Huikari et al., Production of neutron deficient rare isotope beams at IGISOL; on-line and off-line studies, Nucl. Inst and Meth B, 222 (2004) 632-642.

[Huy88] M. Huyse et al., Production and Mass Separation of Short-Living Neutron-Deficient Actinides, Nucl. Instrum. Methods B 31 (1988) 483-486.

[Huy04] M. Huyse, The Why and How of Radioactive-Beam Research, The Euroschool Lectures on Physics with Exotic Beams, Vol. I, DOI 10.1007/b98790, (2004).

[ISOLDE] ISOLDE yield database.

[Iwa97] N. Iwasa, et al., Nucl. Instrum. Methods B 126 (1997) 284.

[Iwa11] N. Iwasa, et al., Nucl. Instrum. Methods B 269 (2001) 752-758.

[Jan11] R. Janik et al., Nucl. Instrum. Methods A 640 (2011) 54.

[Jav97] G. Javahery and B. Thomson, A segmented radio-frequency-only quadrupole collision cell for measurments of ion collision cross section on a triple quadrupole mass spectrometer, J. Am. Soc. Mass Spectrom., 8 (1997) 697-702.

[Jen54] W. Jentschke, A. C Juveland, and G. H Kinsey, Alpha-Emitting Isomer Polonium 211, Phys. Rev. 96 (1954) 231.

[Jes08] C. Jesch Injektions-Ionenfallensystem für ein Multireflektions-Flugzeitmassenspektrometer, Diploma thesis, Justus-Liebig-Universität Gießen (2008).

[Jes15] C. Jesch et all, The MR-TOF-MS isobar separator for the TITAN. facility at TRIUMF, Proceedings TCP 2014, Hyperfine Interact DOI 10.1007/s10751-015-1184-2 (2015).

[Jon97] M. de Jong, A. V. Ignatyuk, K.-H. Schmidt, Nucl. Phys. A 613 (1997) 435-444.

[Kel15] A. Kelic-Heil, private communication (2015).

[Kox01] G. K. Koyanagi et al., Oxidation reactions of lanthanide cations with N2O and O2 periodicities in reactivity, J. Phys. Chem. A, 105 (2001) 9410-9414.

[Koy02] G. K. Koyanagi et al., Gas-Phase reactions of transition-metal ions with molecular oxygen: room-temperature kinetics and periodicities in reactivity., J. Phys. Chem. Am 106, (2002) 4581-4590.

[Kra14] A. Kramida,Â Yu. Ralchenko,Â J. Reader,Â and NIST ASD Team, NIST Atomic Spectra Database (ver.5.2) (2014).

[Kud89] H. Kudo, T. Nomura, K. Sieki et al., Isomeric transitions of 211m-Po and 212m-Po and E4 effective charge, Nucl. Phys. A 494 (1989) 203-213.

[Kud01] Yu. Kudryavtsev et al., A gas cell for thermalizing, storing and transporting

radioactive ions and atoms. Part I: Off-line studies with a laser ion source., Nucl. Instrum. Methods B 179 (2001) 412-435.

[Lin63] J. Lindhard, A. Winther, K. Dan. Vidensk. Selsk. Mat. Fys. Medd. 34(1964) No. 4.

[Lin76] J. Lindhard, The Barkas Effect - or Z_1^3, Z_1^4-Corrections to stopping of swift charged particles, Nucl. Inst. and Meth. 132 (1976)1.

[Lin96] J. Lindhard, A. H. Sørensen, Relativistic theory of stopping for heavy ions, Phys. Rev. A 53 (1996) 2443.

[Liv69] J.Livinggood, The Optics of Dipole Magnets, Acadeimic Press (1969).

[Lob00] A. Loboda, A. Krutchinsky, O. Loboda, J. McNabb, V. Spicer, W. Ens and K. Standing, Novel linac II electrode geometry for creating an axial field in a multipole ion guide. Eur. J. Mass Spectrom., 6:531-536 (2000).

[Lun03] D. Lunney, J. M. Pearson and C. Thibault, Recent trends in the determination of nuclear masses, Rev. Mod. Phys., 75(3):1021-1062 (2003)

[Mas88] E.A. Mason and E.W. McDaniel, Transport properties of ions in gases, John Wiley & Sons, New York (1988).

[Mas70] S. Masuda, K. Fujibayashi, J. I. E. E. Jpn. 90 (1970) 1.

[May79] T. Mayer-Kuckuk, Kernphysik, Teubner Studienbücher Physik, 3. Auflage, Kapitel 6.7, p 222(1976).

[McG1998] T. R. McGoram et al., High-spin isomers in 211Po and related structures in 210Po and 212Po, Nucl. Phys. A 637 (1998)469-490.

[Mis14] I. Miskun et al., An RFQ based beam line and mass filter to improve identification capabilities at the diagnostics unit of the prototype CSC for the LEB, GSI annual report (2014).

[Mis15] I. Miskun, Diplomathesis (2015).

[Møe32] C. Møller, ann. Phys. 14 (1932) 531.

[Moi12] M. Moisan, J. Pelletier, Physics of Collisional Plasmas, DOI 10.1007/978.94.007.4558.2_2, (2012).

[Mor92] Y. Moriwaki, M. Tachikawa, Y. Maeno and T. Shimizu, Collision cooling of ions stored in quadrupol radio-frequency trap. Jpn, J, Appl. Phys., 31:1640-1643 (1992).

[Moo08] I. D. Moore, Nucl. Instrum. Methods B 266 (2008) 4434.

[Mot29] N. F. Mott, Proc. Roy. Soc. London A 124 (1929) 425.

[Mot32] N. F. Mott, Proc. Roy. Soc. London A 135 (1932) 429.

[Mya12] S. Myalski et al., Acta. Phys. Polonica B No 2. Vol. 43 (2012) 253.

[Neu06] J. B. Neumayr et al., The ion-catcher device for Shiptrap, Nucl. Inst. Meth. B 244 (2006) 489-500.

[Oli1979] L. F. Oliveira, R. Donangelo and J. O. Rasmussen, Phys. Rev. C 19 (1979) 826.

[Pal08] S. Pal abd R. Palit, Angular momentum population in fragmentation reactions, Phys. Lett. B 665 (2008) 164.

[Pas89] F. Paschen, Über die zum Funkenübergang in Luft, Wasserstoff und Kohlensäure bei verschiedenen Drucken erforderliche Potentialdifferenz. Ann. Phys., 273: 69-96. doi: 10.1002/andp.18892730505 (1889)

[Pau53] W. Paul and H. Steinwedel. Ein neues massenspektrometer ohne magnetfeld. Z. Naturforschung, 8a:448-451, (1953).

[Pet04] Petrovic and Maric in Lieberman, M. A., & Lichtenberg, A. J. (2005). Principles of plasma discharges and materials processing. Hoboken, N.J: Wiley-Interscience. 2nd Edition Table 14.1 on Page: 546 (2004)

[Pet08] M. Petrick et al., Online test of the FRS Ion Catcher at GSI, Nucl. Inst. Meth. B 266 (2008) 4493-4497 (2008).

[Pet08b] M. Petrick, Aufbau und Erprobung einer neuartigen Separationsmethode für exotische Kerne bei relativistischen Energien, Phd Thesis, JLU-Giessen (2008).

[Per62] I. Perlman et al., Isomeric State of Po212, Phys. Rev. vol. 127 nu. 3 (1962) 917-922.

[Pfu94] M. Pfützner et al., Nucl. Inst. Meth. B 86 (1994) 213.

[Pie15] S. Pietri, private communication (2015).

[Pla01] W. R. Plaß, The dependence of RF ion trap mass spectrometer performance on electrode geometry and collisional processes, PhD thesis, Justus-Liebig-University Giessen (2001).

[Pla07] W. R. Plaß et al., An RF quadrupole-time-of-flight system for isobar-separatin

and multiplexed low energy rare-isotope beam experiments, Eur. Phys. J. Special topics 150 (2007) 367-368.

[Pla08] W. R. Plaß et al., Isobar separation by time-of-flight mass spectrometry for low-energy radioactive ion beam facilities, Nucl. Instr. Meth. B 266 (2008) 4560-4564.

[Pla13b] W. R. Plaß et al., Multiple-reflection time-of-flight mass spectrometry. Int. J. Mass Spectrom. (2013)

[Pla13a] W.R. Plaß et al., Nucl. Inst. Meth. B, 317 (2013) 457-462.

[Pla15] W. R. Plaß et al., Physica Scripta, in print (2015).

[Pod06] Zs. Podolyak et al., High angular momentum states populated in fragmentation reaction, Phys. Let. B vol. 632 (2006) 203-206.

[Pur13] S. Purushothaman et al., EPL 104 (2013) 42001.

[Ram59] W. J. Ramler et al., Phys. Rev. 114, 154 (1959).

[Ran11] M. Ranjan et al., New stopping cell capabilities: RF carpet performance at high gas density and cryogenic operation, (2011).

[Ran12] M. Ranjan, Design and Characterization of a Cryogenic Stopping Cell for Radioactive Ions, PhD thesis, University of Groningen (2012).

[Ran14] M. Ranjan et al, Design, construction and cooling system performance of a prototype cryogenic stopping cell for the Super-FRS at FAIR, Nuclear Instruments and Methods in Physics Research A 770 (2015) 87-97.

[Rei11] M.P.Reiter, Master Thesis JLU-Giessen (2011).

[Rei15] M. P. Reiter et al., Rate Caoabilitdy of a Cryogenic Stopping Cell for Uranium Projectile Fragments Produced at 1000 MeV/u, EMIS Proceedings, Nucl. Instrum. Methods B, submitted (2015).

[Rin12] A.-K. Rink, Eine Laserablations Ionenquelle zur Charakterisierung des FRS Ion Catchers, Master Thesis, Justus-Liebig-University Giessen (2012).

[Rod10] D. Rodrigeuz et al, MATS and LaSpec: High-precision experiments using ion traps and lasers at FAIR, Eur. Phys. J. Special Topics 183, 1-123 (2010).

[Rud79] M. A. Rudat and G. H. Morrison, Detector Discrimination in SIMS II. Ion-to-Electron Converter Yield Factors for Negative Ions, Int. J. Mass Spectrom. Ion Phys. 29 (1979) 1-9.

[Sav01] G. Savard et al., Hyp. Int. 132 (2001)223.

[Sav03] G. Savarda et al,, Development and operation of gas catchers to thermalize fusion evaporation and fragmentation products, Nucl. Inst. Meth. B: Beam, 204, pp. 582-586 (2003)

[Scha10] D. Schäfer, Design and simulation of a cryogenic stopping cell for the low-energy branch of the Super-FRS at FAIR, Diploma Thesis (2010)

[Sche94] C. Scheidenberger, H. Geissel, et al., Direct Obervation of Systematic Deviations from the Bethe Stopping Theroy for Relativistic Heavy Ions, Phys. Rev. Lett. 73 (1994) 50.

[Sche98] C. Scheidenberger, H. Geissel, Penetration of relativistic heavy ions through matter, Nucl. Inst. Meth. B 135 (1998) 25-34.

[Sche03] C. Scheidenberger et al., Energy and range focusing of in-flight separated exotic nuclei - A study for the energy-buncher stage of the low-energy branch of Super-FRS.

[Schm93] K.-H. Schmidt, T. Brohm et al., Phys. Lett. B 300 (1993) 313.

[Smi02] M. A. Smith et al., HOC^++H2 isomerization rate at 25 K : implications for the observed $[HCO^+]/[HOC^+]$ ratios in the interstellar medium, Astrophys. J., 578 (2002) L87-L90.

[Sof77] C. J. Sofield et al., Energy straggling of 5.486-MeV alpha particles in Al, Phys. Rev. A 15 (1977) 2221.

[Schw03] S. Schwarz et al., Nucl. Instrum. Methods B, 204 (2003) 507.

[Sim88] D. A. Dahl, J. E. Delmore, The SIMION PC Users Manual, Idaho National Engineering Labratory (1988).

[Sim08] A. Simon. Entwickung und Test eines CFK-basieren RF-Quadrupols fuer ein Multireflektions-Flugzeitmassenspektrometer, Bachelor thesis, Justus-Liebig-University Giessen, (2008).

[Sod17] F. Soddy. The complexity of the chemical elements. Nature, 99:433-438, (1917).

[Spi53] F. N. Spiess, Alpha-Emitting Isomer: Polonium-211, Phys. Rev. 94, 1292 (1954).

[Ste71] R. M. Sternheimer, R. F. Peierls, General expression for the density effect for the ionization loss of charged particles, Phys. Rev. B 3 (1971) 3681.

[Sue12] K. Sümmerer, Improved Empirical Parametrization of Fragmentation Cross Sections, arXive: 1205.5436v2 [nucl-ex] 20 Jun 2012 (2012).

[Tak05] A. Takamine et al., Rev. Sci. Instrum. 76 (2005) 103503.

[Tak07] A. Takamine et al., Improvement of the slow ri beam transport using carbon-OPIG, RIKEN Accel. Prog. Rep., 40 (2007).

[Tol97] A. V. Tolmachev et al., A collisional fucusing ion guide for coupling an atmospheric pressure ion source to a mass spectrometer, Nucl. Instrum. Methods. B.124 (1997) 112-119.

[Tol00] A. V. Tolmachev et al., Simulation-based optimization of the electrodynamic ion funnel for high sensitivity electrospary ionization mass spectrometry, Int. J. Mass Spectrom. 203 (2000) 31-47.

[Tov58] P. A. Tove et al., Alpha-Emitters with short half-life induced by protons on heavy elements, Arkiv Fysik 13 (1958) 549.

[Val70] K. Valli et al., Pdorduction and Decay Properties o Thorium Isotopes of Mass 221-24 Formed in Heavy-Ion Reactions, Phys. Rev. C, 1 (1970) 2115.

[Vie95] L. A. Viehland, E.A. Mason, Transport Properties of Gaseous Ions over a Wide Energy Range, IV, Atomic Data and Nuclear Data Tables, 60 (1), pp. 37-95. (1995).

[Vie12] L. A. Viehland, Zero-field mobilities in helium: highly accurate values for use in ion mobility spectrometry, Int. J. Ion Mobil. Spec. (2012) 15:21-29.

[Vla95] P. R. Vlasak, D. J. Beussman et al., An interleaved comb ion deflection gate for m/z selection in time-of-flight mass spectrometry, Rev. Sci. Instrum. 67 (1996) 1.

[Wad01] M. Wada, et al., Riken Accel. Prog. Rep 34 (2001) 202.

[Wad03] M. Wade, et al., Slow RI-beams from projectile fragmentation seperators, Nucl. Inst. Meth. B204,507(2003).

[Wad13] M. Wada, Nuclear Instruments and Methods in Physics Research Section B 317 (2013) 450.

[AME2012] M. Wang, G. Audi et al., The AME 2012 atomic mass evaluation, CPC(HEP and NP), 36(12):1603-2014 (2012).

[Web94] M. Weber et al., Nucl. Phys. A 578 (1994) 659.

[Wei00A] H Weick et al., Nucl. Instrum. Methods B, 164-165 (2000) 168.

[Wei00B] H. Weick et al., Phys. Rev. Lett 85 (2000) 2725.

[Wei02] H. Weick, A. H. Sørensen et al., Nucl. Instrum. Methods B. 193 (2002) 1.

[Wei04] L. Weissmann et al., First extraction test of the NSCL gas cell, Nucl. Phys. A 746 (2004) 655c-658c.

[Wei35] C. F. v. Weizsäcker, Zur Theorie der Kernmassen, Zeitschrift for Physik A Hadrons and Nuclei, 96:431-458 (1935).

[Wei36] C. F. v. Weizsäcker, Metastabile Zustände der Atomkerne . Natur- wissenschaften, 24:813-814, (1936).

[Win13] J. S. Winfield, A versatile high-resolution magnetic spectrometer for energy compression, reaction studies and nuclear spectroscopy, Nucl. Inst. Meth. B, 704 (2013) 76-83.

[Win54] M. M. Winn, Short-Lived Alpha Emitters produced by 3He and Heavy Ion Bombardments, Proceedings of the Physical Society, Sec. A, Vol. 67, No. 10, (1954).

[Wol88] H. Wollnik, Optics of Charged Particles, Academic Press (1988).

[Yav15] M. I. Yavor et al., Ion-optical design of a high-performance multiple-reflection time-of-flight mass spectrometer and isobar separator, Int. J. Mass Spectrom. 381-382 (2015) 1-9.